

FUNDAMENTAL STUDY OF MAGNETIC FIELD-ASSISTED MICRO-EDM FOR  
NON-MAGNETIC MATERIALS

BY

KENNETH G. HEINZ, JR.

THESIS

Submitted in partial fulfillment of the requirements  
for the degree of Master of Science in Mechanical Engineering  
in the Graduate College of the  
University of Illinois at Urbana-Champaign, 2010

Urbana, Illinois

Advisers:

Professor Shiv Kapoor  
Professor Richard DeVor

# Abstract

Micro-Electrical Discharge Machining ( $\mu$ -EDM) is a unique machining method capable of removing material in the sub-grain size range (0.1-10  $\mu\text{m}$ ) from materials irrespective of their hardness. This process is valuable in the manufacturing of miniaturized products where industry demand for increasingly hard materials has reached the limitations of conventional micro-machining techniques. However, the current material removal rates (MRR) for  $\mu$ -EDM range from 0.6-6.0  $\text{mm}^3/\text{h}$ , which is far below the desired minimum level of 10-15  $\text{mm}^3/\text{h}$  required for industrial viability. Many techniques have been previously developed to close this gap; however, they have all either fallen short of the industry goal or have been developed for specific materials, limiting widespread industrial use. This research seeks to develop a technique for improving MRR in  $\mu$ -EDM that can be applied to any material, with a focus on non-magnetic materials.

Two processes have been developed in an attempt to solve this problem, one aimed at altering the discharge plasma channel through the use of magnetic fields to affect plasma confinement and/or plasma stability and the other aimed to improve the material removal mechanism of the  $\mu$ -EDM process through the use of Lorentz forces induced in the melt pool. Single-discharge events were carried out on non-magnetic Grade 5 titanium workpieces to investigate the mechanics of material removal and evaluate the effectiveness of these two techniques. Discharge crater area analysis, high-speed imaging, melt pool volume analysis, erosion efficiency, plasma temperature, electron density, and debris field characterization were used as the response metrics to quantify and explain the change in the process mechanics with the application of these techniques.

By orienting the Lorentz force to act in a direction pointing into the workpiece surface, volume of material removed increases by nearly 50%. Furthermore, erosion efficiency is observed to increase by over 54%. Plasma temperature is unaffected and electron density shows a slight decrease with the addition of the Lorentz force. The distribution of debris around the crater is shifted to greater distances from the discharge center with the Lorentz force. Taken together, these facts strongly suggest that the Lorentz force process developed produces a mechanical effect in the melt pool to aid in increasing material removal. The application of the Lorentz force is not found to negatively impact tool wear.

# Acknowledgements

I would like to thank my advisors Professor Richard E. DeVor and Professor Shiv G. Kapoor for their passionate support of this research. Their guidance and mentoring during this research provided the necessary leadership for my development as a graduate student over the past two years. I would like to thank Professor Nick Glumac of the University of Illinois for the use of his facilities during this research. I would also like to thank Professor David Ruzic and Dr. Vijay Surla of the University of Illinois for their input in this research.

I would like to gratefully acknowledge the support of the Grayce Wicall Gauthier Chair in the Department of Mechanical Science and Engineering for funding this research. I would like to thank the Frederick Seitz Materials Research Laboratory Central Facilities, University of Illinois, which are partially supported by the U.S. Department of Energy under grants DE-FG02-07ER46453 and DE-FG02-07ER46471, for the use of their facilities.

I would like to thank my friends, roommates, and colleagues at the University of Illinois, in particular Johnson, Riley, Kurt, Kevin, Nick, Isha, and Keith, for their support, encouragement, and input during my time here as a graduate student. I would also like to thank Elaine Nicholas and Ruthie Lattina for both their friendship and administrative work during this research.

I am forever indebted to my parents Ken and Jill Heinz and my brother Michael Heinz for their constant love, support, and encouragement throughout my life. Finally, I would like to thank my Lord and Savior Jesus Christ for guiding me into this research and providing me the strength to finish the task set before me. *“Whatever you do, work at it with all your heart, as working for the Lord, not for men, since you know that you will receive an inheritance from the Lord as a reward. It is the Lord Christ you are serving.” Colossians 3:23-24.*

# Table of Contents

List of Figures.....	viii
List of Tables.....	xii
Chapter 1: Introduction.....	1
1.1 Background and Motivation .....	1
1.2 Research Objectives Scope and Tasks.....	5
1.2.1 Objective and Scope .....	5
1.2.2 Tasks .....	6
1.3 Outline of this Thesis .....	7
Chapter 2: Literature Review.....	9
2.1 Macro- vs. Micro-EDM .....	9
2.2 Mechanics of the $\mu$ -EDM Process .....	12
2.2.1 Material Removal Mechanism.....	13
2.2.2 Consequences of Debris in the Inter-Electrode Gap.....	17
2.2.3 Process Parameters.....	17
2.3 Process Improvements for Increased Productivity .....	21
2.3.1 Process Parameter Optimization .....	21
2.3.2 Dielectric Selection and Modification.....	27
2.3.3 Debris Removal .....	32
2.4 Magnetic Field-Plasma Interaction.....	36
2.4.1 General Use of Magnetic Fields in Plasma Applications .....	36
2.4.2 Optical Emission Spectroscopy .....	37

2.4.3 Use of Magnetic Fields for Plasma Confinement .....	39
2.4.4 Use of Magnetic Fields for Plasma Stability .....	41
2.4.5 Extending Magnetic Field Effects to $\mu$ -EDM.....	43
2.5 Gaps in Knowledge.....	44
<b>Chapter 3: Exploratory Testing of Magnetic Field-Assisted <math>\mu</math>-EDM for Non-Magnetic</b>	
<b>Materials .....</b>	<b>47</b>
3.1 Magnetic Field-Assisted Micro-EDM for Non-Magnetic Materials Concept	
Development.....	48
3.2 Testbed Design.....	51
3.2.1 Testbed Design Requirements .....	51
3.2.2 Testbed Topology .....	52
3.2.3 Actuation and Control.....	54
3.2.4 Single Spark Discharge Circuit Design .....	56
3.3 Experimental Results for Magnetic Field Effects on Plasma Characteristics in $\mu$ -EDM... 58	
3.3.1 Design of Experiments.....	59
3.3.2 Perpendicular Magnetic Field Results .....	60
3.4 Experimental Results for Magnetic Field-Assisted $\mu$ -EDM using Lorentz Forces .....	66
3.4.1 Design of Lorentz Force Experiments .....	66
3.4.2 Lorentz Force without Directional Workpiece Current Results .....	67
3.4.3 Lorentz Force Pointing into Workpiece Surface Results.....	71
3.4.4 Lorentz Force Pointing Outward From Workpiece Surface Results .....	75
3.4.5 Tool Wear Analysis .....	78
3.5 Chapter Summary .....	79

Chapter 4: Further Testing of Magnetic Field-Assisted $\mu$ -EDM for Non-Magnetic Materials....	81
4.1 Electromagnet Design.....	82
4.2 Experimental Results for Magnetic Field Effects on Plasma Characteristics in $\mu$ -EDM...	87
4.2.1 Experimental Design.....	87
4.2.2 Perpendicular Magnetic Field Results .....	88
4.3 Experimental Results for Magnetic Field-Assisted $\mu$ -EDM using Lorentz Forces .....	93
4.3.1 Lorentz Force Pointing into Workpiece Surface Results.....	93
4.3.2 Lorentz Force Pointing Outward From Workpiece Surface Results .....	99
4.4 Proposed Mechanism of Material Removal for the Lorentz Force Process .....	101
4.5 Chapter Summary .....	106
Chapter 5: Conclusions and Recommendations .....	108
5.1 Summary of Research Objective and Scope.....	108
5.2 Conclusions.....	108
5.3 Recommendations for Future Work.....	113
Bibliography.....	115

# List of Figures

Figure 2.1: Outline of $\mu$ -EDM process parameters and their effects on process characteristics ..	12
Figure 2.2: Principle of the EDM process [67].....	14
Figure 2.3: Breakdown mechanisms leading to spark discharge. Propagation of: (a) the primary electron avalanche; (b) a positive streamer; (c) a negative streamer [67-68].....	15
Figure 2.4: Schematic diagram showing the formation of both vaporized material and melted material on the workpiece and electrode surfaces during a spark discharge [66] .....	16
Figure 2.5: Schematic showing the theory of melt material removal by recoil forces developed after plasma channel collapse [53] .....	17
Figure 2.6: Diagram of typical voltage and current pulses during a discharge [67].....	18
Figure 2.7: Electrode wear (left) and material removal rate (right) versus current in the $\mu$ -EDM of high nickel alloy [6] .....	22
Figure 2.8: Effect of discharge energy and feedrate on material removal rate in aluminum according to Somashekhar et al. [94].....	23
Figure 2.9: Effect of discharge energy and feedrate on surface roughness in aluminum according to Somashekhar et al. [94].....	24
Figure 2.10: Effect of discharge energy and feedrate on process accuracy in aluminum according to Somashekhar et al. [94].....	25
Figure 2.11: MRR, TWR, and overcut results from the differences between deionized water and kerosene as the dielectric in $\mu$ -EDM [90] .....	28
Figure 2.12: Effect of powders on gap distance [15].....	30

Figure 2.13: Effect of powders on electrode wear [15] .....	31
Figure 2.14: Effect of SiC powder in water on MRR [18] .....	31
Figure 2.15: Effect of US vibrations on MRR in $\mu$ -EDM [26].....	32
Figure 2.16: Effects magnetic field-assisted debris removal on MRR in $\mu$ -EDM [36].....	35
Figure 2.17: Effect of electromagnetic current on plasma density throughout plasma radius. Higher current values correlate to higher magnetic field strengths [105] .....	40
Figure 2.18: Effect on an axial magnetic field on plasma electron temperature [107].....	41
Figure 2.19: Effect on an axial magnetic field on plasma electron density [107] .....	41
Figure 2.20: Examples of the different structures of discharge channels observed during single discharge pulses [111].....	42
Figure 2.21: Gross Lorentz force seen on a molten droplet forming at the end of an electrode [112] .....	44
Figure 3.1: Schematic of parallel magnetic field with directional current $\mu$ -EDM setup .....	48
Figure 3.2: Discharge current in the melt pool during a typical spark discharge and the resulting Lorentz force that develops in the presence of a parallel magnetic field....	49
Figure 3.3: a) 3D and b) 2D depictions of the directional discharge current in the melt pool and the resulting Lorentz forces that develop in the presence of a parallel magnetic field .....	50
Figure 3.4: Typical single-shot spark current pulse.....	50
Figure 3.5: Solid model of the $\mu$ -EDM testbed designed for experiments in this thesis .....	53
Figure 3.6: Assembled workpiece and electrode holder stages on the $\mu$ -EDM testbed .....	54
Figure 3.7: Workpiece stage step response to a 100 nm input step .....	55
Figure 3.8: Hybrid RC-transistor single-shot spark generator schematic.....	57

Figure 3.9: Definition of perpendicular magnetic field orientation .....	59
Figure 3.10: Comparison of SEM images between a normal $\mu$ -EDM discharge an a $\mu$ -EDM discharge in the presence of a perpendicular magnetic field .....	61
Figure 3.11: Example of the 100 $\mu$ m tool electrode in focus through a 20x objective lens prior to a discharge.....	62
Figure 3.12: Example progression of high-speed images collected during a spark discharge .....	63
Figure 3.13: Example of discharge plasma high-speed images after processing .....	63
Figure 3.14: Example of high-speed imaging of a $\mu$ -EDM discharge in air .....	64
Figure 3.15: High-speed images from a normal $\mu$ -EDM discharge .....	65
Figure 3.16: High-speed images from a $\mu$ -EDM discharge in the presence of a perpendicular magnetic field.....	65
Figure 3.17: Definition of parallel magnetic field orientation.....	66
Figure 3.18: Digitizing the discharge crater surface (SEM spot sizes to scale) .....	68
Figure 3.19: 3D surface topography from laser scan.....	68
Figure 3.20: Side view of 3D surface map .....	69
Figure 3.21: SEM and laser scan image comparison between parallel field and no field experiments .....	71
Figure 3.22: Example of discharge gap voltage waveform during a $\mu$ -EDM discharge .....	73
Figure 3.23: SEM and laser scan image comparison between three power levels for Lorentz force into workpiece surface and no field experiments .....	75
Figure 3.24: SEM and laser scan image comparison between three power levels for Lorentz force pointing out from workpiece surface and no field experiments .....	77
Figure 4.1: Solid model of the electromagnet design .....	83

Figure 4.2: Solid model of the redesigned $\mu$ -EDM testbed on left and electromagnet mated to testbed on right.....	84
Figure 4.3: FEM simulation results of permanent magnet design at maximum coil current.....	86
Figure 4.4: Electromagnet on $\mu$ -EDM testbed.....	86
Figure 4.5: Spectrometer setup on $\mu$ -EDM testbed .....	89
Figure 4.6: Example of spectrum collected .....	89
Figure 4.7: Example of a PeakFit plot used for deconvoluting spectral data .....	90
Figure 4.8: Samples of the 3D laser scanning images taken of the discharge craters .....	95
Figure 4.9: Electron path of travel when E-field and B-field are perpendicular .....	97
Figure 4.10: Example of the measurements taken from the debris field .....	98
Figure 4.11: Debris field distribution for the Lorentz force pointing into the workpiece surface configuration .....	99
Figure 4.12: Samples of the 3D laser scanning images taken of the discharge craters .....	100
Figure 4.13: Movement of the melt pool material during a $\mu$ -EDM discharge .....	103
Figure 4.14: Melting/Splashing material removal mechanism.....	105

# List of Tables

Table 2.1: Optimal parameter found by Pradhan et al. for the $\mu$ -EDM of titanium given a specific physical requirement [8].....	26
Table 3.1: Experimental conditions for permanent magnet tests.....	60
Table 3.2: Perpendicular magnetic field discharge crater area comparison .....	62
Table 3.3: Comparison of No Field and Parallel Field volume data .....	70
Table 3.4: Titanium Workpiece Properties.....	72
Table 3.5: Comparison of No Field and Lorentz Force into the workpiece experiments.....	74
Table 3.6: Comparison of No Field and Lorentz Force out from the workpiece experiments .....	76
Table 3.7: EDS data for workpiece and melt pools .....	79
Table 4.1: Summary of electromagnet coil wire specifications.....	85
Table 4.2: Experimental conditions for electromagnet trials.....	87
Table 4.3: Equation 2.1* and 2.2* Values .....	91
Table 4.4: Plasma Characteristics for Perpendicular Field Experiments.....	92
Table 4.5: Summary of Lorentz Force into workpiece experiments .....	94
Table 4.6: Plasma Characteristics for Parallel Field Experiments.....	96
Table 4.7: Summary of Lorentz force pointing out from the workpiece experiments .....	100

# Chapter 1

## Introduction

### 1.1 Background and Motivation

Micro-Electrical Discharge Machining ( $\mu$ -EDM) is a unique machining method capable of removing material in the sub-grain size range (0.1-10  $\mu\text{m}$ ) from materials irrespective of their hardness [1]. This process is valuable in the manufacturing of miniaturized products where industry demand for increasingly hard materials has reached the limitations of conventional micro-machining techniques. Some examples include tool steel, tungsten carbide, and titanium used in the manufacture of tooling for micro-scale machining, micro-mold and die making, diesel fuel injector fabrication, and medical device manufacturing. However, the current material removal rates (MRR) for  $\mu$ -EDM range from 0.6-6.0  $\text{mm}^3/\text{h}$  [1], which is far below the desired minimum level of 10-15  $\text{mm}^3/\text{h}$  required for industrial viability.

Efforts have been made to improve the MRR of the  $\mu$ -EDM process through research into several key areas. The optimization of machining parameters has been shown to improve material removal rates in the machining of specific materials. The selection and modification of dielectric fluids has been shown to both directly and indirectly affect MRR through alteration of discharge crater characteristics. Finally, improvements in debris removal strategies have yielded promising increases in MRR due to the adverse effects debris can have on the stability of the discharge process when it is allowed to build up in the inter-electrode gap.

Given the large number of machining parameters influencing the efficiency of the  $\mu$ -EDM process such as gap distance, discharge current, pulse on-time, and duty cycle, the optimization of these parameters often yields improvements in the MRR of the process. Despite nearly 60 years of research into the EDM process, accurate knowledge of the actual discharge process remains the subject of much debate [2]. As a result, robust models that can accurately predict optimal machining parameters for any material do not exist and full-scale parametric studies are often required for individual materials in order to determine the optimal machining parameters [3-10]. The lack of knowledge into the discharge process limits the use of these studies as once process conditions are changed, such as the dielectric fluid properties, or material properties are changed, such as workpiece chemical properties, the optimal machining parameters change and new full-scale parametric studies are again needed to optimize MRR.

The selection and modification of dielectric fluids has also been investigated for effects on MRR in the  $\mu$ -EDM process. Studies have been done on comparisons between tap water, distilled water, deionized water, and kerosene, all of which point to higher MRR, lower electrode wear, and improved surface finishes with water as the dielectric versus kerosene [11-13]. As a result, water has become the standard dielectric in most  $\mu$ -EDM processes. The modification of dielectric fluids through the addition of suspended powders has been used to improve surface quality, MRR and tool wear rates [14-18]. The primary goal of most powder-mixed dielectric studies is to improve surface finishes in  $\mu$ -EDM, which can decrease overall part production time by reducing or eliminating the need for post-machining polishing. However, improvements in actual MRR during the  $\mu$ -EDM process are often small with the addition of powders to the dielectric fluid and come as an indirect result of the efforts to improve surface

characteristics [15]. Because of this, machining times are not significantly reduced through the use of powder-mixed dielectrics.

Debris removal is the most promising area investigated for improvements in MRR. Due to the small inter-electrode gaps used in  $\mu$ -EDM, the debris ejected from each spark discharge can present a problem for the stability of the process. Debris that clogs machining gaps inevitably causes abnormal electrical discharges, resulting in decreased MRR, and resolidified material on the workpiece surface decreases process efficiency. In order to fully understand the relationship between the  $\mu$ -EDM process and the debris it produces, studies have been done to model debris movement in the discharge gap [19], determine its effect on the discharge process [20], and on monitoring the state of the debris in the discharge gap [21]. These studies reveal that the buildup of debris in the discharge gap is a significant problem in  $\mu$ -EDM and efforts to reduce the debris buildup have the potential to significantly increase the MRR of  $\mu$ -EDM.

Several techniques have been investigated to improve debris removal, including orbital electrode movement [22], micro-scale debris flushing [11], and significant research efforts have been made into the use of ultrasonic vibration for debris flushing [24-34]. One common problem with these techniques, particularly the use of ultrasonic vibrations, is that they tend to increase tool wear and decrease machining accuracy [33]. The use of magnetic fields to assist in debris removal has been explored and was found to improve MRR without the side effect of decreased machining accuracy [35]; however, the technique developed required that the workpiece material be magnetic in order for the magnetic fields to be effective. While the results of this study are promising, many of the workpiece materials used in  $\mu$ -EDM are non-magnetic, thus the usefulness of the magnetic field assisted  $\mu$ -EDM technique is very limited.

Despite all the research that has gone into improving the material removal rate of the  $\mu$ -EDM process, no robust solution has been identified with the effectiveness to bring about the large increases in MRR needed for industrial viability without side-effects that adversely affect the desirable qualities of  $\mu$ -EDM. The use of magnetic fields in the  $\mu$ -EDM process has shown significant promise in providing this solution; however, the mechanism currently used in the magnetic field assisted  $\mu$ -EDM process relies on the magnetic properties of the workpiece material, making it inadequate for universal use in  $\mu$ -EDM.

The use of alternative mechanisms in magnetic field assisted  $\mu$ -EDM such as plasma confinement or Lorentz forces could increase MRR independent of workpiece magnetism, thus creating a process that could be universally applied in  $\mu$ -EDM. The material removal mechanism in  $\mu$ -EDM is linked to the heating of the workpiece material through the discharge plasma channel. However, the plasma channel expands rapidly after discharge initiation, causing the current density and plasma temperature to decrease rapidly, thereby reducing the heating of the workpiece [2]. Successful confinement of the  $\mu$ -EDM plasma through the use of magnetic fields could prevent the decrease in workpiece heating, thereby making each spark discharge more efficient and increasing the overall MRR of the process. Significant research has been done on successful magnetic confinement of DC gas discharge plasmas [36-39], but it has not yet been tested in the confinement of  $\mu$ -EDM plasmas. The possibility also exists to use the high currents associated with the discharge pulse in conjunction with magnetic fields to produce a Lorentz force [40] in the workpiece melt pool. The additional force in the melt pool could aid in ejection of material from the discharge crater, thereby improving MRR.

## 1.2 Research Objectives Scope and Tasks

### 1.2.1 Objective and Scope

The objective of this thesis is to develop a magnetic-field-assisted  $\mu$ -EDM process to improve MRR regardless of workpiece magnetic properties. Magnetic fields will be used to determine their effectiveness in confining the  $\mu$ -EDM plasma channel with the goal of increasing plasma temperature and electron density to improve workpiece heating and thus improve MRR. Magnetic fields will also be used in conjunction with the high current pulses present in  $\mu$ -EDM to produce a Lorentz force in the melt pool with the goal of improving material ejection to increase MRR.

The scope of this research is to focus on the magnetic field interactions with the  $\mu$ -EDM discharge process to meet the objective of this research. This will be done in the context of single-spark discharges in order to isolate the fundamental mechanics in the discharge process. Both the plasma produced during a discharge as well as the resulting discharge crater on the workpiece surface will be analyzed through various methods to gain insight into the process. Only Grade 5 titanium alloy will be used for workpiece material since it is a common non-magnetic workpiece material used in  $\mu$ -EDM. Only tungsten wire will be used for electrode material since it is one of the most common electrode materials in  $\mu$ -EDM. Only deionized water will be used as a dielectric as it has been shown to be a superior dielectric in  $\mu$ -EDM. Magnetic fields will be produced by permanent magnets for ease of use during proof of concept experimentation, and will be produced by electromagnets for adjustability and field uniformity during full-scale testing.

## 1.2.2 Tasks

To accomplish the objective of this research, the following tasks must be carried out:

1. The plasma confinement and Lorentz force techniques for improving MRR in  $\mu$ -EDM through the use of magnetic fields without dependence on workpiece material properties will be developed.
2. A  $\mu$ -EDM testbed, single spark discharge circuit, and electromagnet will be designed to facilitate investigation of magnetic-field-assisted single-spark  $\mu$ -EDM discharges. The design of these components will directly reflect experimental needs dictated by the proposed magnetic field techniques of this thesis.
3. A set of response metrics will be defined in order to quantify the effectiveness of the plasma confinement and Lorentz forces as well as shed light onto the mechanics of the process. These metrics will focus on observation and characterization of the discharge plasma, as well as observation and characterization of the discharge crater produced on the workpiece surface.
4. Methods will be outlined and procedures will be developed to enable the measurements necessary to quantify the response metrics. This includes specifying the required equipment as well as detailing the post-processing methods used to convert the raw data into accurate usable information.
5. Experiments will be run to collect data on both the standard  $\mu$ -EDM discharge process as well as the proposed magnetic-field-assisted  $\mu$ -EDM discharge processes. Initially a set of proof of concept experiments will be run using permanent magnets as the source of the magnetic field.

6. Following positive proof of concept results, more in-depth testing will be conducted using an electromagnet as the source of the magnetic field to allow multiple field strengths to be tested for a more complete view of the effects of the process.
7. The experimental data collected will be analyzed and changes in plasma characteristics and discharge crater characteristics will be quantified. The magnetic-field-assisted  $\mu$ -EDM techniques will be compared against the standard  $\mu$ -EDM discharges to determine the effectiveness of the plasma confinement and Lorentz forces. Also from the data collected, a mechanism will be proposed by which the magnetic-field-assisted  $\mu$ -EDM techniques developed work to alter the  $\mu$ -EDM process.

## 1.3 Outline of this Thesis

The remainder of this thesis is organized as follows. Chapter 2 provides a thorough literature review of topics relevant to the subject matter of this thesis. The first section discusses an overview of the macro-scale EDM process and its evolution into the current micro-scale EDM process. The second section discusses the mechanics of the  $\mu$ -EDM process, including process parameters, tooling, and surface effects. The third section provides a look at the current process improvements designed to improve the material removal rates in  $\mu$ -EDM. The final section looks at current research into magnetic field-plasma interactions.

Chapter 3 discusses the results from exploratory investigations on magnetic-field assisted  $\mu$ -EDM for non-magnetic materials utilizing permanent magnets as the source of the magnetic field. The first section covers the theory behind the magnetic field concepts that will be investigated in this thesis, as the application of these techniques will drive the design of the testbed. The second section looks at the design of the testbed itself and the components

necessary for its function. The third section presents the results from experiments exploring the effect of magnetic fields on discharge plasma characteristics in  $\mu$ -EDM. Finally, the fourth section discusses the results from experiments utilizing a Lorentz force pointing into and out from the workpiece surface to alter the material removal mechanism.

Chapter 4 presents the results from further investigations into magnetic-field assisted  $\mu$ -EDM for non-magnetic materials using magnetic fields generated by an electromagnet. The first section covers the design of the electromagnet and changes made to the testbed to accommodate the magnet. The second section presents and discusses the results from the experiments conducted using the electromagnet as the source for the magnetic field to investigate the field effects on  $\mu$ -EDM plasma characteristics. The third section covers results from the electromagnet experiments utilizing Lorentz forces to alter the material removal mechanism. The final section makes a case for a proposed mechanism of material removal in the processes developed using data collected in this thesis.

Chapter 5 provides a summary of the work completed during this research in terms of a specific set of research conclusions. Finally, potential areas for future work are presented.

# Chapter 2

## Literature Review

The objective of this thesis is improvement of the MRR in  $\mu$ -EDM through the use of magnetic fields, thus it is important to understand both the mechanics of the material removal mechanism in  $\mu$ -EDM as well as the current state of productivity improvement methods for  $\mu$ -EDM in order to successfully develop a productivity improvement technique. With this in mind, the literature review reported in this chapter has been organized in the following way. The first section is an overview of the fundamental differences between macro- and  $\mu$ -EDM. Next, the mechanics involved in the EDM process are discussed. The third section reviews current methods of productivity improvement, and the final section covers research on plasma-magnetic field interactions.

### 2.1 Macro- vs. Micro-EDM

Micro-EDM technology has evolved through the years from macro-EDM technology as tool manufacturers improved the form accuracy and structure precision of EDM machines into the submicron domain [46]. Current commercial  $\mu$ -EDM machines are capable of machining components with large aspect ratios (10:1 to 50:1), small features (20-50  $\mu\text{m}$ ) and high accuracies ( $\pm 1-3 \mu\text{m}$ ) [1]. State-of-the-art novel machine tool topologies are also being developed for  $\mu$ -EDM that have reported precisions down to 100nm for die-sinking micro-EDM [47] and 600nm for micro-wire-EDM [48].

The mechanics of the EDM process are fundamentally the same between the macro-scale and micro-scale processes, with differences in three key areas: discharge energy, inter-electrode gap distance, and plasma channel diameter, all of which are interrelated. In order to machine components on the micro-scale using the EDM process, the unit material removal per spark discharge needs to be reduced to refine control over the final workpiece dimensions [114]. This is accomplished through a reduction in the discharge energy by decreasing discharge voltage, current, and pulse on-times [71]. The reduced gap voltage also results in smaller inter-electrode gaps in  $\mu$ -EDM, as the smaller voltages are unable to initiate dielectric breakdown over the larger gap distances used in macro-scale EDM. The reduced discharge current and pulse duration curtails the plasma channel expansion, resulting in a characteristically smaller plasma channel diameter in  $\mu$ -EDM versus macro-scale EDM [71].

$\mu$ -EDM machining centers are mechanically unique from macro-scale EDM machines in that the spark discharge circuit, gap monitoring strategy, and motion platforms must all meet more stringent performance criteria for  $\mu$ -EDM applications. The discharge circuits used in  $\mu$ -EDM must be capable of producing extremely small energy pulses, often in the micro-joule range, by providing low voltage and low current pulses over pulse durations of several hundred nanoseconds to several microseconds with duty cycles of 60-90% [7, 9].

Resistor-capacitor (RC) circuits have been shown to be superior in  $\mu$ -EDM to the traditional transistor-based discharge circuits used in macro-scale EDM given the ability of the RC circuit to produce extremely low energy discharges with nanosecond-range pulse on-times. The use of RC discharge circuits in  $\mu$ -EDM has resulted in better dimensional accuracy, better surface finish, and smaller debris diameters which enhance debris flushing [113]. However, RC circuits suffer

from low duty cycles as the inherent delay between each pulse discharge as the capacitor recharges results in low discharge frequency.

Traditional transistor-based circuits have the ability to achieve very high duty cycles but have an inherent delay in response to control inputs due to gate rise and fall times in the transistor, which makes it difficult to produce the short discharge on-times desired in  $\mu$ -EDM [115]. However, the ability to control pulse timing for high duty cycles with transistor circuits is a distinct advantage over RC circuits when looking to improve MRR, thus research into unique and innovative transistor-based discharge circuits for use in  $\mu$ -EDM is continually pursued as transistor and sensing technology improves [114].

The gap monitoring strategies used in  $\mu$ -EDM must be capable of detecting the differences between sparks, arcs, short circuits, and open circuits with nanosecond range sampling periods [70]. Acoustic techniques [21] as well as high-speed data acquisition [70] have been investigated to handle monitoring of the pulse conditions with extremely high sampling frequencies. Fuzzy logic controllers have been implemented in conjunction with high-speed data acquisition gap monitoring and have been shown to suppress unwanted arc pulses to smooth and stabilize the process with better results in  $\mu$ -EDM than conventional PWM controllers [129].

Finally, the motion platforms used in  $\mu$ -EDM machine tools need to be capable of sub-micron positioning to maintain control over the inter-electrode gap as well as the feedrate of the cutting process [115]. Inter-electrode gaps are typically on the order of several microns in  $\mu$ -EDM, versus several hundred microns to several millimeters in macro-scale EDM, although the gap is rarely directly measured and is instead inferred from gap voltage [71]. To maintain these gaps, electro-mechanical and hydraulic systems are typically used for motion control in ultra-precision 3-5 axis machine tools to achieve positioning accuracies of less than 1  $\mu\text{m}$  [71].

## 2.2 Mechanics of the $\mu$ -EDM Process

The ultimate goals of nearly every machining process are to maximize material removal rate, minimize tool wear rate, and maximize process accuracy. In  $\mu$ -EDM, the controllable process parameters often have complex relationships with the process mechanics, making this a difficult optimization problem. Figure 2.1 shows a breakdown of the process parameters and their connections to the process mechanics. It is important to first understand the mechanics of the  $\mu$ -EDM process before attempting to alter the process parameters due to these complex relations.

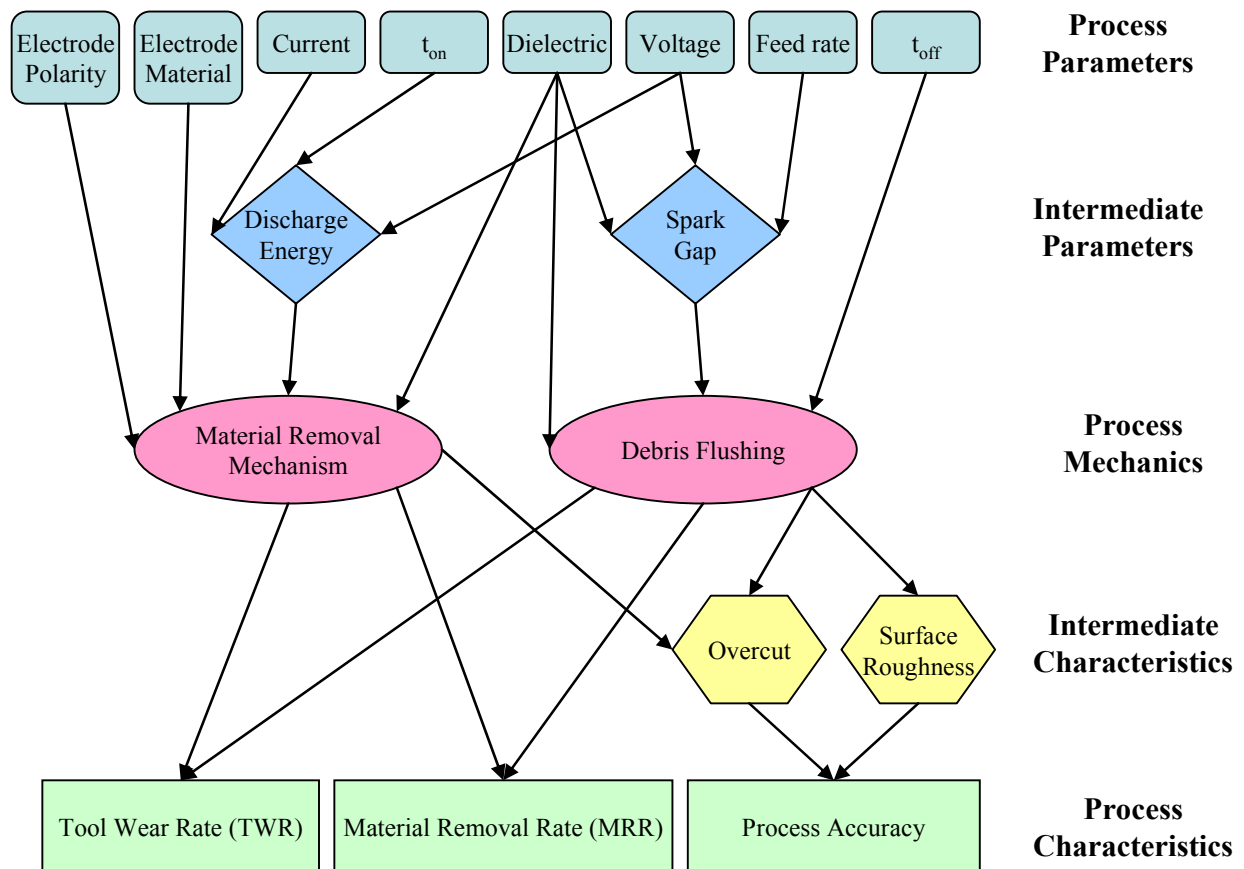


**Figure 2.1: Outline of  $\mu$ -EDM process parameters and their effects on process characteristics**

The mechanics of the  $\mu$ -EDM process can be broken down into three sections; the material removal mechanism, flushing of the debris following material removal, and the process parameters that affect the performance of these two processes. The material removal mechanism defines how material is actually removed from the workpiece in  $\mu$ -EDM, the flushing of debris dictates what happens to the material once it is removed from the workpiece, and the process parameters specify what control there is over these processes.

### 2.2.1 Material Removal Mechanism

A complete understanding of the material removal mechanism for either macro-scale EDM or  $\mu$ -EDM does not currently exist [2]. Significant portions of the material removal mechanism have been successfully modeled and validated from experimental data at the macro-scale [50-60], however far less research has been done into the material removal mechanism of  $\mu$ -EDM [61-65]. Many aspects of the  $\mu$ -EDM process are similar to those of the macro-scale EDM process [63], and principles of the material removal mechanism found at the macro-scale can be applied to an understanding of the micro-scale process if appropriate discretion is used. The material removal mechanism described in this thesis will be covered accordingly.

The EDM process involves the creation of a plasma channel in the form of a spark discharge between the workpiece and electrode, which heats the surfaces of the workpiece and electrode [63]. Some of the material is heated beyond its boiling point and is removed by vaporization, while other material is only heated beyond its melting temperature and forms a molten pool on the material surface [41]. Once the plasma channel collapses at the end of the discharge pulse, some of the molten material is ejected into the dielectric fluid, where it resolidifies into debris [66]. The process of creating a spark discharge occurs extremely rapidly, with pulse on-times on the order of several hundred nanoseconds to several microseconds and duty cycles in the range

of 60-90% [7, 9], resulting in appreciable material removal over time. A schematic of the basics of this process can be seen in Fig. 2.2 along with plots of the voltage and current conditions in the discharge gap that correspond to each stage of the discharge.

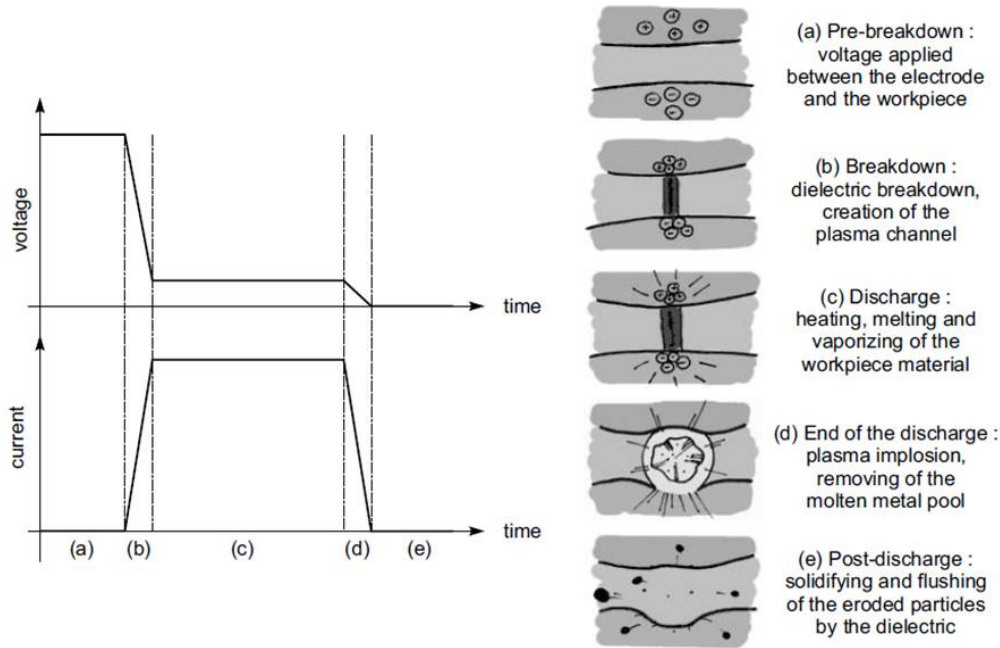


**Figure 2.2: Principle of the EDM process [66]**

To begin the process of creating a spark discharge, a voltage potential is applied across a non-zero gap between the workpiece and electrode, where a dielectric medium acts as an insulator to prevent current flow. The dielectric medium begins to ionize in the inter-electrode gap in the presence of the high electric fields that develop and the process of dielectric breakdown begins. There are two basic theories of dielectric breakdown, one that suggests breakdown begins with the growth of a vapor bubble between the electrodes and another that suggests the formation of streamers between the electrodes [62]. In  $\mu$ -EDM, the discharge pulse occurs over such a short time period that the theory of vapor bubble growth is likely incorrect, so the theory of streamer propagation will be discussed [62].

Streamers begin with an electron avalanche (Fig. 2.3a), and once the avalanche reaches sufficient amplification, the thin weakly-ionized channel of a streamer is created between the electrodes [66]. Positive streamers, shown in Fig. 2.3b, form when gap distances are small and voltages are moderate (as in  $\mu$ -EDM) because the electron avalanche has not grown enough before reaching the anode to form a ionized region, thus the streamer begins at the anode and grows towards the cathode once the avalanche reaches the anode [66-67]. Negative streamers, shown in Fig. 2.3c, form when inter-electrode gaps are large and/or gap voltages are high, where the initial electron avalanche grows to sufficient size before reaching the anode. The avalanche-to-streamer transition occurs in the gap in this case and the streamer propagates towards both electrodes simultaneously [66-67].

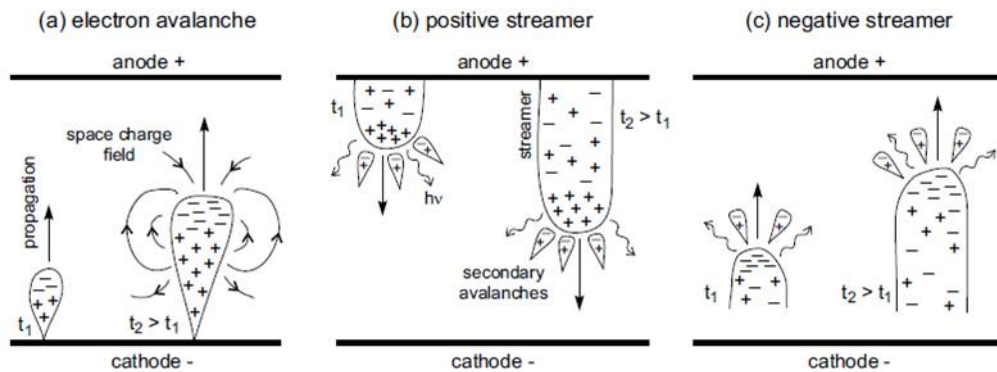


**Figure 2.3: Breakdown mechanisms leading to spark discharge. Propagation of: (a) the primary electron avalanche; (b) a positive streamer; (c) a negative streamer [66-67]**

After a finite amount of time [50], referred to as the ionization time, the dielectric medium breaks down and the weakly ionized streamer channel becomes a highly ionized plasma channel between the electrode and workpiece. Current flows through the plasma channel during the discharge, heating the workpiece and electrode surfaces, causing melting and vaporization of the material in immediate proximity to the plasma channel [65], as shown in Fig. 2.4. The actual mechanism that transfers the electrical energy to thermal energy is still unknown [68]. The amount of workpiece material removed by vaporization is very small in comparison to the

amount removed due to melting, as reported by Wong et al. [61]. The workpiece material that is melted in the discharge crater is not removed until the end of the discharge, which is signified by the implosion of the plasma channel.

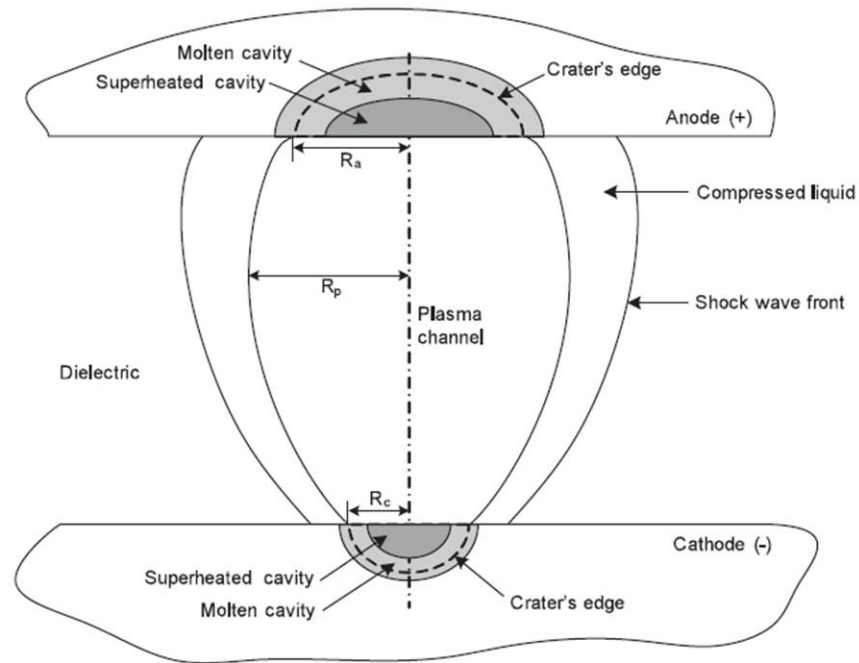


**Figure 2.4: Schematic diagram showing the formation of both vaporized material and melted material on the workpiece and electrode surfaces during a spark discharge [65]**

The process involving the removal of the melted workpiece material from the workpiece surface after plasma channel collapse is very complex and stochastic, involving forces originating from electrodynamics, electromagnetics, thermodynamics and hydrodynamics [69]. As a result, comprehensive theories on the removal of melt material are nearly impossible to develop [65], so simplifications are made. A number of studies have developed and tested models that assume the plasma channel exerts a pressure on the melt pool during the discharge [52, 55, 62, 64]. Once this pressure is released by the implosion of the plasma channel at the end of the discharge, a recoil effect takes place and the molten material is ejected from the workpiece surface [52], as seen in Fig. 2.5. The debris resolidifies into globules as it is entrained in the dielectric fluid as it re-enters the electrode gap.

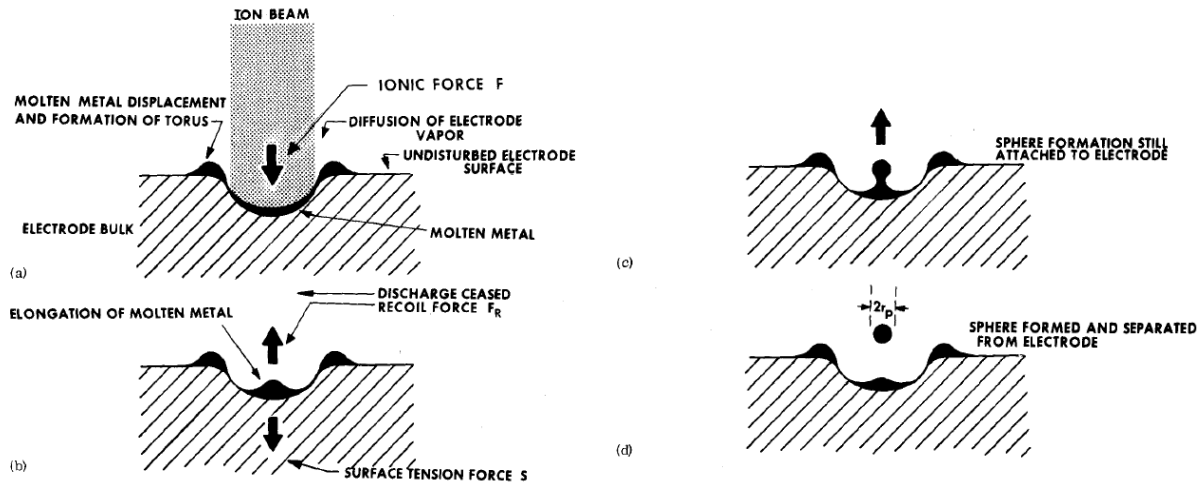


**Figure 2.5: Schematic showing the theory of melt material removal by recoil forces developed after plasma channel collapse [52]**

## 2.2.2 Consequences of Debris in the Inter-Electrode Gap

Once the debris has entered the dielectric fluid in the inter-electrode gap, it needs to be removed from the working area. The accumulation of debris in the discharge gap is a significant problem in  $\mu$ -EDM as the inter-electrode gap distances are very small. If debris is allowed to accumulate in the gap, the conductivity in the gap increases and short-circuit discharges occur instead of normal spark discharges, reducing the efficiency of the process [20]. Debris in the gap can also alter the energy distribution in the plasma channel, further reducing the efficiency of each spark discharge [20]. Recently Wang et al. [19] developed a method of simulating the debris movement in  $\mu$ -EDM deep hole drilling and found that typically the debris tends to accumulate near the workpiece and electrode surfaces and in corners. Successful elimination of this debris buildup has been shown to be essential for improving machining stability [32].

## 2.2.3 Process Parameters

**Discharge pulse parameters.** The discharge pulse parameters that are commonly controlled are shown in Fig. 2.6. The no-load voltage  $V$ , also called the open-gap voltage, the pulse current

$I$ , and the pulse on-time and pulse off-time are labeled in Fig. 2.6. The no-load voltage  $V$  is the voltage applied to the electrode gap prior to a discharge and is the source of the electric field used to initiate dielectric breakdown [63]. The pulse current  $I$  is the current flowing through the plasma channel during a discharge event. The pulse on-time is the time period between dielectric breakdown and plasma implosion during which the plasma channel is allowing current to flow between the workpiece and electrode [70]. The pulse off-time is the time period following the end of a spark discharge where no voltage is applied to the electrode gap prior to the beginning of another discharge cycle [70].

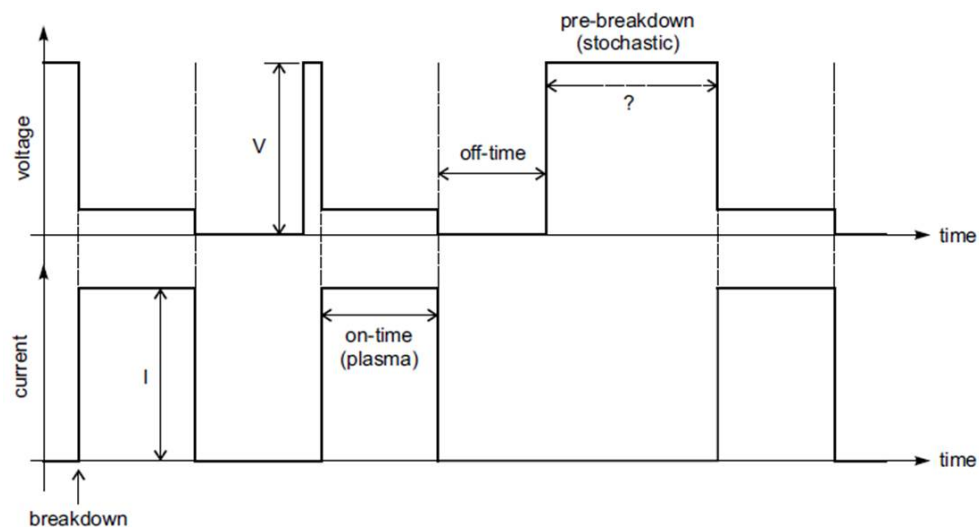


**Figure 2.6: Diagram of typical voltage and current pulses during a discharge [66]**

As was briefly mentioned in Section 2.1 and seen in the process outline in Fig. 2.1, three of the discharge parameters, the voltage, current, and on-time, are linked to the discharge energy, which is defined as the product of these parameters [71]. The discharge energy has a direct effect on the resulting discharge crater dimensions [65], which affect material removal rate, electrode wear, and process accuracy [61]. Smaller discharge energies produce smaller discharge craters, which reduce material removal rates and electrode wear, but improve process accuracy as each discharge pulse has a finer resolution with the decreased discharge crater size

[61]. The opposite is true for larger discharge energies. The no-load voltage  $V$  also affects the inter-electrode gap distance, as larger gaps require larger voltages to initiate dielectric breakdown. Larger gap distances can improve dielectric circulation and prevent debris buildup; however, the larger voltages required for increased gap distances result in poor dimensional accuracy, as reported by Jahan et al. [72].

The pulse off-time allows for both the flushing of debris from the discharge gap as well as recovery of the dielectric strength of the dielectric fluid [71]. Adjusting pulse off-time is often done to find an optimal balance between machining time and debris flushing. If the pulse off-time is set very long, much of the debris will be flushed from the machining gap, reducing the risk of subsequent abnormal discharges, but the material removal rate will be drastically reduced due to the inefficient use of time during machining. However, if the pulse off-time is set very short, much of the debris will still be present in the discharge gap during the next discharge, and the dielectric fluid may not have sufficient recovery time, causing a high frequency of abnormal discharges [71]. This reduces the material removal rate, as abnormal discharges are not an efficient way to remove material, and also affects the surface quality of the machining process as arc discharges can damage the workpiece surface [73]. Thus, pulse off-times are adjusted for a balance between debris flushing and machining time.

**Electrode material.** The electrode materials typically used are various forms of copper and tungsten. Jahan et al. [83] recently investigated the effects of tungsten (W), copper tungsten (CuW), and silver tungsten (AgW) on the  $\mu$ -EDM process. They concluded that AgW produced the best surface finish, while CuW achieved the highest MRR, followed by AgW. Electrode wear rate was lowest with W, followed by CuW and AgW. Tungsten carbide (WC) is another popular tungsten composition used for  $\mu$ -EDM processes [5, 84-86].

A study was conducted by Tsai et al. [68] to investigate the effect of electrode material boiling point on electrode wear rate. They found that electrode materials with high boiling points experienced lower volumetric tool wear than those with lower boiling points, regardless of workpiece material. This helps explain why tungsten is achieving significant success as an electrode material in  $\mu$ -EDM.

**Electrode polarity.** The electrode polarity can be set as either positive or negative. Positive polarity indicates that the workpiece is set as the anode, i.e. electron movement in the plasma channel is towards the workpiece, and negative polarity sets the electrode as the anode. When negative polarity is used, MRR is increased and electrode wear is decreased [72]. This is because with negative polarity, the workpiece is set as the cathode which experiences a greater concentration of discharge energy (Fig. 2.4) and thus undergoes greater heating than the anode, where the discharge energy is dissipated [75]. Also, with the electrode as anode, a protective carbon or oxide layer forms on the electrode to prevent tool erosion when using either hydrocarbon-based dielectrics or water-based dielectrics, respectively [76].

**Feedrate and dielectric fluid.** The electrode feedrate can be adjusted to directly impact the inter-electrode gap distance. A slow feedrate results in the gap distance having an average value larger than the optimal distance, slowing the discharge process as fewer spark discharges occur but enhancing debris flushing by allowing dielectric fluid to be more easily flushed from the spark gap. A fast feedrate can result in the gap distance becoming too short, resulting in a high occurrence of short-circuit discharges and hindering debris removal.

The dielectric fluid plays a similar role in the spark gap. Dielectric fluids with weak dielectric strengths can open the gap distance to increase debris flushing, as the same gap voltage is able to initiate dielectric breakdown over greater distances, and vice-versa for fluids with

strong dielectric strengths [11]. The chemical composition of the dielectric fluid can also affect the process and will be discussed in Section 2.3.2. Finally, the dielectric fluid thermal conductivity and viscosity can play minor roles in debris flushing [12].

## 2.3 Process Improvements for Increased Productivity

The three process characteristics of most concern in  $\mu$ -EDM are the tool wear rate, material removal rate, and process accuracy. These characteristics are affected by the material removal mechanism and the state of debris flushing, as shown in Fig. 2.1. Improvements made to the  $\mu$ -EDM process often result in tradeoffs between the TWR, MRR, and process accuracy [91]. The following discussion is aimed at identifying these tradeoffs in the context of the three avenues used to alter the process characteristics. First, the optimization of process parameters that mainly affect the material removal mechanism are investigated. Second, changes in the dielectric fluid, which bridge the gap between effects on material removal mechanism and effects on the debris flushing, are discussed. Finally, auxiliary processes that have been developed to improve debris removal are reviewed.

### 2.3.1 Process Parameter Optimization

Comprehensive parametric studies that map the interactions and effects of the process variables to changes in machining characteristics do not exist. According to Pham et al. [91], it is this lack of information that prevents the development of knowledge-based  $\mu$ -EDM planning systems. However, partial studies have been conducted looking at a limited number of variables and selected machining characteristics. Due to the thermal nature of  $\mu$ -EDM, the workpiece

thermal properties play a large role in how the material responds to differing process conditions [92], therefore parametric studies are only valid for the workpiece materials used in the study.

**Single parameter investigations.** A few studies exist that focus on determining the effect of a single process parameter on the machining characteristics while holding all other process parameters constant [3-5]. Liu et al. [5] examined the effects of discharge current on TWR and MRR in the  $\mu$ -EDM of a high nickel alloy. Figure 2.7 shows that tool wear was found to exponentially increase with increasing discharge current, whereas an optimum discharge current was found to maximize material removal rate. They concluded that at low discharge energies, vaporization dominated the material removal mechanism, leading to low material removal rates. However, at extremely high discharge energies, the spark discharge is explosive, leading to the dielectric fluid being over-flushed from the spark gap, leaving insufficient time in between discharges for dielectric recovery. Thus, abnormal discharges would result, reducing MRR at high discharge energies as well, causing a maximum MRR to be realized at a discharge current pulse of 500mA.

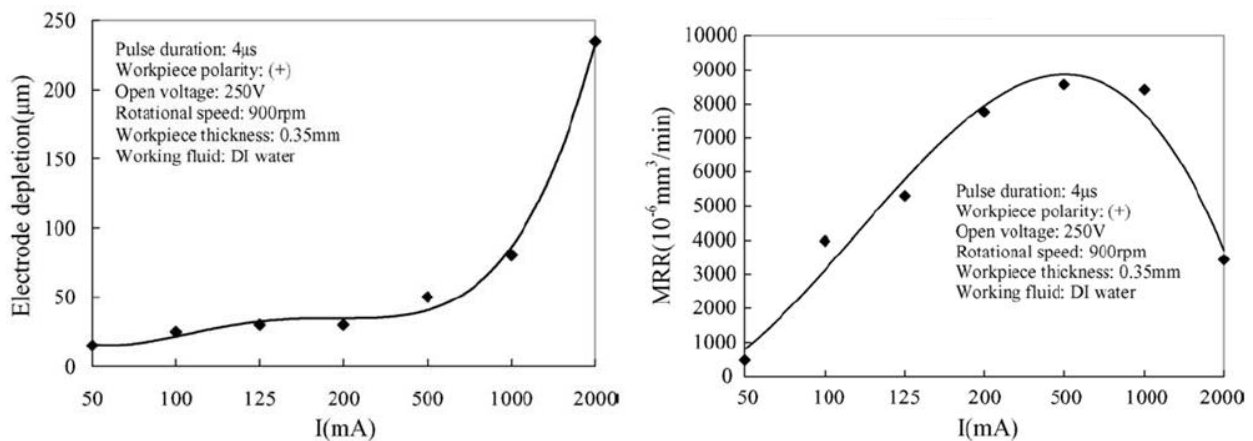


**Figure 2.7: Electrode wear (left) and material removal rate (right) versus current in the  $\mu$ -EDM of high nickel alloy [5]**

**Multiple parameter investigations.** There are several parametric studies that examine the effects of multiple process parameters and their interactions on machining characteristics [7-10, 61, 93]. Somashekhar et al. [8, 93] conducted a set of studies on the  $\mu$ -EDM of aluminum, focusing on the effects of varying voltage, discharge energy (via discharge capacitance), and feedrate on MRR and process accuracy (measured as amount of overcut present and surface roughness). Figure 2.8 shows the interaction effects of capacitance and feedrate on MRR. MRR can be seen to increase at both ends of the capacitance scale. Somashekhar et al. attributed larger MRR at low capacitance values to the increased number of pulses that were able to be produced per second when the capacitance was reduced, which reduced the pulse on time. Large capacitance values increased MRR for the more obvious reason of increased workpiece heating.

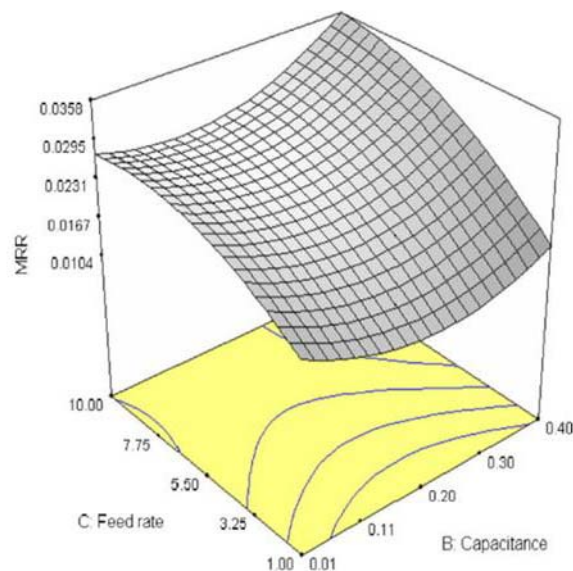


**Figure 2.8: Effect of discharge energy and feedrate on material removal rate in aluminum according to Somashekhar et al. [93]**

Figure 2.9 shows the surface roughness effects from capacitance and feedrate variations. Capacitance is shown to be the dominant factor influencing surface roughness. Increasing capacitance from 0.01 to 0.2  $\mu$ F is shown to decrease surface roughness, while further increases

in capacitance cause an increase in surface roughness. Somashekhar et al. explain that from 0.01  $\mu\text{F}$  to 0.2  $\mu\text{F}$ , the increases in discharge energy result in increased debris in the discharge channel. This debris then dissipates the majority of the discharge energy, actually netting smaller discharge energy at the workpiece surface, resulting in lower surface roughness values. However, above 0.2  $\mu\text{F}$ , the discharge energy becomes high enough to increase the depth of the discharge craters, resulting in increases in surface roughness.

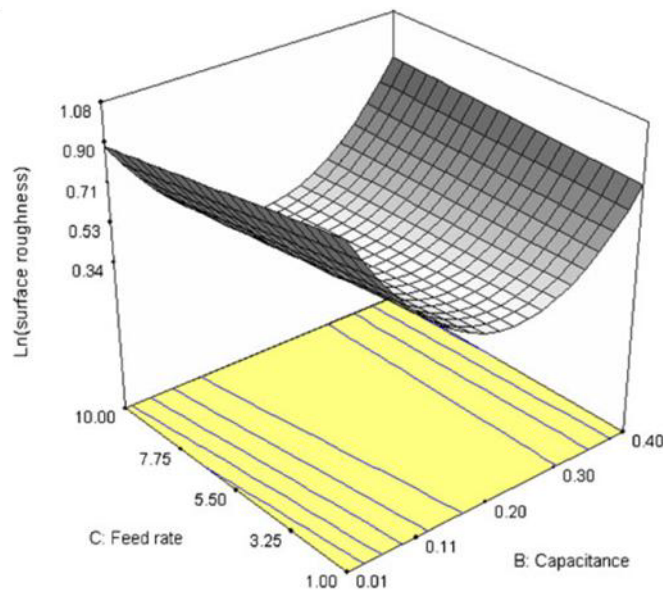


**Figure 2.9: Effect of discharge energy and feedrate on surface roughness in aluminum according to Somashekhar et al. [93]**

The process accuracy is measured by Somashekhar et al. as the amount of overcut present, which is the distance between the electrode and the final machined surface. Larger values of overcut indicate a loss of accuracy in the process as the final workpiece dimensions will deviate from the nominal dimensions by the overcut distance. Figure 2.10 shows that while feedrate has a small effect on the overcut distance, it is the increases in capacitance values that result in the largest increases in overcut distance. Larger capacitance values result in deeper discharge craters, increasing the distance between the final workpiece surface and the cutting electrode.

Overall, Somashekhar et al. concluded that capacitance was the largest single factor influencing MRR, TWR, and process accuracy.

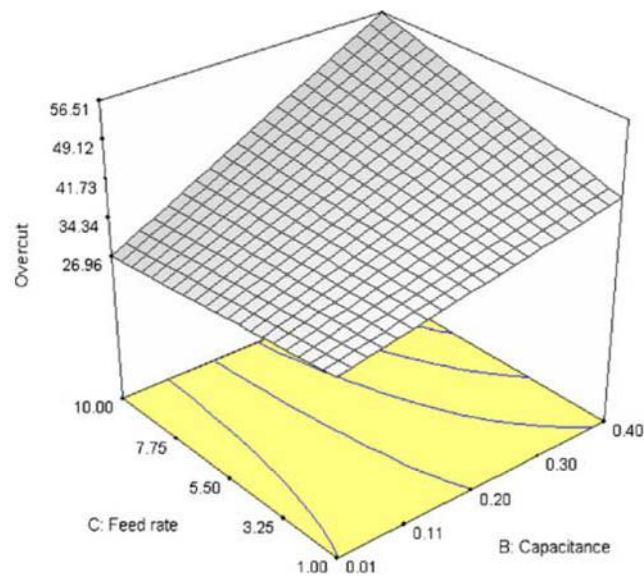


**Figure 2.10: Effect of discharge energy and feedrate on process accuracy in aluminum according to Somashekhar et al. [93]**

Pradhan et al. [7] published their investigations on the effects of current, pulse on-time, and pulse duty cycle on the MRR, TWR, and process accuracy (also measured as amount of overcut present in accordance with Somashekhar et al.) of  $\mu$ -EDM in titanium. Using the Taguchi method, they were able to determine that the pulse on-time had the greatest influence on the MRR and accuracy while the discharge current had the most influence on TWR. MRR and TWR were found to increase monotonically with increases in current as well as increases in pulse on-time up to 10  $\mu$ s, at which point further increases in pulse on-time showed a decrease in MRR.

The increases in MRR and TWR for increasing current and pulse on-time up to 10  $\mu$ s were attributed to the increase in discharge energy density at the workpiece and electrode surfaces, resulting in increased material removal. However, as the pulse on-time increased past 10  $\mu$ s, the

TiC layer thickness on the workpiece surface, which hinders electrical conductivity and thus process stability, was found to increase causing a reduction in MRR. The TWR was not affected by the TiC growth layer, and continued to increase with increasing pulse on-time.

The overcut was found to be most significantly increased by increases in current and pulse on-time. As was described by Somashekhar et al., the increase in energy density with increased pulse current and on-time results in deeper discharge craters, leading to larger distances between the final workpiece surface and the tool electrode. Given desired physical requirements for the  $\mu$ -EDM process, Pradhan et al. was able to use Taguchi analysis to find the optimal machining parameters based on their findings. The results are shown in Table 2.1, where  $I_p$  is the pulse current,  $T_{on}$  is the pulse on-time,  $Pr.$  is the flushing pressure, and  $t$  is the duty cycle.

**Table 2.1: Optimal parameter found by Pradhan et al. for the  $\mu$ -EDM of titanium given a specific physical requirement [7]**

Physical requirement	Optimal combinations ( $I_p/ T_{on}/Pr./t$ )
Higher MRR	1.5 A/10 $\mu$ s/0.5 kg-cm <sup>-2</sup> /95%
Least tool wear rate, TWR	0.5 A/1 $\mu$ s/0.3 kg-cm <sup>-2</sup> /60%
Least overcut, OC	0.5 Amp/1 $\mu$ s/0.1 kg-cm <sup>-2</sup> /60%
Least taper	1.5 A/10 $\mu$ s/0.5 kg-cm <sup>-2</sup> /95%

**Process parameter optimization summary.** The lack of fundamental understanding of the effects of process parameters on machining characteristics in  $\mu$ -EDM makes parameter optimization a difficult avenue to pursue in improving  $\mu$ -EDM performance. In general, the results can be summarized by saying that increases in discharge energy create increases in material removal rates but often with the side effect of increased TWR and decreased process accuracy. Beyond this generalization, results either become contradictory because different materials were tested or inconclusive because identical variables were not studied. For example,

Allen et al. [4] found increases in pulse on-time to decrease tool wear in molybdenum, whereas Sun et al. [9] and Pradhan et al. [7] found increases in pulse on-time to increase tool wear in steel and titanium, respectively. Somashekhar et al. [8] found that the capacitance of the discharge circuit had the largest effect on MRR, however capacitance is related to voltage, current, and pulse on-time, and none of these variables were studied independently. Pradhan et al. [7] found the pulse-on time to have the largest effect on MRR but did not test the effect of discharge circuit voltage or current.

### 2.3.2 Dielectric Selection and Modification

The selection and modification of dielectric fluids can affect the MRR, TWR, and process accuracy by altering the discharge crater characteristics and the workpiece surface chemistry. Typical options for dielectric selection are water-based dielectrics and hydrocarbon based dielectrics, often kerosene. The modification of dielectric fluids is typically done through the addition of suspended powders.

**Dielectric fluid selection.** Kibria et al. [89] recently conducted a comparative study of dielectrics for the  $\mu$ -EDM of titanium alloy. A portion of this study focused on the differences between deionized water and kerosene and their effects on MRR, TWR, and process accuracy (measured as amount of overcut present). Figure 2.11 shows that MRR and TWR increased when using deionized water when compared to kerosene, which is also in agreement with previous studies [11, 12]. The process accuracy was greater at smaller discharge currents when using deionized water, however at larger discharge currents, the trend flipped and kerosene produced better process accuracy results (Fig. 2.11).

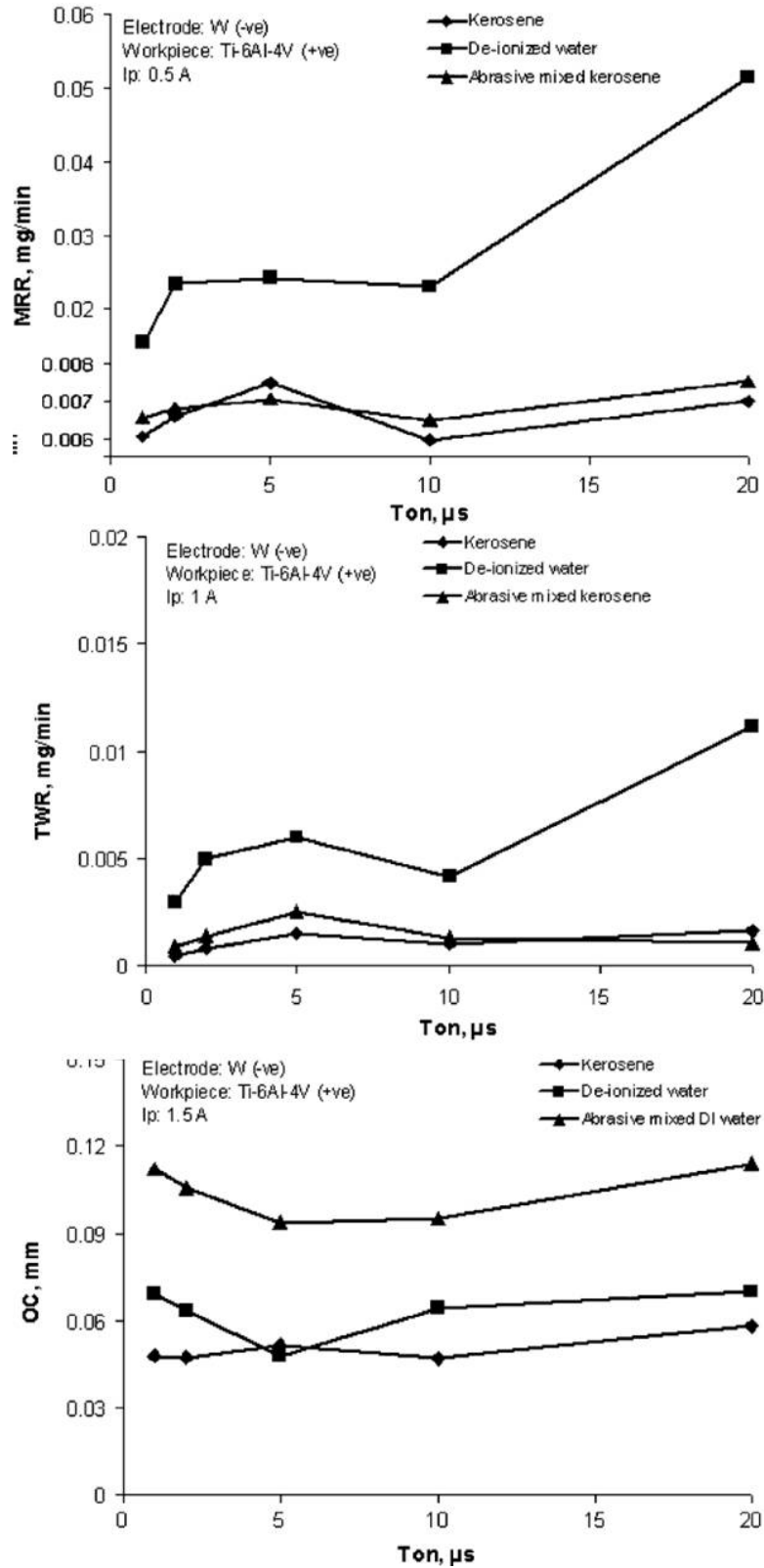


Figure 2.11: MRR, TWR, and overcut results from the differences between deionized water and kerosene as the dielectric in  $\mu$ -EDM [89]

Kibria et al. [89] concluded that the increases seen in MRR and TWR when using deionized water versus kerosene were due to the formation of oxides on the workpiece surface with deionized water instead of the higher melting temperature carbides that form with kerosene dielectrics, which is in agreement with conclusions made in previous studies by Wang et al. [11] and Lin et al. [12]. Carbides formed on the workpiece surface when using kerosene decrease MRR and TWR because their higher melting temperature helps resist the thermal effects of the discharge process. Lin et al. also provided an alternative explanation for the differences in MRR between the two dielectrics. They claimed the formation of floating ‘carbon elements’ in the hydrocarbon dielectric during a discharge increase the viscosity of the dielectric and cause debris to clump together and clog the machining gap, decreasing the MRR. The higher MRR for water was explained by an increase in explosive force by the spark discharge with the addition of hydrogen and oxygen to the discharge channel from the disassociated water molecules [12].

The increase in process accuracy reported by Kibria et al. at small discharge energies and the decrease at larger discharge energies with deionized water dielectrics was attributed to secondary sparking promoted by disassociated oxygen molecules in the dielectric. At low discharge energies, these secondary sparks reduced machining time over kerosene-based processes, which helped to reduce process inaccuracies as the tool had less machining time to cause dimensional inaccuracies. However, at high discharge energies, the secondary discharges were powerful enough to produce significant overcutting of the workpiece surface, resulting in increased dimensional inaccuracies when using deionized water as the dielectric.

**Dielectric fluid modification.** The addition of suspended powders to the dielectric fluid in  $\mu$ -EDM has been investigated as a possible means of improving the machining characteristics of  $\mu$ -EDM. Chow et al. conducted two similar studies, one on the addition of aluminum powders

and silicon carbide to kerosene [14], and another on the addition of silicon carbide to water [17] in the micro-slit cutting of titanium. They concluded that in general, the addition of powders to the dielectric fluid in  $\mu$ -EDM increased the conductivity of the fluid, thereby expanding the inter-electrode gap, as shown in Fig. 2.12. This had the positive effect of improving debris flushing as well as dispersing the discharge into multiple smaller pulses. The theory of dispersing discharge energy in powder-mixed dielectrics was also suggested by Yeo et al. [16] in a similar study as well as by Prihandana et al. in a study using  $\text{MoS}_2$  powder [18].

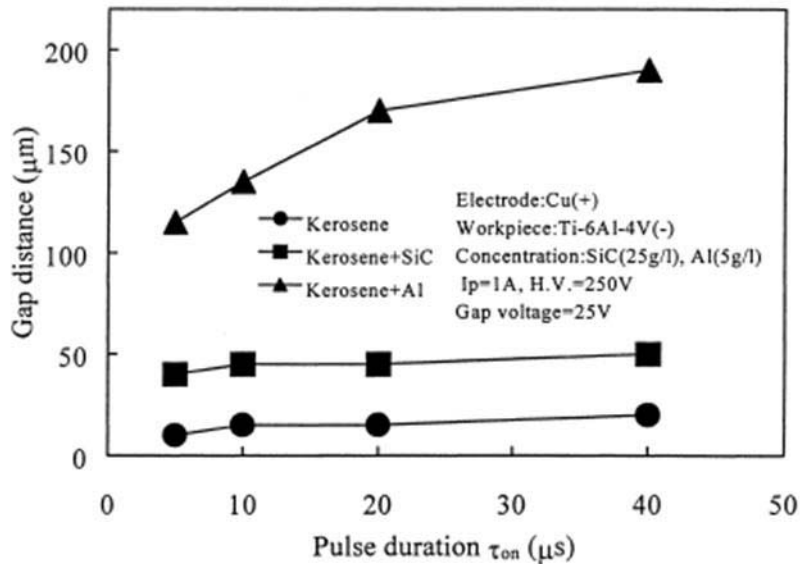


**Figure 2.12: Effect of powders on gap distance [14]**

Chow et al. found that the powders increased TWR in both studies (Fig. 2.13). When kerosene was used as the base dielectric, the increased tool wear was attributed to the powders preventing carbon buildup on the electrode, therefore expediting erosion because of the loss of insulation the carbon normally provides. The reduction in workpiece surface layer thicknesses when using powder-mixed dielectrics was also reported by Kocke et al. [15] in a similar study.

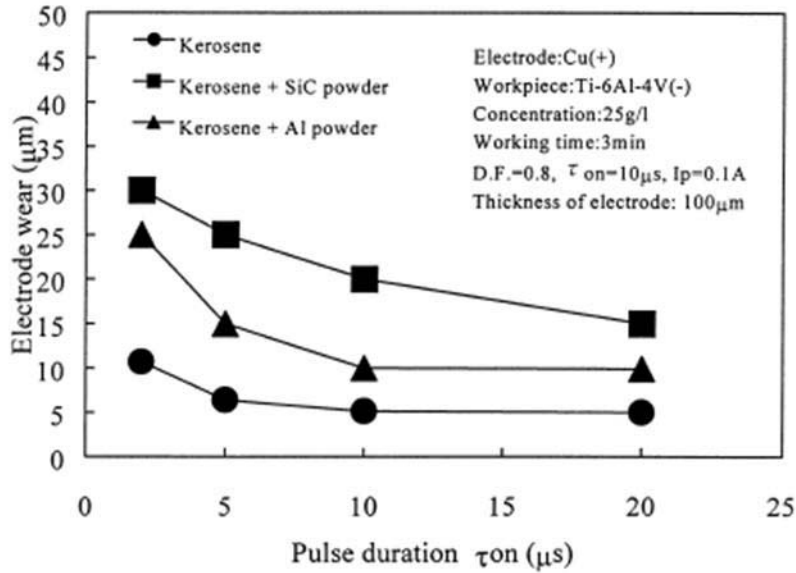


**Figure 2.13: Effect of powders on electrode wear [14]**

Figure 2.14 shows that MRR increased in the studies conducted by Chow et al. [17] with the addition of powders as a result of the larger gap distance which enhanced debris flushing. Prihandana et al. also reported enhanced MRR when using powder-mixed dielectrics but claimed it was a result of an increase in discharge frequency caused by the presence of the powder [18].

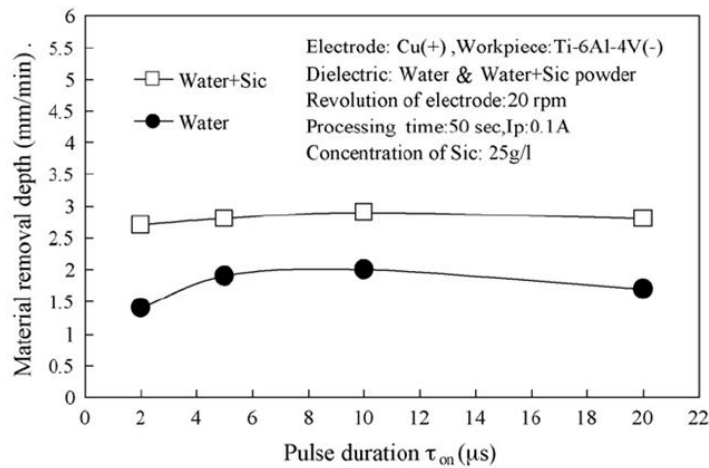


**Figure 2.14: Effect of SiC powder in water on MRR [17]**

**Dielectric selection and modification summary.** The use of water as a dielectric has been definitively shown to improve MRR in  $\mu$ -EDM, however the TWR has largely been shown to increase as well. The addition of powders to the dielectric fluid has been shown to improve

MRR by increasing the electrical conductivity of the fluid, thereby increasing the discharge gap and improving debris flushing. However, the powders in the dielectric can interfere with carbon deposition on the electrode surface, resulting in increased TWR in powder-mixed dielectrics.

### 2.3.3 Debris Removal

**Ultrasonic-assisted debris removal.** Currently the most widely used technique to improve debris flushing in  $\mu$ -EDM is through the addition of ultrasonic (US) vibrations to the process. Two major avenues have been pursued in the US vibration-assisted  $\mu$ -EDM process, workpiece vibration and tool vibration, as well as a third option that has shown minor support- dielectric fluid vibration. The vibrations can cause a pumping action in the inter-electrode gap to improve debris movement from the gap [26], and it has also been theorized that the US vibrations produce cavitation in the electrode gap, accelerating the ejection of molten material from the discharge crater to minimize the re-cast and heat-affected layers [24].

The use of US vibrations to increase MRR has been widely documented [24-28, 30, 32-33, 94, 98, 100]. Yeo et al. [94] first reported using US vibrations to increase aspect ratios of  $\mu$ -EDM drilled holes from 6:1 to 14:1. Figure 2.15 shows the differences reported in MRR during a study by Gao et al. [25] on the through-hole  $\mu$ -EDM drilling of both stainless steel and copper. The increases seen in MRR were attributed to enhanced debris removal from the discharge gap.

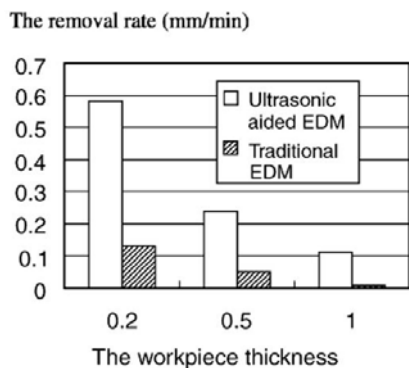


**Figure 2.15: Effect of US vibrations on MRR in  $\mu$ -EDM [25]**

The US vibrations have also been shown to improve process stability in  $\mu$ -EDM [30, 32, 98, 100] as well as process accuracy [24, 25, 28, 32, 95, 96]. Yeo et al. [95] reported increased process accuracy in the form of a reduction in surface roughness of nearly 9% from 394 nm  $R_a$  to 313 nm  $R_a$ . Tong et al. [32] reported a direct increase in machining accuracy of 10.5  $\mu\text{m}$  by measuring the difference between nominal and machined dimensions on a US-assisted  $\mu$ -EDM part.

Ultrasonic vibration has been incorporated with other  $\mu$ -EDM innovations in an effort to further improve the process. Yu et al. [34] combined planetary electrode movement with US vibration but found that the combination was detrimental to the machining characteristics. The US workpiece vibrations alone were found to increase MRR and decreased tool wear, but when combined with planetary electrode movement, the MRR decreased and tool wear increased relative to the normal  $\mu$ -EDM process.

Hung et al. [28] developed a technique for  $\mu$ -EDM hole drilling in high nickel alloy using a helical electrode and ultrasonic vibrations to reduce the machining gap, improve machining times, and improve surface quality. Jia et al. [33] showed the possibility of inverting the typical  $\mu$ -EDM hole drilling setup to use gravity to assist debris removal and paired it with ultrasonic electrode vibration to further improve debris flushing and machining speed in the  $\mu$ -EDM of stainless steel.

Kim et al. [29] experimented with exciting the dielectric bath in  $\mu$ -EDM using an ultrasonic transducer and reported a reduction in secondary discharges and decreased TWR as a result. In the straight hole  $\mu$ -EDM drilling through steel, they found that paring ultrasonic bath vibration with a method of varying capacitance throughout the drilling process could produce a straight micro-hole with a diameter variation of less than 1  $\mu\text{m}$  over a workpiece thickness of 500  $\mu\text{m}$ .

Prihandana et al. [18] also used ultrasonic dielectric bath vibration in conjunction with powder-mixed dielectrics in  $\mu$ -EDM and reported the ultrasonic vibrations alone were a significant factor in the increased MRR reported due to the reduced adhesion of debris to the workpiece surface.

**Magnetic field-assisted debris removal.** While ultrasonic-assisted debris removal is currently the most widely used debris removal technique in  $\mu$ -EDM, a few other techniques have been investigated for improving debris removal in  $\mu$ -EDM. However, all but magnetic field-assisted debris removal have failed to produce increases in  $\mu$ -EDM MRR. Bamberg et al. [22] investigated orbital tool movement in  $\mu$ -EDM hole drilling of steel to improve debris flushing. They found a reduction in TWR and surface roughness, and reported that they were able to eliminate the inherent exponential reduction in MRR normally seen in  $\mu$ -EDM hole drilling as depth increases. However, overall MRR was not shown to significantly increase beyond levels normally seen at the beginning of a hole drilling process. Wang et al. [11] experimented with forced dielectric fluid flushing through the discharge gap during the die-sinking operation of heat sink fins in tungsten carbide plates. They found that the forced dielectric flushing generally decreased process stability due to turbulence in the small inter-electrode gap in all but the lowest of flushing pressures, making it an ineffective technique to improve MRR in  $\mu$ -EDM.

Of particular interest though is Yeo et al. [35], who was able to utilize magnetic fields during  $\mu$ -EDM hole drilling in steel to improve debris circulation. The use of magnetic fields to aid in debris circulation is not a new topic. De Bruijn et al. [130] first suggested the application of magnetic fields for gap cleaning in EDM in 1978. More recently, Lin et al. [131-132] was able to link enhanced debris removal from the application of magnetic fields in macro-scale EDM to

an increase in MRR. They observed that for a magnetic material, the MRR increased nearly three times that of a hole cut without the magnetic field.

The magnetic field-assisted debris removal technique in these studies depends on the debris particles being ferromagnetic. A ferromagnetic debris particle can be considered to behave as a dipole in the presence of a non-uniform magnetic field, thus Yeo et al. and others were able to exert a force on the debris particles in the dielectric fluid to improve their ejection from the discharge gap. Yeo et al. reported that the magnetic field-assisted debris removal technique, when applied to  $\mu$ -EDM, resulted in a 26% increase in MRR, as shown in Fig. 2.16. However, the magnetic field also induced a distortion in the tool electrode, causing increased wear along the length of the tool during the operation.

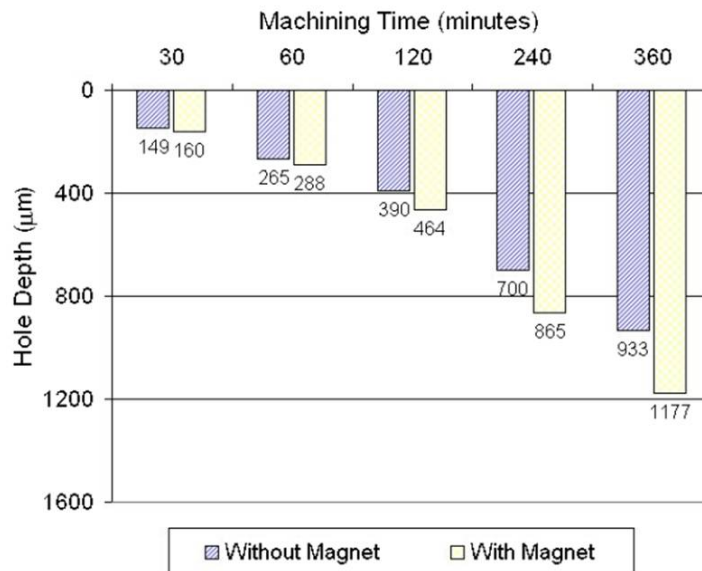


**Figure 2.16: Effects magnetic field-assisted debris removal on MRR in  $\mu$ -EDM [35]**

**Debris removal summary.** The effective flushing of debris from the inter-electrode gap in  $\mu$ -EDM processes is essential for machining stability. In general, the addition of ultrasonic vibrations has been shown to increase process stability and MRR, as well as increasing process accuracy and reducing surface roughness. The implementation of orbital electrode movement

appears to stabilize debris flushing in deep hole  $\mu$ -EDM drilling [22]. The use of forced dielectric flushing in the inter-electrode gap has also been tried, however the results do not appear promising as the flushing technique implemented resulted in significant process instability [11]. The use of magnetic fields has shown promise to increase MRR, as evidenced by a 26% increase in MRR reported by Yeo et al. [35], however this technique requires the workpiece material to possess ferromagnetic properties.

## 2.4 Magnetic Field-Plasma Interaction

### 2.4.1 General Use of Magnetic Fields in Plasma Applications

The material removal mechanism discussed in Section 2.2.1 has a large dependence on the plasma channel in its operation. The thermal energy required for heating and vaporization of the workpiece material is provided by the plasma channel and the collapse of the plasma channel is suspected to be largely responsible for the removal of molten material from the workpiece melt pool at the end of a discharge. As a result, changes in the plasma channel characteristics may have a large effect on the material removal mechanism.

The use of magnetic fields to influence plasma behavior has been central to plasma research since the 1950's and remains a topic of great interest today [101]. Much of the magnetic field-plasma interaction research interest has been in the confinement and stabilization of plasmas generated for sputtering applications, X-ray source applications, and plasma torch applications. Plasma confinement is useful in creating high density plasmas, often for the purpose of generating X-rays [133]. Confined plasmas also possess a higher current density than standard plasmas, increasing anode and cathode spot heating, which is useful in sputtering applications [104]. Plasma stabilization is critically important in the development of plasma torches used in

surface processing techniques, as an unstable arc creates unpredictable and uneven surface heating [109]. Unfortunately, the investigation of magnetic field effects on  $\mu$ -EDM plasmas has not been previously studied.

Plasmas produced in  $\mu$ -EDM are different from most other plasmas as the gap distance often approaches the same length as the sheath thickness and/or Debye length, causing the plasma to organize itself differently from traditional macro-gap discharge plasmas [66]. As a result, no direct comparisons can be drawn between current magnetic field-plasma interaction studies and how  $\mu$ -EDM plasmas may behave in the presence of magnetic fields. However, by examining research into plasma confinement and stabilization of plasmas that possess somewhat similar characteristics to the plasmas produced in  $\mu$ -EDM, hypotheses can be made about how magnetic fields may affect the  $\mu$ -EDM plasma. Current research with the closest relation to  $\mu$ -EDM applications is that which focuses on plasmas produced from direct current arcs at or near atmospheric pressure and interacting with magnetic dipoles.

## 2.4.2 Optical Emission Spectroscopy

In order to determine changes in plasma characteristics, spectroscopic measurement techniques are often utilized to obtain plasma temperature and electron density data, two of the primary characteristics that define a plasma [66]. Plasma temperature is determined by the line-pair method (Eq. 2.1), a widely used plasma temperature estimation technique that compares the relative intensities of two spectral peaks and has been shown to determine plasma temperature with an estimated 20% error [121], i.e.,

$$T = \frac{-(E_1 - E_2) / k}{\ln \left( \frac{I_1 \lambda_1 g_2 A_2}{I_2 \lambda_2 g_1 A_1} \right)}. \quad (2.1)$$

In Eq. 2.1,  $E_n$  is the excitation energy of the spectral line  $n$ ,  $k$  is the Boltzman constant,  $I_n$  is the intensity of the spectral line  $n$ ,  $\lambda_n$  is the wavelength of line  $n$ ,  $g_n$  is the statistical weight of line  $n$ , and  $A_n$  is the transition probability of line  $n$ .

Electron density can be found by measuring the  $H_\alpha$  (656.28nm) spectral line broadening, another common spectroscopic technique for plasma analysis [66, 123]. The FWHM (Full-Width Half-Maximum) of the  $H_\alpha$  line can be directly correlated to electron density using Eq. 2.2 [66]:

$$n_e = 8.8308 \cdot 10^{16} \cdot (\Delta\lambda_w)^{1.6005} \quad (2.2)$$

where  $n_e$  is the electron density in  $\text{cm}^{-3}$  and  $\Delta\lambda_w$  is the width of the  $H_\alpha$  line measured at FWHM in nm. After determining the plasma temperature and electron density, it is possible to calculate the coupling factor  $\Gamma$ , the mean inter-particle distance  $a$ , and the Debye length  $\lambda_D$  [66].

The coupling factor  $\Gamma$  describes the ratio of the potential energy of Coulomb interactions between particles to the thermal energy of the particles in the plasma. If  $\Gamma \ll 1$ , the plasma is labeled as ideal and indicates that all particles in the plasma are free to move and electrostatic interactions between particles are minimal. Ideal plasmas are typically very hot with a low density. For a non-ideal plasma ( $\Gamma \leq 1$ ) as well as a strongly coupled plasma ( $\Gamma > 1$ ), the inter-particle distances are very small, which leads to high electrostatic interactions between particles.

The Debye length  $\lambda_D$  describes the distance over which charge shielding occurs and gives insight into the cause of plasma ideality. The Debye length is important relative to the inter-particle distance  $a$  in the sense that when  $\lambda_D \gg a$  (an ideal plasma), many particles are present within the distance required for charge shielding. Only a few particles are actually needed for charge shielding, and as a result, the remaining particles are free to move around free from interaction with each other.

However, if  $\lambda_D \approx a$  (a non-ideal plasma), few particles are present within the Debye length, resulting in a majority of particles in the plasma tied up in electrostatic interactions with one another. Because electrostatic forces are present between nearly all particles in non-ideal plasmas, magnetic fields may have less of an effect on non-ideal plasmas as the electrostatic forces likely dominate the magnetic forces.

### 2.4.3 Use of Magnetic Fields for Plasma Confinement

Magnetic fields applied perpendicular to an electrode surface, sometimes also referred to as axial magnetic fields due to the coaxiality of magnetic field lines with the electric field lines in the inter-electrode gap, likely confine the plasma based on the Larmor radius principle. In the presence of a uniform magnetic field, electrons will travel in helical paths along the field lines with a radius equivalent to the Larmor Radius,

$$r_g = \frac{mv_{\perp}}{|q|B} \quad (2.3)$$

where  $m$  is the mass of the electron,  $v$  is the velocity component of the electron perpendicular to the direction of the field line,  $q$  is the charge of the electron, and  $B$  is the field strength. If the Larmor radius is small in comparison to the radius of the plasma, electrons are confined [102].

Keidar et al. [102] and Beilis et al. [103] conducted a simulation on the confinement effects of an axial magnetic field on a DC arc produced in vacuum. They concluded that the self-induced azimuthal magnetic fields from a normal DC arc are not sufficient for confinement at low currents [103]. However, if an externally applied axial magnetic field was introduced to the plasma, the radial plasma velocity was found to decrease [102]. This indicates the existence of plasma confinement as a normal arc without an axial magnetic field present develops equal radial and axial plasma velocities.

Rondanini et al. [104] conducted both modeling and testing of a low vacuum DC plasma in the presence of an axial magnetic field and found the electron density to increase with increasing field strength (Fig. 2.17). Wilson et al. [105] tested a low vacuum DC micro-plasma in an axial magnetic field and found the plasma current to increase in the presence of the magnetic field. Higher currents likely correspond to increases in electron density as the current is a measure of the flow of charges through the plasma channel and the magnetic field is not found to increase axial plasma velocity in any other studies, thus the electron density may be increasing if an increase in current is measured. Both Rondanini et al. and Wilson et al. show promising results that point towards successful plasma confinement through the use of axial magnetic fields.

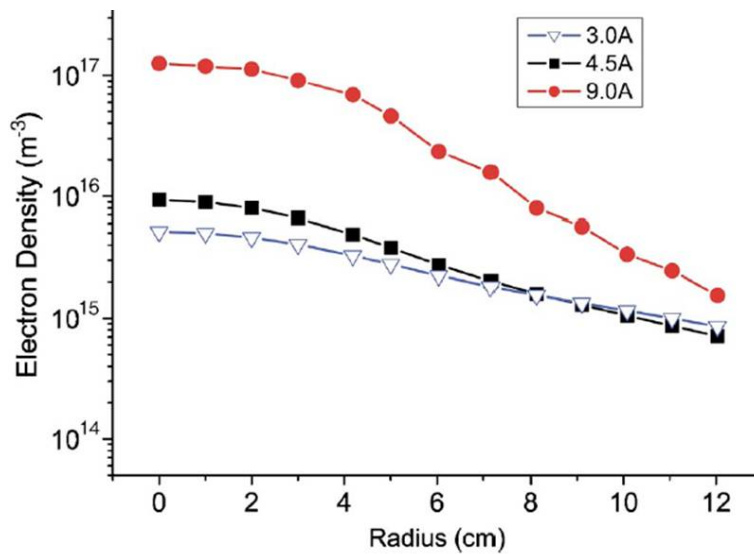


**Figure 2.17: Effect of electromagnetic current on plasma density throughout plasma radius. Higher current values correlate to higher magnetic field strengths [104]**

Hassouba [106] examined the electron temperature and density of a DC plasma produced in a vacuum in the presence of an axial magnetic field. Testing revealed a decrease in electron temperature, as seen in Fig. 2.18, and an increase in electron density, as seen in Fig. 2.19, in the presence of an axial magnetic field. Hassouba suggested that the confinement produced by the magnetic field increased the plasma density, but at the same time this produced more electron

collisions in the plasma, lowering the overall energy of the electrons, which appears as the observed decrease in temperature.

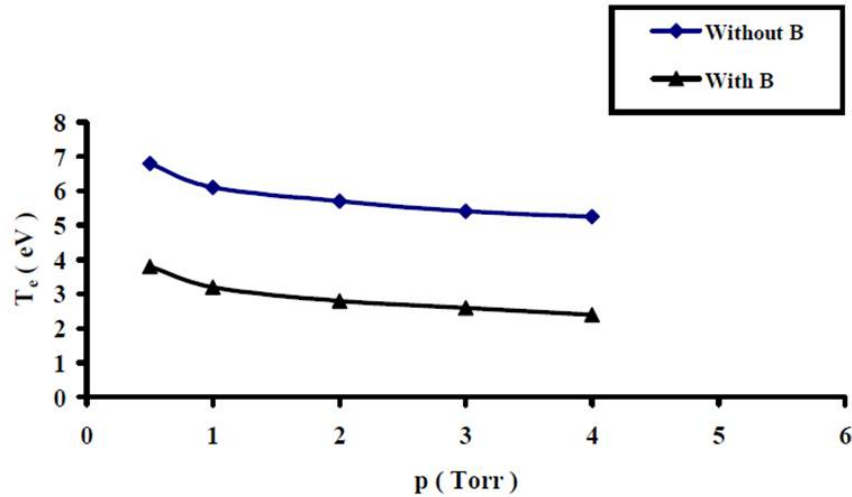


Figure 2.18: Effect on an axial magnetic field on plasma electron temperature [106]

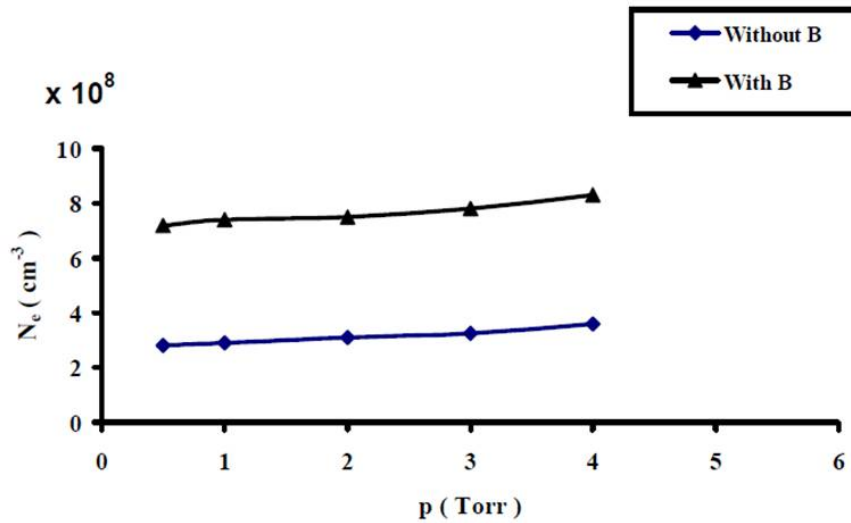


Figure 2.19: Effect on an axial magnetic field on plasma electron density [106]

#### 2.4.4 Use of Magnetic Fields for Plasma Stability

The use of magnetic fields to increase plasma stability has been around since at least 1957, when Taylor [107] modeled the use of axial magnetic fields to successfully stabilize an arc inside of a gas filled cylinder. More recently, Kotalik et al. [108] modeled a DC arc in the presence of

an axial magnetic field and reported observing a decrease in electron turbulence at the electrode faces, creating a more stable arc discharge channel. The additional stability seen in plasmas subjected to perpendicular magnetic fields is said to originate from the suppression of a recirculation zone that appears in the front of the cathode when no magnetic field is applied [108]. Unaided, electrons flow randomly between the cathode and anode [66] and form recirculation zones caused by weak self-induced magnetic fields from the plasma current in front of the electrode faces [108]. However, when perpendicular magnetic fields are applied, the azimuthal component of the plasma velocity substantially increases, creating a centrifugal force in the plasma that stabilizes it and removes the recirculation zones in front of the electrodes [108].

Kim [109] reported successfully implementing a transverse magnetic field to suppress electron turbulence and increase arc stability in a DC plasma produced at atmospheric pressure in a plasma torch. Stability was measured by monitoring voltage fluctuations at the anode. It was reported that the addition of the transverse magnetic field decreased arc instabilities by 28.6%. This could be of use in EDM discharges, as Rehbein et al. [110] reported movement of the discharge channel during observation of single pulse discharges (Fig. 2.20). Increasing the stability of the discharge channel to reduce this movement may improve the EDM process.

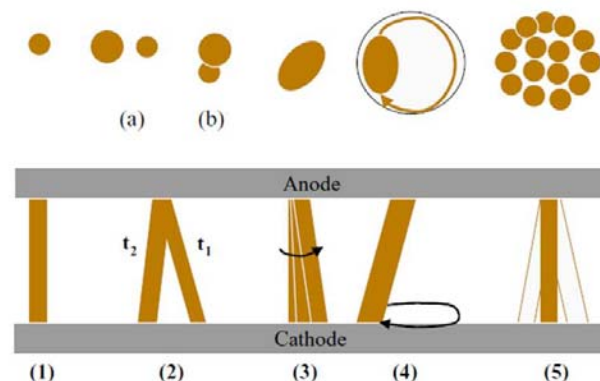


**Figure 2.20: Examples of the different structures of discharge channels observed during single discharge pulses [110]**

## 2.4.5 Extending Magnetic Field Effects to $\mu$ -EDM

**Perpendicular Magnetic Fields.** Magnetic fields applied perpendicular to the workpiece surface have been shown in Section 2.4.3 to successfully confine DC plasmas produced in a vacuum and in Section 2.4.4 to successfully stabilize similar DC plasmas. Extending successful confinement or stability techniques to  $\mu$ -EDM plasmas may increase current density at the workpiece surface by creating smaller discharge spots that migrate less, yielding more efficient material removal or more consistent discharge crater characteristics.

**Use of Lorentz Force.** The use of Lorentz forces to influence  $\mu$ -EDM material removal mechanics is a new concept that allows the use of magnetic fields in conjunction with non-magnetic materials to theoretically add additional force acting on the melt pool during a spark discharge. Lorentz forces develop when a current-carrying element is subjected to an externally applied magnetic field. The Lorentz force is given by the cross product of the current with the magnetic field:

$$F = J \times B \quad (2.4)$$

where  $J$  is the current per unit area [ $A/mm^2$ ] and  $B$  is the magnetic field [T]. In the case of  $\mu$ -EDM, the current-carrying element is the workpiece melt pool, so a properly oriented magnetic field can result in the development of Lorentz forces in the melt pool.

Research conducted by Amson [111] has shown that molten material droplets produced by a plasma interacting with an electrode are removed with the help of a self-induced Lorentz force that fluctuates from negative to positive and back to negative during droplet formation (Fig. 2.21). The addition of an external Lorentz force in  $\mu$ -EDM would alter this force curve and may increase the number of molten droplets that detach from the workpiece material to become debris, thus improving MRR. Additionally, Gallet et al. [112] has shown magnetic fields to

dampen turbulence in molten metal pools, which may help stabilize the material removal process in  $\mu$ -EDM and create more consistent crater geometries.

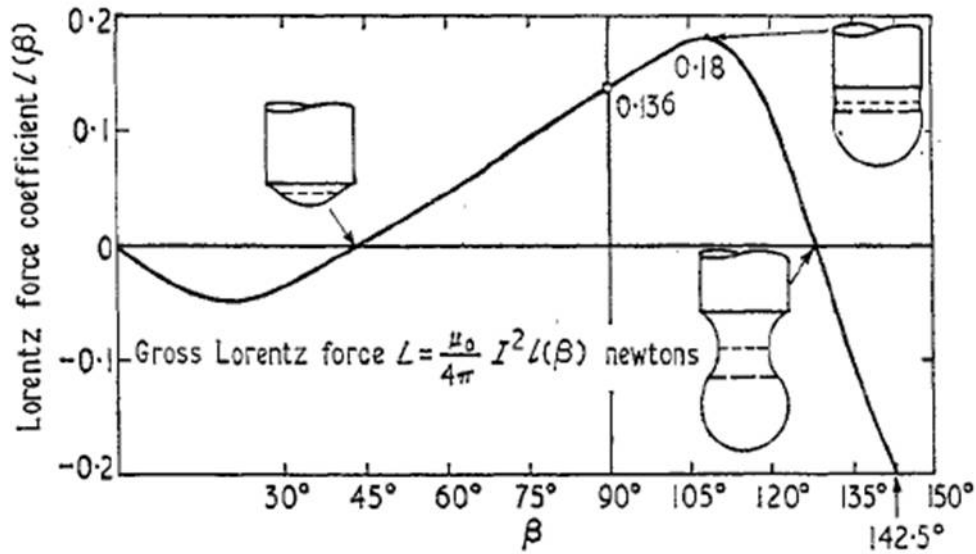


Figure 2.21: Gross Lorentz force seen on a molten droplet forming at the end of an electrode [111]

## 2.5 Gaps in Knowledge

Many industrial applications exist for  $\mu$ -EDM, however the current material removal rates of 0.6-6 mm<sup>3</sup>/hour are below the desired industry minimum levels of 10-15 mm<sup>3</sup>/hour, preventing widespread use of  $\mu$ -EDM. Attempts have been made to improve MRR through parameter optimization, dielectric selection and modification, and debris removal; however, shortcomings associated with each approach have left the industry short of its goal.

A complete understanding of all the interaction effects between process parameters and the machining characteristics does not currently exist, limiting their widespread use for enhancing MRR in industrial applications. Due to the thermal nature of the material removal mechanism in  $\mu$ -EDM, the problem of mapping the interaction effects of the process parameters to the

machining characteristics is exacerbated by the requirement to extend these relationships to include changes in workpiece thermal properties. The resulting optimization problem is prohibitively complicated and not a method of choice to implement industry-wide increases in MRR in  $\mu$ -EDM.

Dielectric selection and modification, as well as current debris removal techniques, have been shown to improve MRR to an extent, but still fall significantly short of the industry desired increases in MRR of over 100% to 10-15 mm<sup>3</sup>/hour. The use of magnetic fields to improve MRR in  $\mu$ -EDM has been explored previously with success, improving MRR by an appreciable 26%; however, the technique was limited to magnetic workpiece materials based on the principles used. The development and testing of a magnetic field-assisted  $\mu$ -EDM technique that is both significantly more effective as well as functionally independent of workpiece magnetic properties is required to determine the viability of using magnetic fields to solve the MRR discrepancy between the industry and what can currently be provided in  $\mu$ -EDM.

The effects of applied magnetic fields on  $\mu$ -EDM plasma characteristics have not been investigated. Applications of magnetic fields to other plasmas have been shown to improve plasma confinement [102-106] and reduce plasma instability [107-109]. Plasma confinement is the most direct way to increase the energy density in a  $\mu$ -EDM discharge, which increases the thermal efficiency of the material removal technique, thus improving the MRR of the process. Increasing plasma stability is equally important in improving energy density as the  $\mu$ -EDM process is plagued by discharge instability, resulting in low discharge energy density as the plasma column moves around the workpiece surface [110]. The possibility for utilizing magnetic fields to improve plasma confinement and/or plasma stability in  $\mu$ -EDM plasmas needs to be investigated. It is hypothesized that perpendicular magnetic fields will confine the  $\mu$ -EDM

plasma, resulting in smaller diameter and deeper discharge craters that improve process MRR regardless of workpiece magnetic properties.

The use of Lorentz forces to affect the material removal mechanism in  $\mu$ -EDM has also not been investigated. Self-induced Lorentz forces have been shown to play a role in the removal of molten droplets from electrodes in plasma discharges at the macro-scale [111]. Altering the forces present during droplet separation in  $\mu$ -EDM through the introduction of additional Lorentz forces may alter the material removal mechanism. It is hypothesized that the addition of externally applied Lorentz forces to the melt pool during a  $\mu$ -EDM discharge will increase the productivity of the discharge, and thus the MRR of the process, without a dependence on workpiece magnetic properties.

# Chapter 3

## Exploratory Testing in Magnetic Field-Assisted $\mu$ -EDM for Non-Magnetic Materials

This chapter will discuss proof-of-concept experiments on methods developed for improving MRR in  $\mu$ -EDM for non-magnetic materials through the use of magnetic fields in order to fill the gap in knowledge that exists for such a technique. Two avenues will be explored; alteration of the discharge plasma channel through the use of magnetic fields to affect plasma confinement and/or plasma stability, and the development of a unique magnetic field-assisted  $\mu$ -EDM process to improve the material removal mechanism through the use of Lorentz forces induced in the melt pool. To understand the effects of these techniques on the fundamental mechanics of the  $\mu$ -EDM process, the investigation will focus on the process at the single spark discharge level.

As a result of the new processes that will be investigated and the metrics that will be used to characterize changes in the process mechanics during these investigations, a unique testbed topology is required. This testbed will be designed and built for experimental testing of magnetic field-assisted  $\mu$ -EDM techniques for non-magnetic materials and the spark discharges will be controlled by a purpose-built hybrid RC-transistor single-spark discharge circuit. Preliminary single-spark discharge experiments will then be run on the magnetic field-assisted  $\mu$ -EDM techniques developed to explore the feasibility of altering plasma channel confinement and/or stability as well as using Lorentz forces to affect the material removal mechanism in the  $\mu$ -EDM of non-magnetic materials. Metrics to be used in the characterization of these

techniques include discharge crater area analysis, high-speed imaging of the spark discharge process, discharge crater volume analysis, and erosion efficiency analysis. Tool wear will also be examined in these experiments by surface chemistry analysis.

### 3.1 Magnetic Field-Assisted Micro-EDM for Non-Magnetic Materials Concept Development

Non-magnetic materials inherently do not experience any force in the presence of a magnetic field. However, if additionally a directional current is flowing through the non-magnetic material, such as through the  $\mu$ -EDM workpiece seen in Fig. 3.1, a Lorentz force is developed as the cross product of the current with the magnetic field, as seen in Eq. 2.4. When the two components are set perpendicular to one another, the Lorentz force is maximized in a direction that is mutually perpendicular to both the current vector and the magnetic field vector.

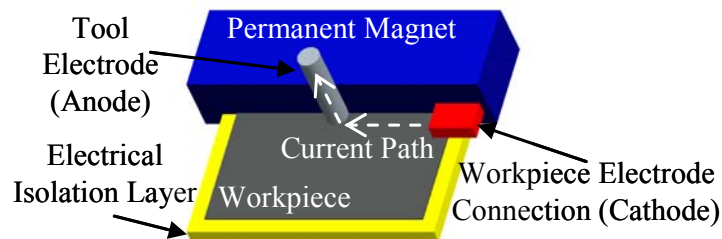


**Figure 3.1: Schematic of parallel magnetic field with directional current  $\mu$ -EDM setup**

It is proposed that the presence of an externally applied Lorentz force pointing into the melt pool will enhance MRR by adding to the existing force produced by the plasma channel on the melt pool, which is a component of the material removal mechanism used to eject melt material from the discharge crater [52]. The possibility will also be investigated of improving MRR by orienting the Lorentz force outward from the melt pool to assist the internally produced Lorentz forces that affect droplet separation from the melt pool [111].

During a typical  $\mu$ -EDM discharge, current flows normal to the workpiece surface in the plasma channel but disperses isotropically once it enters the workpiece. By applying a parallel magnetic field in this configuration, defined as a magnetic field parallel to the workpiece surface, Fig. 3.2 shows that a Lorentz force  $F_2$  resulting from the current in the plasma channel  $J_2$  can be produced at the surface of the melt pool before the current disperses; however, this force acts parallel to the melt pool surface, not perpendicular as desired in the proposed process to direct the additional force into or out from the workpiece surface.

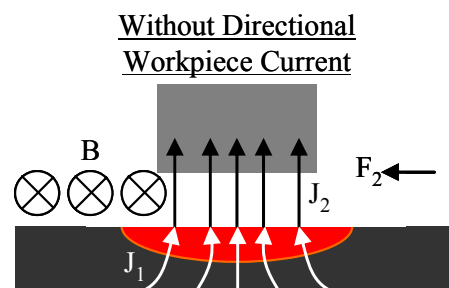


**Figure 3.2: Discharge current in the melt pool during a typical spark discharge and the resulting Lorentz force that develops in the presence of a parallel magnetic field**

In order to produce a Lorentz force perpendicular to the melt pool surface, changes need to be made to the typical current path in  $\mu$ -EDM. If the current is given a preferential direction in the workpiece by providing a low resistance path as depicted in both the 2D and 3D figures in Fig. 3.3, an additional Lorentz force is developed, force  $F_1$  from current direction  $J_1$ , which acts on the melt pool in the same way a Lorentz force acts on a current-carrying wire in a magnetic field. The actual direction of the current  $J_1$  in the melt pool will be a combination of the overall current direction in the workpiece ( $J_1$ ) and the current direction in the plasma channel ( $J_2$ ), thus the resulting force vectors  $F_1$  and  $F_2$  will combine to produce a force in the melt pool  $F_R$ , as seen in Fig. 3.3. For clarification,  $J_1$  and  $J_2$  are two designations for the same discharge current, used to differentiate between current in the plasma channel and current in the workpiece.

With Directional Workpiece Current

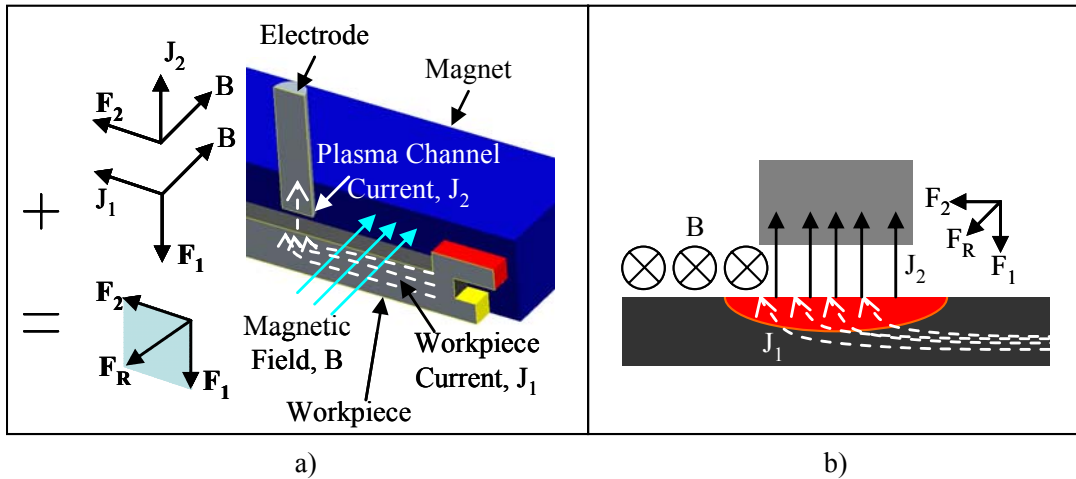


**Figure 3.3: a) 3D and b) 2D depictions of the directional discharge current in the melt pool and the resulting Lorentz forces that develop in the presence of a parallel magnetic field**

By controlling the directionality of the magnetic field, it is possible to control the direction of the Lorentz force. Figure 3.3 shows the configuration where  $F_1$  is pointing into the workpiece surface; however the magnetic field direction can be reversed  $180^\circ$  to direct the Lorentz force outward from the workpiece. The time required for the Lorentz force to develop is dictated by the timing of the current pulse during a discharge. Figure 3.4 shows a time resolved plot of a current pulse characteristic of those used in this thesis. The pulse is initiated just before the  $1.2\mu\text{s}$  mark on the x-axis, followed by approximately  $200\text{ns}$  of delay before the current reaches a value of  $6\text{-}8\text{A}$  for the remainder of the discharge. The timing and magnitude of the Lorentz force developed would follow the form of the current pulse based on Eq. 2.4.

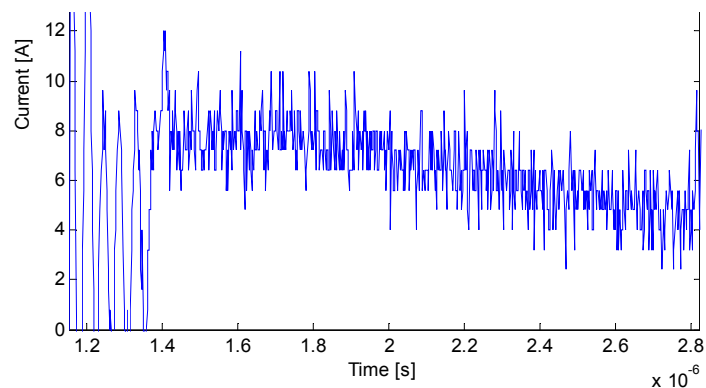


**Figure 3.4: Typical single-shot spark current pulse**

## 3.2 Testbed Design

### 3.2.1 Testbed Design Requirements

The proposed study on the fundamentals of magnetic field interactions with  $\mu$ -EDM plasmas as well as the testing of the Lorentz force technique developed several special requirements for both the testbed topology and discharge circuit. In the investigation of the use of magnetic fields without directional workpiece current, the perpendicular magnetic fields are to be investigated for signs of plasma confinement and enhanced stability. This requires the use of high-speed camera imaging and spectroscopic imaging to measure the process metrics developed. As a result, the  $\mu$ -EDM testbed was required to be light and compact enough for transport, as the size of the high-speed camera equipment required the testbed be brought to it rather than the camera be brought to the testbed. The testbed also needed to have unrestricted optical access only a few centimeters from the discharge location due to short working distances on the optics used.

The Lorentz force technique required that the workpiece be insulated from the surrounding structure in order to develop a directional current in the melt pool. Also, all components near the discharge area were required to be non-magnetic to eliminate unwanted forces between the magnets to be used in testing and the testbed structure that could affect positioning accuracy. Finally, the placement of the magnets was critical in these experiments, as permanent magnets have field strengths that drop off quickly as you move away from the surface of the magnet, thus the magnets needed to be placed as close as possible to the discharge location to maximize their effectiveness. Based on these requirements, it was determined that a conventional  $\mu$ -EDM machine would be insufficient in this application, necessitating the need for the development of a custom testbed design.

In order to identify the fundamental mechanics of material removal in  $\mu$ -EDM, the process needs to be examined at the single spark discharge level. The process metrics developed to determine the effectiveness of the Lorentz force technique involve analyzing the discharge craters for changes in crater characteristics, so it was essential to ensure the crater being analyzed was created by a single spark discharge to ensure accurate data was collected. Commercially available  $\mu$ -EDM circuits are not designed for single spark duty as it is not required for industrial operation. Furthermore, the discharge circuit needed to possess the ability to coordinate the production of both a single low energy discharge pulse as well as a high-speed camera trigger signal for the high-speed imaging of the spark discharge. Based on these requirements, it was determined that a custom single-spark discharge circuit would need to be designed.

### 3.2.2 Testbed Topology

The design requirements for the  $\mu$ -EDM testbed were that it had to be able to rigidly hold a 100  $\mu\text{m}$  diameter electrode wire and position it within the fixed field of view of a set of high-speed framing cameras that was to be used to collect high-speed images of the discharge process. The testbed had to rigidly hold a 15 mm square by 0.4 mm thick workpiece sample in a dielectric bath as well and accurately position and maintain an inter-electrode gap of 1  $\mu\text{m}$  between the electrode and workpiece. A minimum of one side of the testbed needed to be optically accessible to enable imaging of the process. Finally, the testbed needed to be electrically isolated from the electrode and workpiece in order to reduce the amount of stray capacitance present in the system, which can cause unwanted discharges.

Based on the design requirements, a solid model of the  $\mu$ -EDM testbed was designed in ProEngineer, as shown in Fig. 3.5. The final design of the testbed consisted of two main modules; the electrode holder with associated motion stages and the workpiece holder with

associated motion stages. The testbed was located on a precision granite surface with vibration isolation to prevent movement of the electrode during testing.

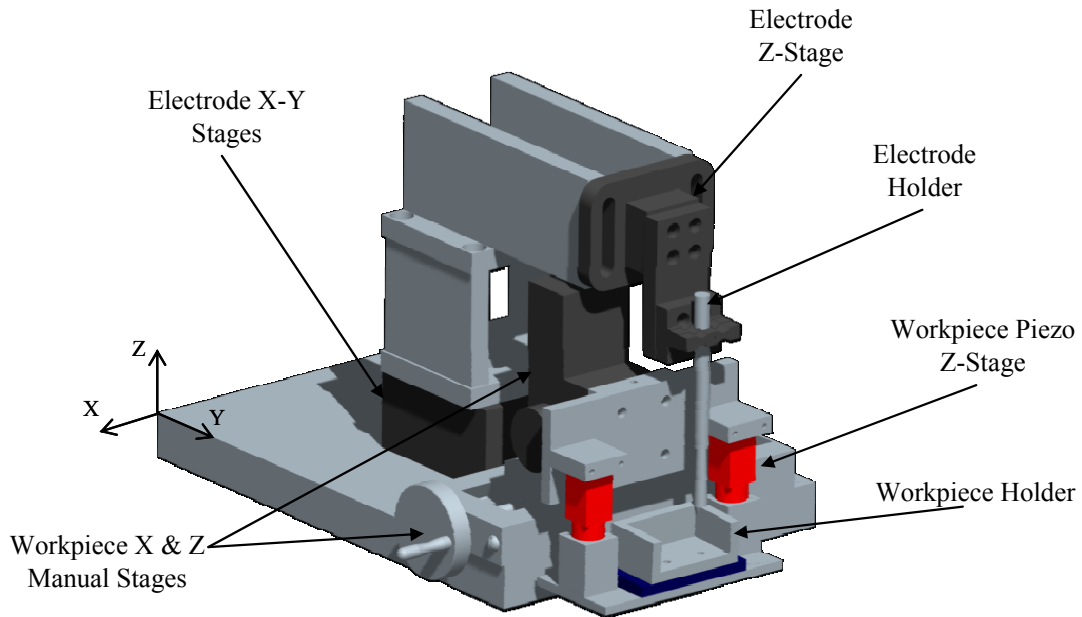


**Figure 3.5: Solid model of the  $\mu$ -EDM testbed designed for experiments in this thesis**

The small size of the 100  $\mu\text{m}$  diameter electrode caused concern for locating the tip of it within the fixed narrow and shallow field of view of the framing cameras. As a result, the electrode holder was designed to include full 3-axis manual X-Y-Z control to facilitate easy location of the electrode in the field of view. The Z-axis on the electrode holder is capable of 1  $\mu\text{m}$  positioning to locate the electrode just above the workpiece surface. Once the electrode was located within the field of view, all three axes could be locked down and any required movement during an experiment was done by moving the workpiece stages instead to avoid disturbing the focus on the electrode. The electrode holder was electrically isolated from the attached motion platforms by a plastic isolation mount, as can be seen in Fig. 3.6.

The workpiece holder was designed to accommodate a variety of workpiece and magnet mounting configurations while allowing the workpiece to be submerged in dielectric fluid and maintaining full view of the inter-electrode gap through a glass window on the side of the

workpiece holder. The workpiece holder stages included manual X-Z control, as well as a computer-controlled piezoelectric Z-stage with PID control. The assembled motion stages for both the workpiece and electrode holders can be seen in Fig. 3.6.

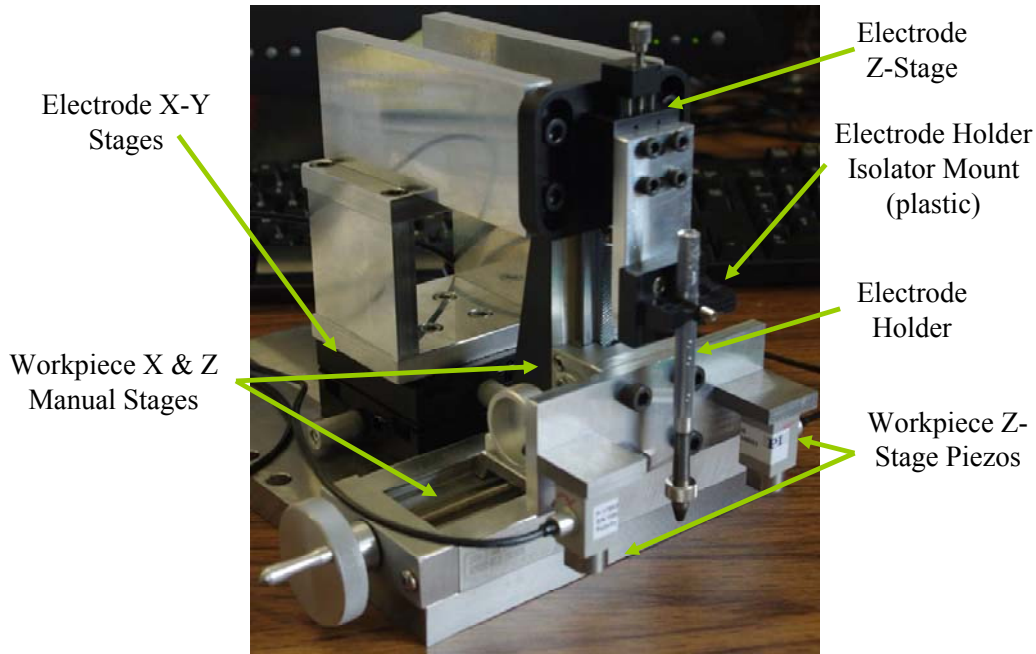


**Figure 3.6: Assembled workpiece and electrode holder stages on the  $\mu$ -EDM testbed**

The X-axis workpiece stage was used for advancing the workpiece to the next discharge location after a trial was completed, while the manual Z-axis workpiece stage was used to bring the workpiece up to the electrode after the electrode had been located in the field of view of the cameras. The piezo Z-stage was capable of 10 nm positioning and was used when setting the electrode gap prior to running a trial. The workpiece holder was also electrically isolated from the motion platforms by a plastic isolation mount.

### 3.2.3 Actuation and Control

All of the stages except for the Z-axis workpiece and electrode stages are manual screw-driven dovetail stages that can be locked into place for stability. These stages were used for rough alignment of the discharge area into the field of view of the optics used for both the

spectroscopy and high-speed camera imaging. The Z-axis electrode stages consisted of a manual screw-driven ball bearing stage with a 250  $\mu\text{m}/\text{revolution}$  screw to facilitate electrode positioning within a few microns of the workpiece surface. This stage was required to bridge the gap between the manual Z-axis on the workpiece stage, which lacked the required precision to bring the electrode within several microns of the workpiece, and the PID controlled piezo Z-axis on the workpiece stage, which only had a travel range of several microns.

The PID controlled piezo-driven Z-axis on the workpiece stage consisted of dual PI (Physik Instrumente) piezo actuators as seen in Fig. 3.6, with a Lion precision capacitance probe for feedback. The piezo actuators had a range of 20  $\mu\text{m}$  with an open loop resolution of 0.4 nm and the capacitance probe had a 25  $\mu\text{m}$  range with a 1.5 nm RMS resolution. PID control was provided by a custom LabView software program paired with a National Instruments DAQ card to handle I/O operation on the capacitance probe driver and piezo controller with a 1kHz update rate. The step input response for a 100nm step, which was the step size used when setting the electrode gap distance during experiments, is shown in Fig. 3.7. The signal noise is 10 nm and the settling time is 0.16 s, which was sufficient for our single-spark discharge experiments.

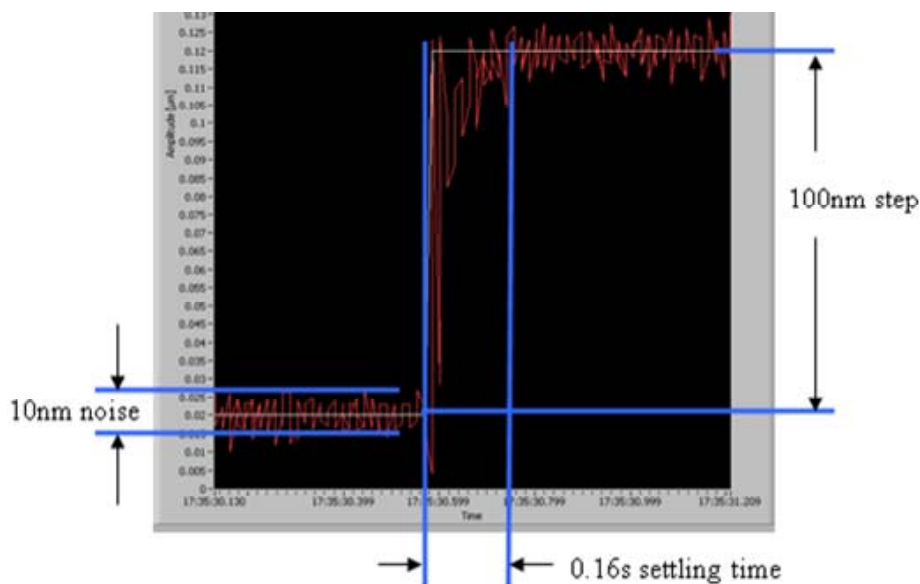


**Figure 3.7: Workpiece stage step response to a 100 nm input step**

### 3.2.4 Single Spark Discharge Circuit Design

The first design requirement for the discharge circuit was that it had to be able to coordinate a single discharge pulse with a high-speed camera trigger signal to ensure successful high-speed imaging. The second design requirement was that the discharge circuit had to prevent any unintended discharges from occurring before the triggered discharge, as the workpiece surface would be analyzed for changes in material removal characteristics so it was essential to ensure the crater being analyzed was created by a single spark discharge. Finally, the pulse energy had to be kept low enough to remain in the range suitable for  $\mu$ -EDM.

Transistor-based circuits appeared to solve the first two design requirements by being able to electronically control the pulse timing, while RC circuits are more favorable for providing low discharge energies. As a result, a hybrid RC-transistor circuit was designed and fabricated that prevented unwanted stray discharges when waiting to conduct a trial, but with the push of a button triggered a single short duration low-energy pulse discharge in addition to the trigger signal for the high speed cameras.

Figure 3.8 shows the schematic of the circuit designed for single-shot spark generation. The unique feature of this circuit is the single spark control of a capacitor discharge through a metal oxide semiconductor field effect transistor (MOSFET's) [116]. On the high-voltage side of the circuit, pulse energy is provided by a bank of five 220nF capacitors wired in parallel, for a total capacitance of 1.1 $\mu$ F. This configuration was chosen because multiple capacitors in parallel can provide current more rapidly than a single large capacitor, which was important with pulse on-times in the range of 1-2  $\mu$ s. The capacitance value was chosen because it stored enough energy to provide nearly uniform discharge current over the entire discharge duration, which is determined by the MOSFET timing.

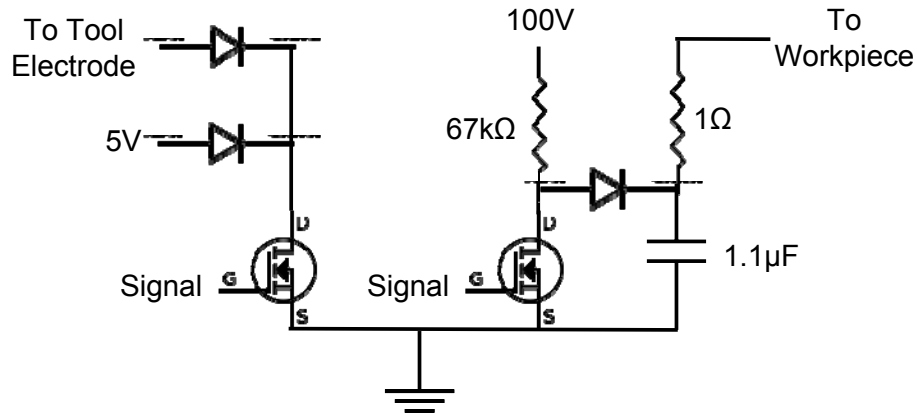


**Figure 3.8: Hybrid RC-transistor single-shot spark generator schematic**

As can be seen in Fig. 3.8, capacitor charging is accomplished by a 100V source. The voltage source is also connected to an n-channel 10A, 100V MOSFET that when opened, dumps the voltage source current to ground through a 67 kΩ resistor so that the capacitor bank is the only source of current during the discharge. The 67 kΩ resistor was chosen to prevent excessive current in the system during this period of the discharge cycle. A diode prevents the capacitor bank from connecting to ground when the MOSFET opens, keeping the capacitors charged until dielectric breakdown is initiated. A 1-ohm resistor is put in series between the capacitor bank and workpiece to allow for indirect current measurements by monitoring voltage across the resistor. This method of current measurement eliminates the issues involved with inductance-based current probes such as delayed response and low-amperage current detection.

On the grounded side of the circuit, the tool electrode is directly connected to another n-channel 10A, 100V MOSFET, which is tied into the same signal source as the MOSFET on the high-voltage side of the circuit. This allows the electrode to be opened to ground only during a discharge event, providing pulse on-time control via the MOSFET control signal. The 5V source connected in parallel with the tool electrode is used to maintain the required source-drain voltage on the MOSFET. Both MOSFET's are tied to the same gate signal, which is provided by a

monostable multivibrator, commonly referred to as a “one-shot,” that can provide a 5V square wave input with infinitely adjustable pulse width for pulse duration control.

The sequence of events for a single-shot discharge is as follows. Prior to discharge, the capacitor bank is charged to 100V. Both workpiece and tool electrode are held at approximately 100V since the tool electrode is essentially left “floating” since the MOSFET is not allowing connection to ground at this point. This system prevents stray capacitance in the circuit from causing small discharges while waiting for the signal to be the discharge event. Once a manual button is pressed to initiate the discharge, the “one-shot” sends a signal to both MOSFET’s to open their source to drain connections. Also initiated by this same button press is a second “one-shot” that controls the high-speed camera trigger signal. The MOSFET connected to the 100V side opens to ground, causing all current from the 100V source to drain through the 67k $\Omega$  resistor to ground. The MOSFET connected to the tool electrode side opens to ground as well, pulling the tool electrode voltage down to 0V, creating the spark gap voltage differential required for dielectric breakdown. Once breakdown voltage is achieved, the capacitors discharge through the plasma channel formed in the electrode gap until the signal from the “one-shot” ceases, ending the discharge event by cutting off connection to ground for the tool electrode. Diodes are placed throughout the circuit to prevent backflow of current and maintain voltage potentials where needed.

### 3.3 Experimental Results for Magnetic Field Effects on Plasma Characteristics in $\mu$ -EDM

An experiment was conducted to gain initial insight into the possibility of using perpendicular magnetic fields to affect plasma confinement and/or plasma stability for the

purpose of improving MRR in non-magnetic materials as was discussed in Section 2.4.5.

Perpendicular magnetic fields are defined in this thesis as fields with field lines perpendicular to the workpiece surface and parallel to the electric field lines as shown in Fig. 3.9. The effects of the magnetic field on the plasma were quantified by measuring the discharge crater area from SEM images of the craters. The area data was examined for changes in average and standard deviation. Decreases in the average discharge crater area would indicate plasma confinement, thereby affecting a smaller area of the workpiece surface. Decreases in the standard deviation of the discharge crater area would indicate enhanced plasma stability, thereby increasing plasma channel uniformity from one discharge to the next. Visual confirmation of characteristic changes was provided by time-resolved high-speed images of the discharge plasma as it evolved.

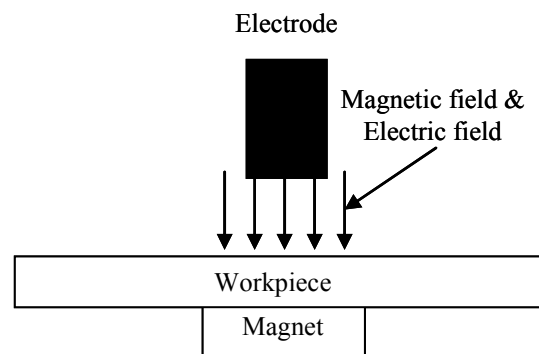


**Figure 3.9: Definition of perpendicular magnetic field orientation**

### 3.3.1 Design of Experiments

Trials were run using a magnetic field supplied by a 0.7T surface field strength permanent magnet. Magnetic field lines in the discharge gap can be assumed to be perpendicular to the magnet face due to the close proximity of the discharge location to the center of the magnet face. Test conditions for the permanent magnet trials are shown in Table 3.1.

**Table 3.1: Experimental conditions for permanent magnet tests**

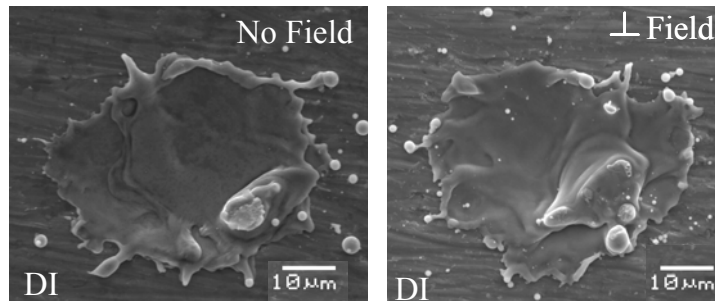
Electrode (Anode)	100 $\mu$ m diameter W wire
Workpiece (Cathode)	Grade 5 titanium (6% Al, 90% Ti, 4% V)
Gap Distance	1 $\mu$ m
Open gap voltage	100V
Discharge Power	50-210W
Dielectric	Deionized Water
Magnet	Grade 53 Neodymium (0.7T surface field strength)

For each trial, the workpiece was prepared by polishing and cleaning. To simulate in-process electrode condition, the electrode, which is left with a chisel edge after installation, was prepared by conducting a series of discharges against a sacrificial titanium workpiece before beginning testing. This blunts the chisel edge and results in a tool electrode surface characteristic of one seen in-process. Once the workpiece was mounted to the stage, the stage was filled with dielectric fluid and brought into close proximity with the electrode. To locate the surface of the workpiece with respect to the tool electrode, the piezo-actuated stages were oscillated upwards and downwards while monitoring the oscilloscope reading of the gap voltage under zero current conditions. Once the point of contact was determined to within 50nm, the gap was set to 1 $\mu$ m and a discharge was initiated. After the discharge, a step-over of 640 $\mu$ m was used to separate subsequent discharge locations. The electrode was re-zeroed at each individual discharge location to ensure accurate gap setting.

### 3.3.2 Perpendicular Magnetic Field Results

**Discharge crater area analysis.** A simple set of metrics was used in the initial permanent magnet tests to determine the viability of perpendicular magnetic fields for confining and/or stabilizing the  $\mu$ -EDM discharge plasma. High resolution images of the discharge craters were

taken on a JEOL 6060LV SEM, as shown in Fig. 3.10, and the discharge crater areas were analyzed by tracing the outline of the discharge and calculating the enclosed area using image processing software. The observation of smaller crater areas would point to plasma confinement, and a reduction in the area standard deviation would point to enhanced plasma stability.



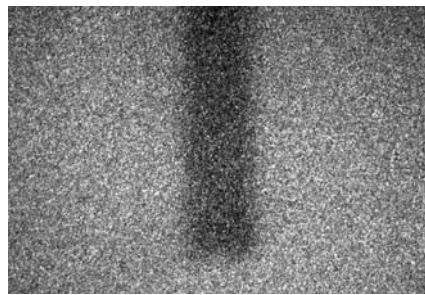
**Figure 3.10: Comparison of SEM images between a normal  $\mu$ -EDM discharge and a  $\mu$ -EDM discharge in the presence of a perpendicular magnetic field**

Table 3.2 summarizes the results of these preliminary experiments. It can be seen that the average discharge crater area does appear to be slightly smaller in the case of the perpendicular magnetic field tests, as well as the standard deviation being less than half the deviation of the standard no-field  $\mu$ -EDM discharge craters. To compare the difference of means for this sample set with unknown but equal variance, a t-test was used. At a 0.1 level of significance, the test statistic is  $t_{\text{calc}}=1.73$ , with a rejection criteria of equal true means being  $t_{\text{crit}}=1.86$ , thus statistically there is no evidence to suggest a difference of true means at a 0.1 level of significance. To compare the difference of standard deviations for this sample set assuming a standard distribution of the data, an F-test was used. At a 0.1 level of significance, the test statistic is  $F_{\text{calc}}=4.324$  with a rejection criteria of equal true variances of  $F_{\text{crit}}=4.11$ , thus there is evidence to suggest a decrease in the discharge crater area standard deviation with the addition of the perpendicular magnetic field.

**Table 3.2: Perpendicular magnetic field discharge crater area comparison**

Trial	Perpendicular Magnetic Field			No Magnetic Field		
	Discharge Energy [ $\mu\text{J}$ ]	Pulse Duration [ $\mu\text{s}$ ]	Area [ $\mu\text{m}^2$ ]	Discharge Energy [ $\mu\text{J}$ ]	Pulse Duration [ $\mu\text{s}$ ]	Area [ $\mu\text{m}^2$ ]
1	175.7	2.1	2011	181.2	2.1	2108
2	211.4	2.4	2349	207.9	2.3	2674
3	207.2	2.4	2318	207.9	2.3	2674
4	199.7	2.1	2069	201	2	2092
5	197.5	2.4	2129	207.9	2.3	2674
Average	<b>198.3</b>	<b>2.3</b>	<b>2175</b>	<b>201.2</b>	<b>2.2</b>	<b>2444</b>
Standard Deviation	<b>13.8</b>	<b>0.2</b>	<b>151</b>	<b>11.6</b>	<b>0.1</b>	<b>314</b>

**High speed imaging.** Based on the previous plasma confinement and stability research discussed in Section 2.4, it was determined that optical observation of the  $\mu$ -EDM discharge plasma may help reveal changes in plasma discharge size, indicating possible confinement, or an improvement in discharge plasma uniformity, indicating enhanced plasma stability. As a result, high-speed imaging data was collected for a number of trials utilizing a combination of two High Speed Framing Cameras (HSFC Pro) from the Cooke Corporation with a combined capability of seven million frame-per-second. Each image collected during a discharge was able to be spaced 140ns apart, yielding approximately ten images per discharge. Figure 3.11 shows an example of what the 100  $\mu\text{m}$  diameter electrode after focusing through a 20x Mitutoyo long working distance objective and Fig. 3.12 shows an example of the captured image progression.



**Figure 3.11: Example of the 100  $\mu\text{m}$  tool electrode in focus through a 20x objective lens prior to a discharge**

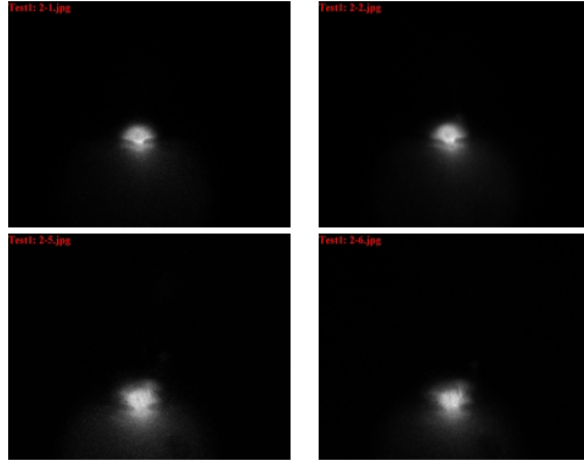


**Figure 3.12: Example progression of high-speed images collected during a spark discharge**

The gray-scale images output by the camera were processed using a custom image thresholding algorithm to isolate the area of the image containing the plasma. Once this area was identified, the image was colorized based on intensity value, with blue corresponding to low light intensity from the plasma and red corresponding to high light intensity from the plasma. This was useful in visually determining both the center of the plasma and the expansion of the plasma. Using the electrode image collected during focusing (Fig. 3.11), the colorized plasma images were overlaid onto the electrode image to provide a size scale reference, as shown in Fig. 3.13.

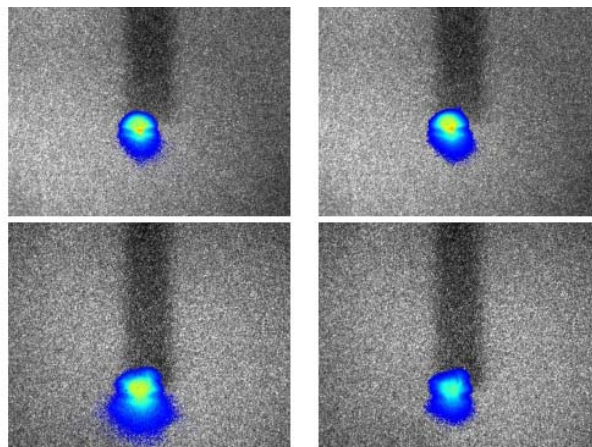


**Figure 3.13: Example of discharge plasma high-speed images after processing**

An immediate observation about this data is that the light output from the plasma has been distorted by diffusion through the dielectric fluid, as the plasma can be observed to expand into the electrode, which is physically impossible. For comparison, Fig. 3.14 shows similar discharge data in air, not dielectric fluid. The plasma can clearly be seen to be much smaller and well confined by the boundaries of the electrode.

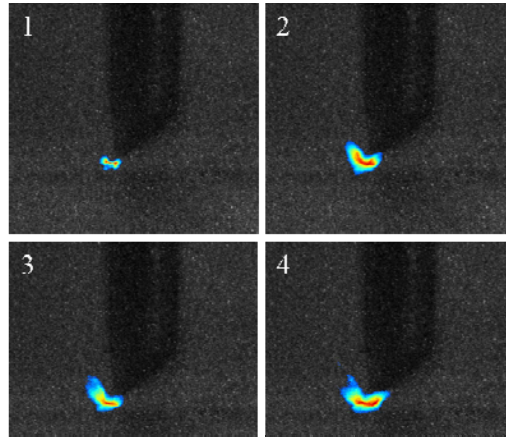


**Figure 3.14: Example of high-speed imaging of a  $\mu$ -EDM discharge in air**

The formation of bubbles in the gap prior to a discharge as the result of electrolysis of the deionized water also causes problems with high-speed imaging as they obstruct the view of the discharge plasma. As a result, only one set of clear high-speed images for each trial was able to be collected after numerous repetitions. Figure 3.15 shows the processed high-speed image progression of a normal  $\mu$ -EDM discharge without any external magnetic fields applied, and Figure 3.16 shows images from a  $\mu$ -EDM discharge in the presence of a perpendicular magnetic field. Figure 3.16 suffers from another issue associated with the high-speed imaging process in that when processed, sometimes the electrode image does not align with the plasma image because they are taken at separate times. Regardless, there is no significant difference observable between these two sets of high-speed images.

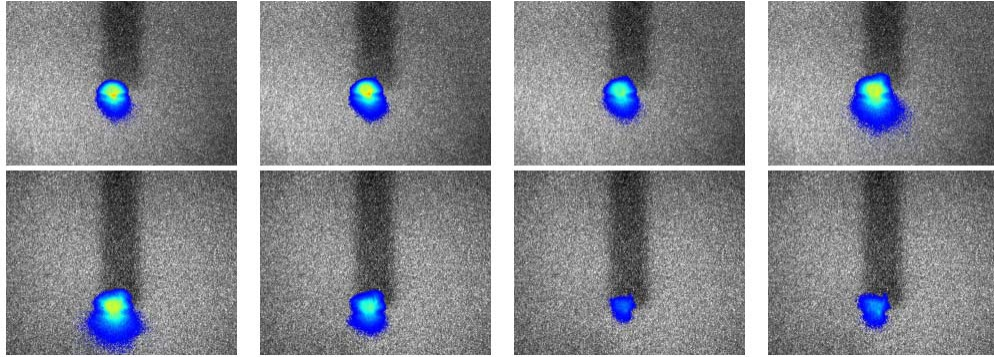


**Figure 3.15: High-speed images from a normal  $\mu$ -EDM discharge**

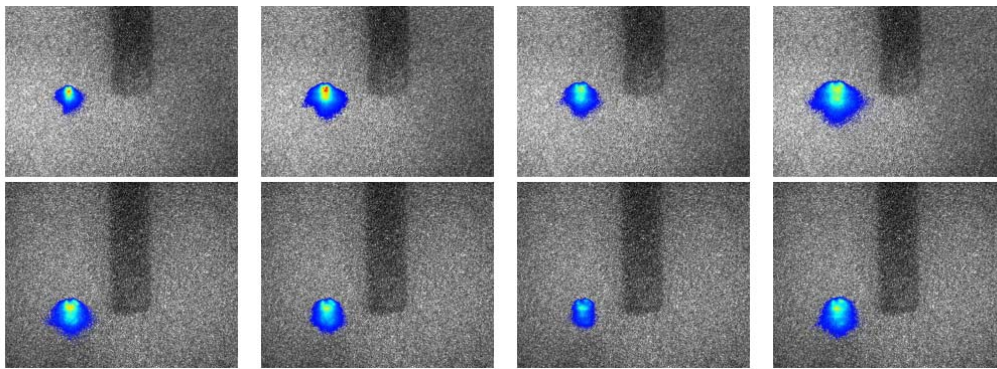


**Figure 3.16: High-speed images from a  $\mu$ -EDM discharge in the presence of a perpendicular magnetic field**

**Summary.** The evidence from the average discharge crater area comparison shows little support for the magnetic fields having an effect on discharge plasma confinement, but the differences seen in the standard deviations may suggest changes in plasma stability. Because of the many issues associated with the high-speed imaging technique, no conclusions on the magnetic field plasma confinement/stabilization technique could be made from this data, so further testing was later pursued utilizing spectroscopic characterization techniques during the electromagnet experiments that will be discussed in Chapter 4.

## 3.4 Experimental Results for Magnetic Field-Assisted $\mu$ -EDM using Lorentz Forces

### 3.4.1 Design of Lorentz Force Experiments

Three experiments were conducted to gain initial insight into the effects of Lorentz forces on discharge crater characteristics with an eye towards enhancing MRR in the  $\mu$ -EDM of non-magnetic materials through the use of magnetic fields. The Lorentz force technique utilizes a parallel magnetic field orientation, indicating the magnetic field lines are parallel to the workpiece surface and perpendicular to the electric field lines as shown in Fig. 3.17.

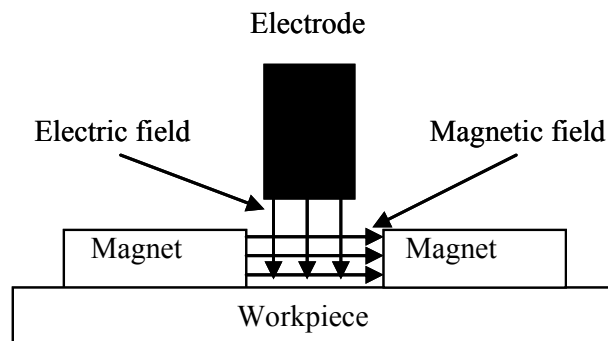


**Figure 3.17: Definition of parallel magnetic field orientation**

The Lorentz force process was tested in three configurations: one where the Lorentz force was parallel to the workpiece surface as the result of no directional workpiece current, as shown in Fig. 3.2, one where the Lorentz force resulting from the directional current in the workpiece was pointing out from the workpiece surface, thus creating a tension force on the melt pool, and one where the Lorentz force was pointing into the workpiece surface, creating a compression force on the melt pool as shown in Fig. 3.3. The effects of the Lorentz force on the discharge crater characteristics were measured by obtaining 3D surface scans of the discharge crater and analyzing the volume of the crater. Changes in the crater volumes would provide evidence to

support claims that the Lorentz forces alter the material removal mechanism in  $\mu$ -EDM. The only change to the design of experiment reported in Section 3.3.1 is the direction of the magnetic field in these experiments.

### 3.4.2 Lorentz Force without Directional Workpiece Current Results

When implementing the Lorentz force process *with* directional workpiece current, two Lorentz forces are predicted, one parallel to the workpiece surface and the other perpendicular as discussed in Section 3.1. The parallel force vector is present irrespective of directional workpiece current. In order to decouple the Lorentz force effects seen in the discharge crater volumes between those originating from the directional workpiece current from those preexisting from the plasma channel current, the Lorentz force process was first investigated *without* the directional workpiece current to examine the effect of the force vector that is parallel to the workpiece surface.

To enable volume data to be collected, 3D imaging of the discharge crater was conducted by laser scanning. The Z-axis of a 3-axis micro-scale machine tool (MMT) was fitted with a Keyence LT-9010M surface scanning confocal laser with  $0.01\mu\text{m}$  distance resolution and a  $2\mu\text{m}$  spot size, while the  $\mu$ -EDM workpiece was affixed to the XY-axis of the MMR to enable raster scanning of the surface.

The laser scans over the surface collecting discrete height measurements from the  $2\mu\text{m}$  diameter laser spot with a spacing of  $2\mu\text{m}$  (SEM image in Fig. 3.18), thus each discrete data point is actually an average height over the  $2\mu\text{m}$  spot size of the laser with no overlap. This discrete point data from the laser is then digitally approximated as rectangles with a square base of  $2\mu\text{m} \times 2\mu\text{m}$  and height 'h' for volume calculations (Fig. 3.18). The surface topology can be

digitally recreated by plotting the height data for every point in a matrix with  $2\mu\text{m}$  spacing between points, as seen in Fig. 3.19.

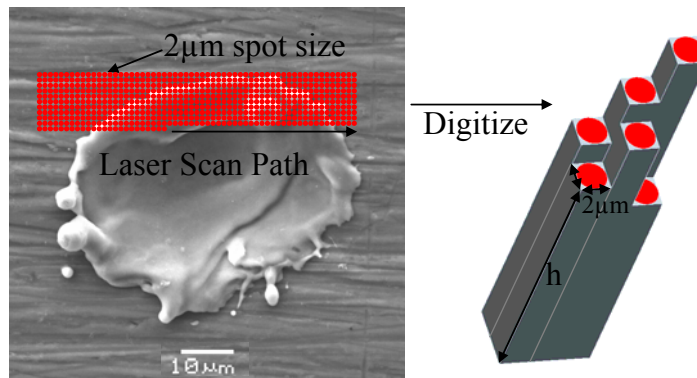


**Figure 3.18: Digitizing the discharge crater surface (SEM spot sizes to scale)**

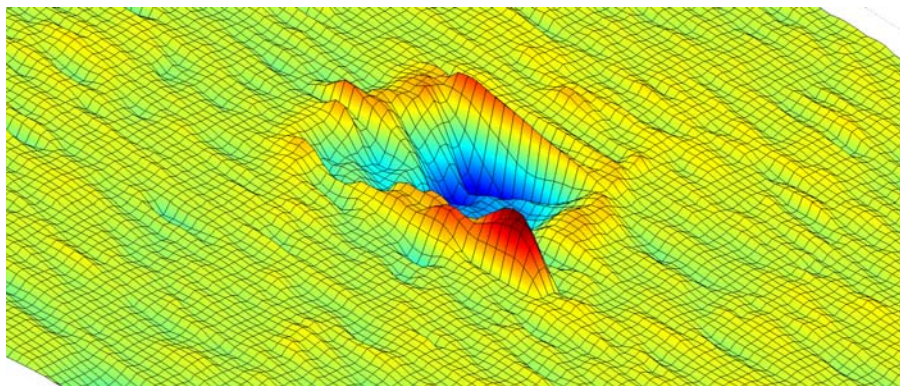


**Figure 3.19: 3D surface topography from laser scan**

After initial examination of the discharge craters, two unique volumes were identified, a negative volume, defined as the material pushed up around the rim of the discharge crater above the workpiece surface, and positive volume, defined as the material removed below the surface of the workpiece (Fig. 3.20). The erosion volume  $v_e$  (actual amount of material removed) was found by taking the difference in these two volumes. Surface roughness was not insignificant at the micro-scale, so the workpiece surface was characterized by examining the area surrounding

the discharge crater to allow for differentiation in the 3D laser data between depth data from the discharge crater and depth data from the surface roughness.

To calculate volume, the following algorithm was used:

1. Digitally correct any slope to the workpiece surface and move the average surface height to  $z=0\mu\text{m}$ ;
2. Determine the maximum depth and height of the surface roughness on the workpiece surface around the discharge crater to minimize inclusion of surface roughness in volume measurements;
3. Any points in the discharge crater found to be higher than the highest point of the workpiece surface were added to the total negative volume (Fig. 3.20);
4. Any points in the discharge crater found to be lower than the lowest point on the workpiece surface were added to the total positive volume (Fig. 3.20).

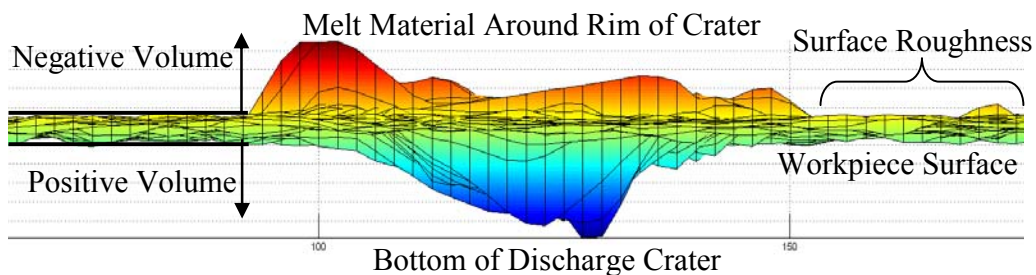


**Figure 3.20: Side view of 3D surface map**

A number of trials were conducted both with and without the parallel magnetic field present at the workpiece surface without promoting any directionality in the current flowing through the workpiece. After the discharge craters were created, they were scanned using the laser and their volumes were analyzed. Table 3.3 shows the positive and negative volume data for the parallel magnetic field experiments without directional workpiece current versus the no-field

experiments. The average positive volume for the no-field case was  $3156 \mu\text{m}^3$ , with an increase of 8.5% to  $3424 \mu\text{m}^3$  for the parallel field case. The average negative volume for the parallel field case was  $719 \mu\text{m}^3$ , a 10.6% decrease from the no-field case at  $804 \mu\text{m}^3$ . Both changes in volume are small between the no-field and parallel field cases, indicating that the melt pool is largely unaffected by the application of a parallel magnetic field alone.

**Table 3.3: Comparison of No Field and Parallel Field volume data**

Trial	No Field		Parallel Field	
	Positive Volume [ $\mu\text{m}^3$ ]	Negative Volume [ $\mu\text{m}^3$ ]	Positive Volume [ $\mu\text{m}^3$ ]	Negative Volume [ $\mu\text{m}^3$ ]
1	2910	371	3300	240
2	2720	389	4640	334
3	3060	1230	2070	720
4	2070	513	2700	451
5	3440	742	1490	51
6	1980	226	4680	220
7	2940	1690	4620	404
8	4070	419	4530	193
9	3980	1630	3210	1930
10	4390	834	3000	2650
Average	<b>3156</b>	<b>804</b>	<b>3424</b>	<b>719</b>
Standard Deviation	<b>816</b>	<b>535</b>	<b>1157</b>	<b>864</b>

A t-test was conducted to verify that there is no evidence to suggest a difference of true means in either the negative or positive volume at a level of significance of 0.1. The test statistic for the positive volume was  $t_{\text{calc}}=0.599$  and for the negative volume was  $t_{\text{calc}}=0.265$  with a rejection criteria of equal true means of  $t_{\text{crit}}=1.734$ , thus there is no evidence to suggest a difference of true means in either the positive volume data or the negative volume data at a level of significance of 0.1. This is likely the result of the current losing directionality too rapidly in the workpiece, negating the effects of the Lorentz force.

Further examination of SEM and 3D laser images in Fig. 3.21 shows no significant differences in the discharge crater characteristics between the two cases. This evidence, in combination with the crater volume data, indicates that the parallel Lorentz force vector has no effect on the discharge crater volumes and that any changes observed with the application of the directional workpiece current would be due to the perpendicular force vector.

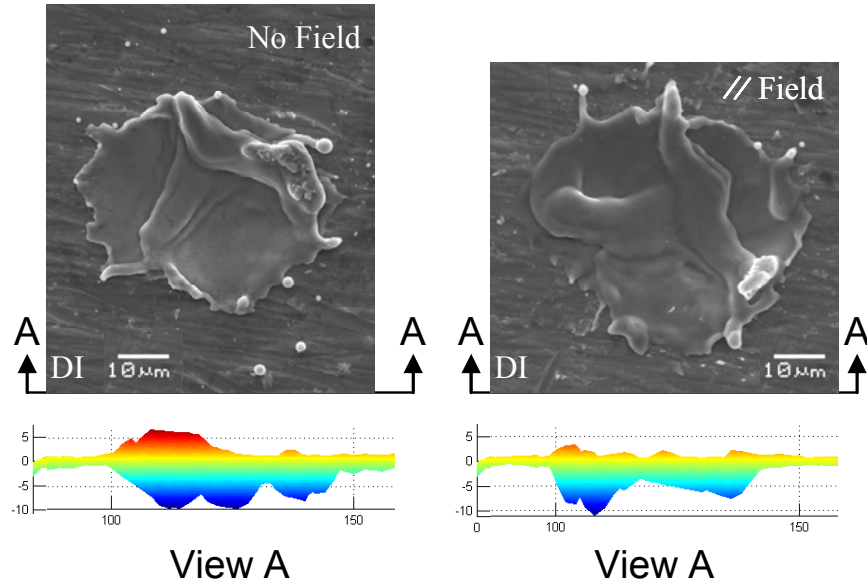


**Figure 3.21: SEM and laser scan image comparison between parallel field and no field experiments**

### 3.4.3 Lorentz Force Pointing into Workpiece Surface Results

Based on the proposed Lorentz force-assisted process from Section 3.1, it was determined that measuring erosion efficiency in addition to discharge crater volume would be important for determining the effect the Lorentz force vector originating from the directional workpiece current had on the MRR of the process. Erosion efficiency can be used to quantify the percentage of discharge energy going into material removal. The greater the erosion efficiency, the higher the volume of material removed per unit energy expended during a discharge, and thus

the higher MRR achieved. Erosion efficiency, originally defined by Wang et. al. [57], is the ratio of erosion energy to spark energy:

$$\eta = \frac{E_e}{E_s} = \frac{v_e \rho H_m}{E_s} \quad (3.1)$$

where  $E_s$  is the spark energy and  $E_e$  is the erosion energy.

Erosion energy  $E_e$  as defined by Wang et. al. [57] is a relative energy quantity representative of the amount of material actually removed from the melt pool, assuming melting/splashing as the primary material removal mechanism. This is not the same as the energy required to remove that material, which would take into account ejection velocity, surface tension forces, etc. By the definition provided by Wang et al.,  $E_e$  can be found by the product seen in Eq. 3.1 where  $v_e$  is the erosion volume,  $\rho$  is the density of the material, and  $H_m$  is the enthalpy of melting for the workpiece material. The titanium workpiece properties used to calculate  $E_e$  are listed in Table 3.4.

**Table 3.4: Titanium Workpiece Properties**

Density	4.43 g/cm <sup>3</sup>
Melting Point	1933 K
Boiling Point	3560 K
Enthalpy of Melting	1.156x10 <sup>3</sup> kJ/kg

Spark energy  $E_s$  was calculated using discharge voltage, current and duration data:

$$E_s = VIT \quad (3.2)$$

where  $V$  is voltage across the electrode gap,  $I$  is the current through the electrode gap, and  $T$  is the duration of the discharge. To measure these quantities during experimentation, a Tektronix TDS2024B oscilloscope, capable of two giga-samples per second, was utilized to record discharge waveform data. To measure the gap voltage, two voltage probes were utilized; one affixed to the workpiece, and the other to the electrode, and their difference was taken as the gap

voltage. Discharge current was measured indirectly by inserting a 1.0-ohm resistor inline with the discharge circuit and measuring the voltage drop across the resistor during the discharge pulse. Using Ohm's law  $I=V/R$ , the discharge current was easily calculated once the voltage drop across the resistor was known. Pulse duration was measured using the time scale on the oscilloscope and taking the difference between the pulse start time and pulse end time. To calculate  $E_s$ , numerical integration was used over the duration of the discharge since both voltage and current vary with time over the discharge duration, as seen below in Fig. 3.22 and previously shown in Fig. 3.4.

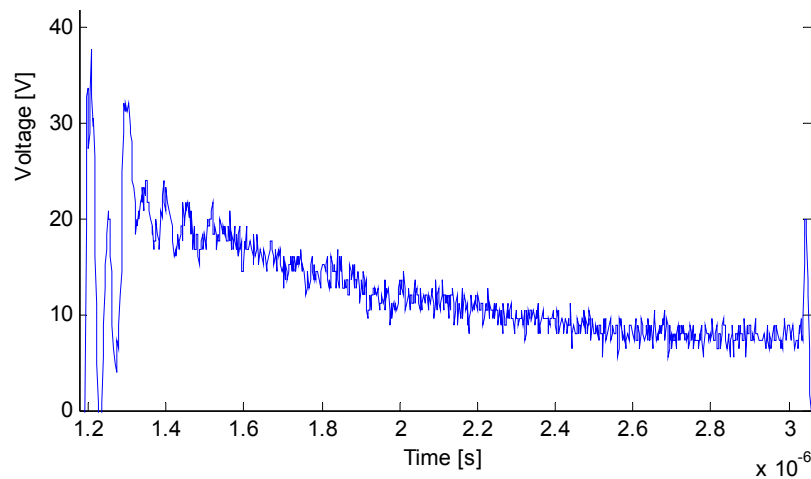


**Figure 3.22: Example of discharge gap voltage waveform during a  $\mu$ -EDM discharge**

Trials were conducted using both the standard  $\mu$ -EDM process as well as the Lorentz force pointing into the workpiece surface process and the erosion efficiency and crater volume were analyzed for differences between the cases. Table 3.5 shows the results from these experiments. With the Lorentz force pointing into the melt pool, there is an increase in positive volume of 30.5% and an increase in negative volume of 11% when compared to the no field case, resulting in an increase in erosion volume of 38.2%. Average erosion efficiency for the no-field case was 4.5%, with an increase of 25% in the Lorentz force into the workpiece surface case to 5.6%.

**Table 3.5: Comparison of No Field and Lorentz Force into the workpiece experiments**

Trial	<u>No Field</u>				<u>“Lorentz In”</u>			
	Positive Volume [ $\mu\text{m}^3$ ]	Negative Volume [ $\mu\text{m}^3$ ]	Erosion Volume [ $\mu\text{m}^3$ ]	Erosion Efficiency [%]	Positive Volume [ $\mu\text{m}^3$ ]	Negative Volume [ $\mu\text{m}^3$ ]	Erosion Volume [ $\mu\text{m}^3$ ]	Erosion Efficiency [%]
1	3060	1230	1830	4.4%	2030	548	1482	4.4%
2	2070	513	1557	3.8%	3350	1360	1990	5.0%
3	3440	742	2698	6.9%	4440	323	4117	6.6%
4	1980	226	1754	4.8%	5420	1220	4200	7.5%
5	2940	1690	1250	2.1%	4120	796	3324	5.3%
6	4070	419	3651	5.2%	4590	838	3752	6.0%
7	3980	1630	2350	3.6%	5130	1300	3830	5.9%
8	4390	834	3556	5.3%	4760	1720	3040	4.3%
Average	<b>3241</b>	<b>911</b>	<b>2331</b>	<b>4.5%</b>	<b>4230</b>	<b>1013</b>	<b>3217</b>	<b>5.6%</b>

A t-test on the difference of means for a sample set with unknown but equal variance was used on the erosion efficiency data to test the confidence of these results. Erosion efficiency data was chosen because it is normalized to power, eliminating the effect varying power has on the melt pool characteristics. The test statistic value was  $t_{\text{calc}}=1.769$  with a rejection criteria of equal true means of  $t_{\text{crit}}=1.761$  at a level of significance of 0.1, which indicates that there is mild evidence to suggest that the erosion efficiency is increased in the “Lorentz In” experiments versus the No Field experiments at a level of significance of 0.1.

Figure 3.23 shows a comparison of SEM images between the no field and Lorentz force into the workpiece cases. The images for the Lorentz force into the workpiece exhibit increased consistency from crater to crater in both shape and uniformity of distribution of melt material in the rim versus the no-field images. Additionally, the depth of the crater is greater in the majority of the Lorentz force into the workpiece cases than in the no-field cases. These results show strong evidence that the addition of the Lorentz force pointing into the workpiece surface alters the mechanism of material removal and can enhance the erosion efficiency of the  $\mu$ -EDM process in non-magnetic materials through the use of magnetic fields.

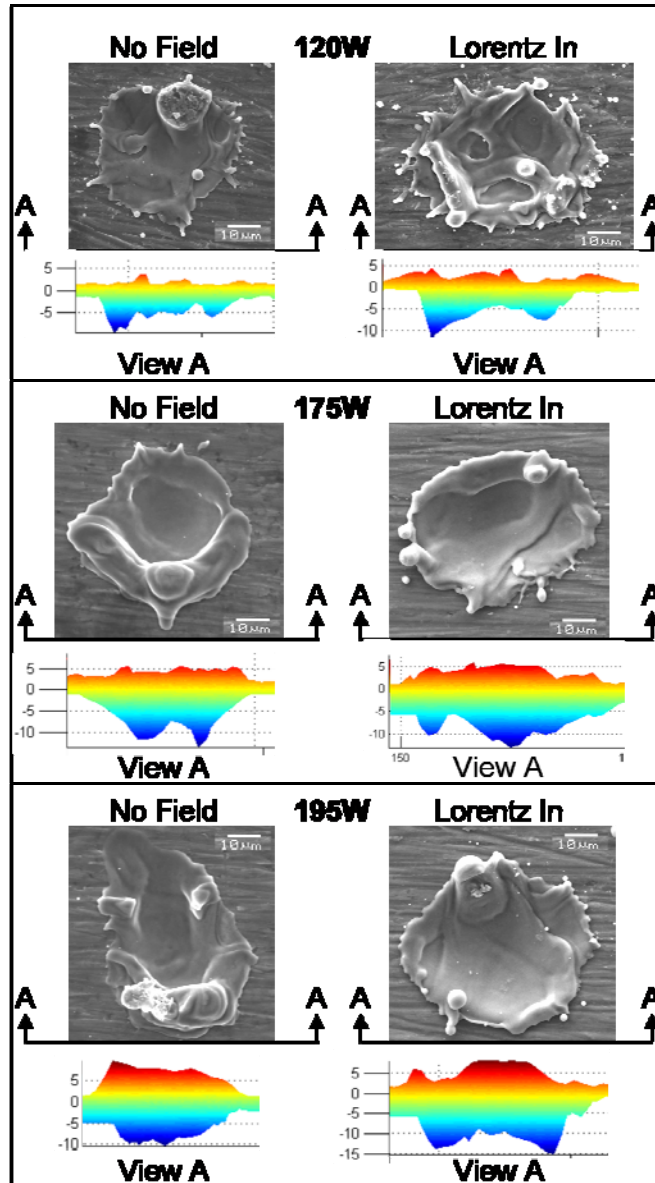


**Figure 3.23: SEM and laser scan image comparison between three power levels for Lorentz force into workpiece surface and no field experiments**

### 3.4.4 Lorentz Force Pointing Outward From Workpiece Surface Results

Table 3.6 shows a comparison of results from the no field experiments and the Lorentz force pointing out from the workpiece surface experiments. The average negative volume decreases by 43% and the average positive volume decreases by 23% for the Lorentz force pointing out

from the workpiece case compared to the no-field case. The result is a 15% decrease in erosion volume and the erosion efficiency appears unaffected.

**Table 3.6: Comparison of No Field and Lorentz Force out from the workpiece experiments**

Trial	<u>No Field</u>				<u>“Lorentz Out”</u>			
	Positive Volume [ $\mu\text{m}^3$ ]	Negative Volume [ $\mu\text{m}^3$ ]	Erosion Volume [ $\mu\text{m}^3$ ]	Erosion Efficiency [%]	Positive Volume [ $\mu\text{m}^3$ ]	Negative Volume [ $\mu\text{m}^3$ ]	Erosion Volume [ $\mu\text{m}^3$ ]	Erosion Efficiency [%]
1	3060	1230	1830	4.4%	751	61	690	3.2%
2	2070	513	1557	3.8%	1532	117	1415	3.7%
3	3440	742	2698	6.9%	3760	172	3588	8.4%
4	1980	226	1754	4.8%	2320	329	1991	5.8%
5	2940	1690	1250	2.1%	2870	796	2074	5.1%
6	4070	419	3651	5.2%	2760	183	2577	6.8%
7	3980	1630	2350	3.6%	2960	1400	1560	2.3%
8	4390	834	3556	5.3%	3120	951	2169	3.7%
9	-	-	-	-	2490	639	1851	2.5%
Average	<b>3241</b>	<b>911</b>	<b>2331</b>	<b>4.5%</b>	<b>2507</b>	<b>516</b>	<b>1991</b>	<b>4.6%</b>

A visual inspection of SEM images in Fig. 3.24 does not appear to reveal differences in the discharge craters between the no-field case and Lorentz force pointing out from the workpiece surface case. Both cases show highly irregular discharge crater shapes with no clear pattern from crater to crater. The difference in the peak-to-valley distance is also similar between the no-field and Lorentz force pointing out from the workpiece cases. These results show evidence that the addition of the Lorentz force pointing out from the workpiece surface alters the flow of melt material in the discharge crater, as evidenced by the changes in positive and negative crater volumes, but it may not affect the erosion efficiency of the  $\mu$ -EDM process.

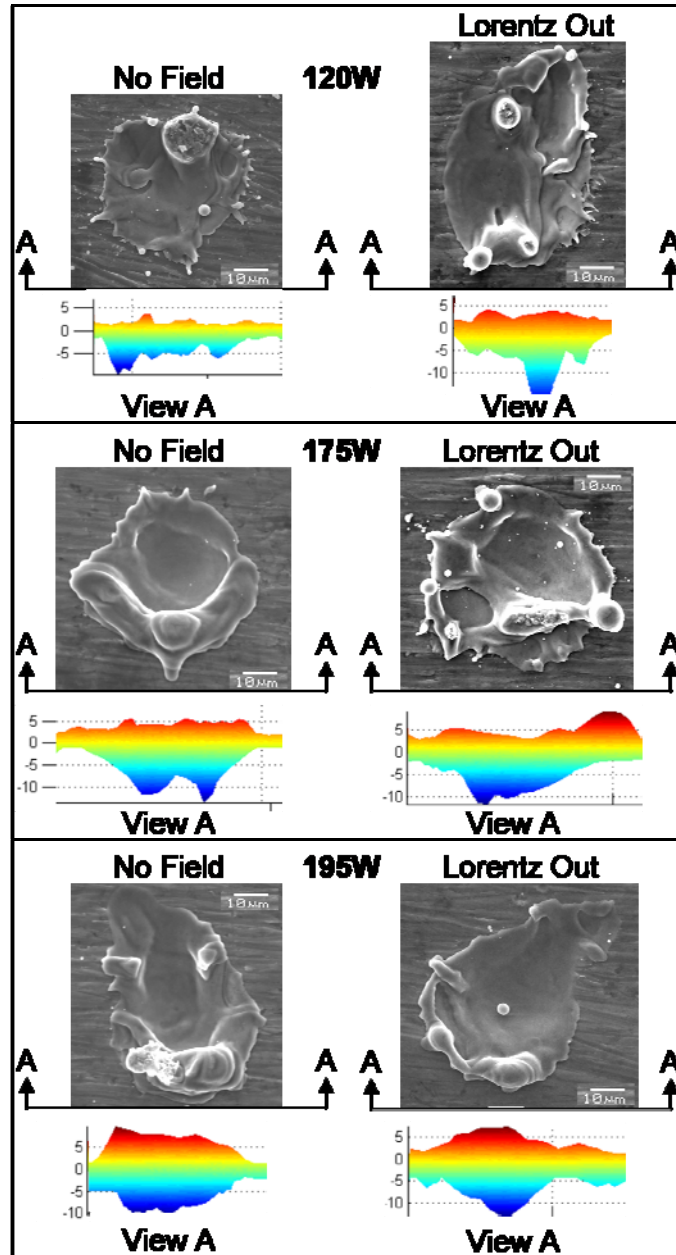


**Figure 3.24: SEM and laser scan image comparison between three power levels for Lorentz force pointing out from workpiece surface and no field experiments**

Based on the promising results in the Lorentz force pointing into the workpiece surface experiments to increase erosion efficiency using permanent magnets to alter the material removal characteristics of non-magnetic materials in  $\mu$ -EDM, these experiments were selected to be continued using electromagnets as the source of the magnetic field in the next chapter to provide

additional insight into the process. Additionally, the results from the Lorentz force pointing out from the workpiece surface experiments showing decreases in both positive and negative volume without any evidence of changes in erosion efficiency are also worth further investigation using electromagnets in the next chapter.

### 3.4.5 Tool Wear Analysis

Volumetric tool wear is often only a small percentage of the volumetric workpiece wear [12], indicating that when conducting single-spark discharge experiments, the volume of tool material removed is likely immeasurable. One alternative for determining tool wear is to examine the chemical composition of the melt pool. During a spark discharge, electrode material that is eroded can migrate to the workpiece surface and resolidify in the melt pool [117-120]. By quantifying the difference in workpiece material composition before and after a pulse discharge, an idea of the degree of electrode wear can be determined.

To measure the effects of tool wear in the single-discharge  $\mu$ -EDM experiments, the resolidified melt pool was analyzed using Oxford Instruments ISIS EDS (Energy Dispersive Spectroscopy) System to determine its composition and look for signs of electrode cross-contamination in the melt pool. In order to establish a baseline for comparison, a clean area of the workpiece well away from any discharge craters was selected first for analysis. Several measurements were taken of the surface chemistry at this location and the results were averaged together to form the baseline composition. Then, the sample was moved to a position containing one of the discharge craters created in Section 3.4 for composition analysis. Eighteen separate discharge craters were analyzed in this manner and Table 3.7 lists the averages for the chemical composition data collected.

**Table 3.7: EDS data for workpiece and melt pools**

	<b>%Al</b>	<b>%Ti</b>	<b>%V</b>	<b>%W</b>
<b>Baseline</b>	$\bar{x}$ : 4.9	$\bar{x}$ : 91.0	$\bar{x}$ : 3.9	$\bar{x}$ : 0.3
<b>Magnetic Field Discharge Craters</b>	$\bar{x}$ : 4.3	$\bar{x}$ : 90.4	$\bar{x}$ : 4.8	$\bar{x}$ : 0.5

The melt pool composition for the Lorentz force discharge craters is nearly identical to the composition of the parent workpiece material. More importantly, only trace amounts of tungsten are shown for both cases, indicating that electrode material wear is undetectable in the Lorentz force discharge craters based on the material migration principle discussed at the beginning of this section. The lack of electrode wear found here is in agreement with Wang et. al. [57], who found that there is a high correlation between melting temperature differences and erosion volume in single-spark discharge events. The titanium used in these experiments as the workpiece material has a melting point of 1933K, while the tungsten electrode melts at 5828K, thus low electrode wear can be expected.

### 3.5 Chapter Summary

The development of a Lorentz force-assisted  $\mu$ -EDM technique has been detailed and the requirements for its implementation have been used as the driving criterion for the design of a  $\mu$ -EDM testbed. The  $\mu$ -EDM testbed and hybrid RC-transistor discharge circuit required to test the magnetic field-assisted  $\mu$ -EDM techniques have been designed and built. Preliminary testing on these components has been completed to determine their capabilities.

The use of perpendicular magnetic fields during  $\mu$ -EDM appears to have little effect on the discharge crater area; however, the variation in the areas does appear to decrease in the presence of perpendicular magnetic fields, possibly indicating enhanced plasma stabilization. High-speed imaging of the plasma channel during these discharges was attempted to support these initial

findings. However, no definitive results were produced due to diffusion of the light from the discharge plasma and formation of bubbles in the discharge gap from the electrolysis of the dielectric which caused sufficient degradation of the optical signal to make the formation of firm conclusions impossible. Additional investigation was determined to be required through the use of optical spectroscopy, a common technique of plasma characterization described in Section 2.4.2, to conclude if plasma characteristics are changing with the introduction of perpendicular magnetic fields to the discharge gap.

Parallel magnetic fields alone produce a Lorentz force parallel to the workpiece surface in non-magnetic materials during  $\mu$ -EDM. These parallel force vectors have shown no effect on discharge crater volume or discharge crater characteristics, indicating that effects seen in discharge crater characteristics with the addition of a directional workpiece current would be the result of the additional perpendicular Lorentz force vector. The experimental data has shown that Lorentz forces pointing into the workpiece may alter the material removal mechanism on non-magnetic materials in  $\mu$ -EDM and enhance the erosion efficiency, while Lorentz forces pointing out from the workpiece appear to alter the flow of melt material in the discharge crater but do little to affect the erosion efficiency. Additional investigation utilizing methods that enable more precise control over the magnetic field direction and strength are required to confirm the effect of the Lorentz force on the material removal mechanism of non-magnetic materials in  $\mu$ -EDM. No tool wear is found using SEM EDS in  $\mu$ -EDM single-discharge experiments regardless of the presence of Lorentz forces.

# Chapter 4

## Further Testing of Magnetic Field-Assisted $\mu$ -EDM for Non-Magnetic Materials

The exploratory testing completed on the Lorentz force techniques yielded promising results for the Lorentz force pointing into the workpiece surface configuration by showing an increase in erosion efficiency. However, these experiments were only conducted for a single field strength produced by a permanent magnet, so the techniques' dependence on field strength could not be determined. Additionally, knowledge of the quality of the magnetic field produced by the permanent magnets was not known, thus the magnitude, direction, and uniformity of the field was assumed. Switching the magnetic field source from permanent magnets to an electromagnet would allow for testing over a variety of magnetic field strengths and provide an improvement in the quality of the magnetic field as the magnitude, direction, and uniformity of the field could all be more actively controlled. As a result, the development of a custom electromagnet that can be integrated with the  $\mu$ -EDM testbed developed during preliminary testing will be completed in this chapter. In addition to the metrics and methods of measurement utilized in the preliminary testing, the additional testing presented in this chapter will also utilize optical spectroscopy techniques to measure discharge plasma temperature and electron density and debris field characterization to measure the distance of debris particles from the discharge crater.

The final section of this chapter will propose a mechanism that is believed to be behind the Lorentz force technique. This mechanism will be backed by data collected in both Chapter 3 and

Chapter 4. The data and analysis provided in this chapter will complete the understanding of the effects of Lorentz forces on the  $\mu$ -EDM process as well as continue to fill the gap in knowledge existing for the effects of magnetic fields on the  $\mu$ -EDM plasma characteristics.

## 4.1 Electromagnet Design

To increase control over magnetic field line strength, direction, and uniformity for more in-depth experimental investigations, an electromagnet was fabricated. The electromagnet used in this research was designed with the aid of finite element model (FEM) simulations. The FEM simulation software allowed for the analysis of static two-dimensional planar electromagnetic problems by solving Maxwell's equations. Inputs required for the analysis begin with a two-dimensional drawing of the electromagnet to denote sizes, locations, and geometries of the electromagnet cores and coils. Next, materials need to be defined for the cores, coils, and surrounding medium. Finally, the number of turns and current in each coil need to be specified. The simulations then outputs magnetic field plots to determine field magnitude, direction, and uniformity.

Design criteria for the electromagnet were that the magnet had to produce a concentrated uniform orthogonal field at the workpiece surface, be capable of producing field strengths up to 1 Tesla, and the overall magnet structure could not interfere with the workpiece, electrode, or front viewing area of the testbed for optical access. To ensure uniformity of the magnetic field, symmetry was maintained in the magnet design. A solid model concept for the electromagnet design was created in ProEngineer. Figure 4.1 shows the solid model concept of the electromagnet, consisting of four magnetic coils wrapped around four cores held in place with a frame. This design meets the criteria of allowing optical access; however, it required parallel

design changes to the workpiece and electrode holders on the testbed in order to meet the design requirement of no interference between the testbed and electromagnet. After researching materials for the magnet cores and frame, 1006 steel was found to have one of the highest commercially available magnetic permeabilities, making it a prime candidate for a core material. Thus, the magnetic cores and frame were selected to be made from 1006 steel and were annealed to restore magnetic permeability lost during machining. The focal point of the four cores is designed as the location for the  $\mu$ -EDM discharge to occur.

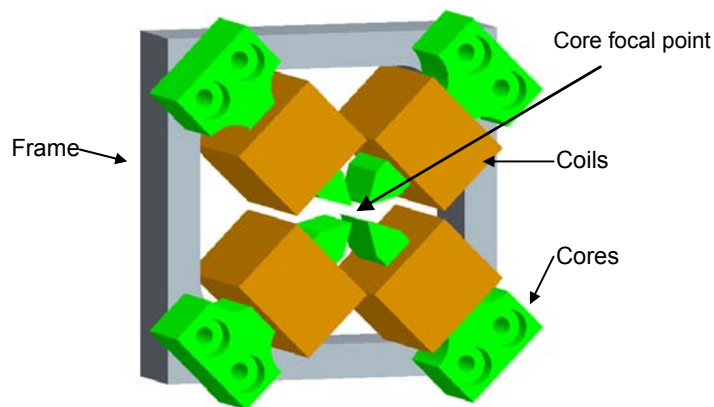


**Figure 4.1: Solid model of the electromagnet design**

The testbed design changes that were required to mate the magnet to the testbed successfully are shown in Figure 4.2 on the left. Both the electrode holder and workpiece holder were redesigned as thin sheets of aluminum to prevent deflection from magnetic forces between the holders and the electromagnet as well as to provide a slim profile to slip between the magnetic poles. The figure on the right in Fig. 4.2 shows how the magnet and testbed were designed to mate together without interference and with the workpiece and electrode holders intersecting at the focal point of the magnetic cores.

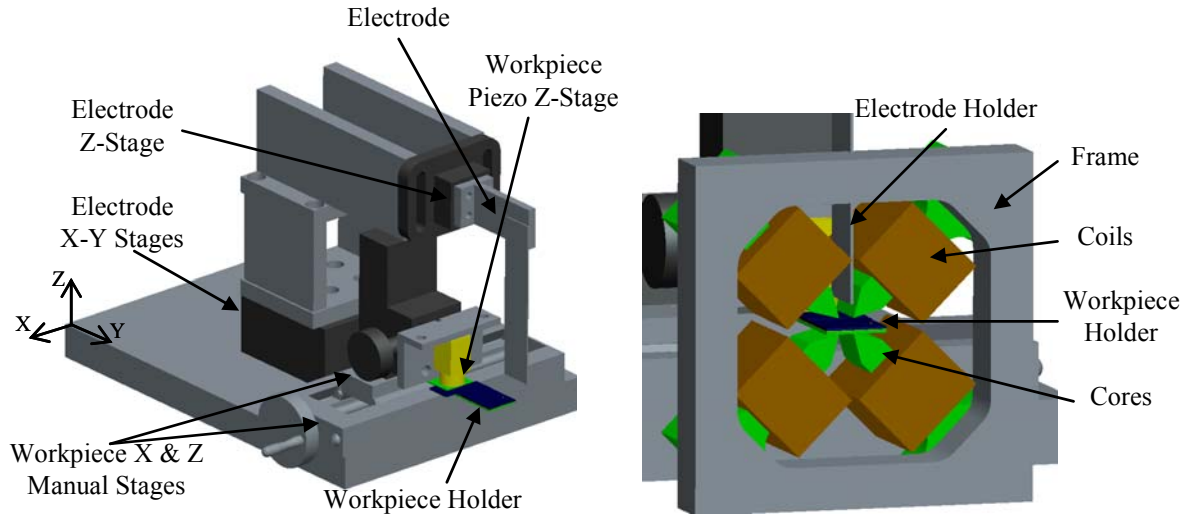


**Figure 4.2: Solid model of the redesigned  $\mu$ -EDM testbed on left and electromagnet mated to testbed on right**

The coil specifications were driven primarily by heating and space constraints. The power dissipated  $P$  in the coil is given by Eq. 4.1:

$$P = I^2 R \quad (4.1)$$

where  $I$  is the coil current and  $R$  is the coil resistance. Because electromagnetic field strength is proportional to the product of the number of turns of wire  $N$  and the current  $I$  flowing through it, increasing the number of turns while decreasing the coil current provides the best electromagnet design to prevent overheating. However, space constraints between the magnet poles as seen in Fig. 4.1 limited the number of turns of wire that could be utilized to a 25 mm long by 10 mm thick coil, thus an optimum combination of wire size and number of turns was needed.

Wire gauges ranging from 22-30 AWG were investigated as possible options. To analyze each choice, first the total number of turns permitted by space constraints of the system was determined. Next, total resistance of each coil was estimated given the number of turns in each coil and the resistance per meter for each gauge. Finally, the maximum allowable current through each coil was determined by finding the lower value from two restriction criteria. The

first restriction was the wire could not exceed 100°C at maximum current conditions, which was half of the rated wire insulation temperature. This current value was determined experimentally by monitoring wire temperature while increasing current in a sample length of wire. The second restriction was that the power supply used to power the coils was limited to a maximum output voltage of 20V. So for each wire gauge, the maximum allowable current was determined given the power supply voltage and estimated coil resistance. The lower of the two current values was then recorded as the maximum allowable current for that wire gauge to be used in the simulation.

With the information collected for each wire gauge on number of turns and maximum current, a simulation was run for each configuration to determine what wire size would be required to achieve 1T of magnetic field strength at the core focal point. Table 4.1 summarizes the results of this investigation, and it can be seen that using 800 turns of 24 AWG wire yields a maximum magnetic field strength of just under 1T with 4A of coil current, thus this configuration was chosen for the electromagnet. Figure 4.3 shows the final FEM simulation results for this configuration, with field strength denoted by the grayscale color bar located at the bottom of the figure and magnetic field lines shown as loops drawn between the upper and lower magnet cores on both the left and right side of the magnet. Notice in the detail image on the right that the field lines are nearly uniform and orthogonal to the workpiece surface at the discharge location and that the magnetic field strength is approximately 1T.

**Table 4.1: Summary of electromagnet coil wire specifications**

<u>Gauge</u> <u>[AWG]</u>	<u>Number of Turns</u> <u>[-]</u>	<u>Coil</u> <u>Resistance [Ω]</u>	<u>Maximum Allowable</u> <u>Coil Current [A]</u>	<u>Calculated Maximum</u> <u>Field Strength [T]</u>
30	2700	70	0.3	0.25
28	2000	32	0.6	0.37
26	1200	12	1.7	0.63
<b>24</b>	<b>800</b>	<b>5</b>	<b>4</b>	<b>0.988</b>
22	500	2	6.5	0.88

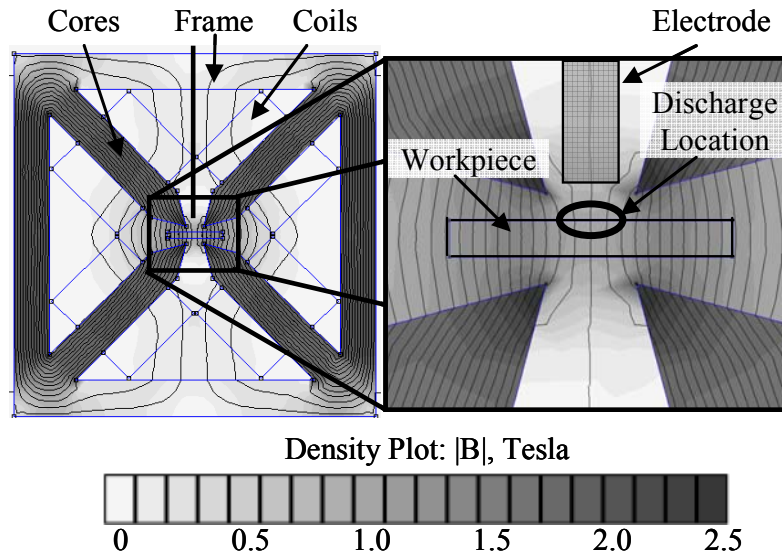


**Figure 4.3: FEM simulation results of permanent magnet design at maximum coil current**

Each core was prepared for winding by covering the core in electrical tape to prevent shorting between coil windings. The cores were then hand-wound with 800 turns of 24 AWG copper magnet wire. Once installed in the magnet frame, each core was independently connected to a switch box that allowed for independent control of pole polarity for altering the field direction while maintaining uniformity of current through each pole to keep the field symmetric. The final electromagnet setup is shown in Fig. 4.4 mounted to the testbed.

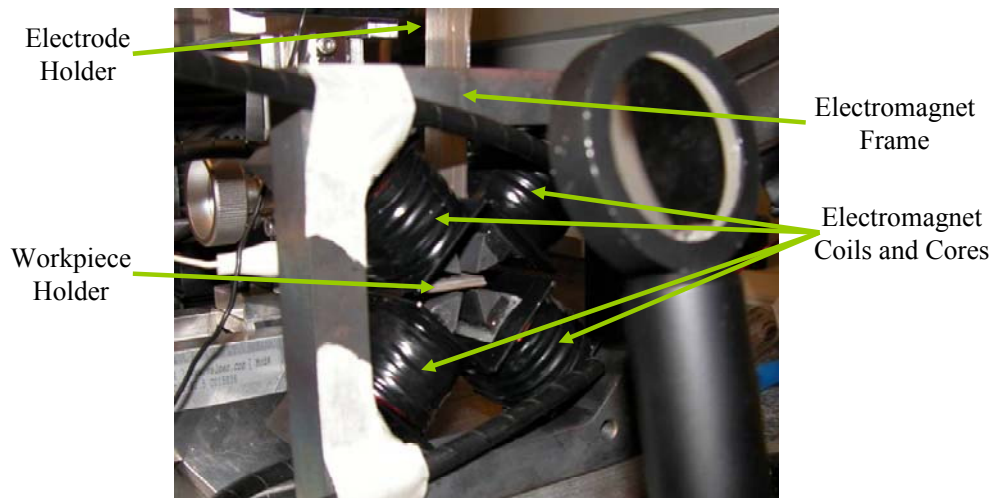


**Figure 4.4: Electromagnet on  $\mu$ -EDM testbed**

The simulation shown in Fig. 4.3 indicates that the magnetic field lines are nearly perpendicular to the workpiece surface in this configuration. The magnetic field direction can also be easily rotated by 90° to make it parallel to the workpiece surface by appropriately switching the direction of the current in each coil to change the pole of each core. When oriented parallel to the workpiece surface, the orthogonality of the magnetic field lines to the electric field lines at the workpiece surface maximizes the cross-product seen in Eq. 2.4 for maximum Lorentz force production.

## 4.2 Experimental Results for Magnetic Field Effects on Plasma Characteristics in $\mu$ -EDM

### 4.2.1 Experimental Design

Based on the inconclusive results from the perpendicular magnetic field experiments in Section 3.3, additional investigations into the effects the perpendicular magnetic field have on the  $\mu$ -EDM process were required, so a full-scale set of experiments utilizing multiple field strengths generated by the electromagnet was conducted. Test conditions for these trials are shown in Table 4.2.

**Table 4.2: Experimental conditions for electromagnet trials**

Electrode (Anode)	100 $\mu$ m diameter W wire
Workpiece (Cathode)	Grade 5 titanium (6% Al, 90% Ti, 4% V)
Gap Distance	1 $\mu$ m
Open gap voltage	100V
Discharge Power	100-150 W
Dielectric	Deionized Water
Electromagnet Strength	0.33T, 0.66T, or 1.0T

For each trial, the workpiece was prepared by polishing and cleaning and the electrode edge was blunted as described in Section 3.3.1. Because no dielectric container would fit between the magnet poles, a new method of submerging the discharge location in the dielectric was needed. Once the workpiece was mounted to the stage, a few drops of dielectric were applied to the future discharge location on the workpiece surface to form an approximately 10 mm diameter droplet. The electrode was then lowered through the meniscus of the droplet and brought into close proximity with the workpiece surface. The inter-electrode gap was set to 1  $\mu\text{m}$  in the same manner as described in Section 3.3.1.

Due to heating of the electromagnet when current is flowing through the coils, the electromagnet was kept off until just prior to a trial run. When a discharge was ready to be initiated, the electromagnet was switched on and the discharge circuit was activated. Between trials, a step-over of roughly 640  $\mu\text{m}$  was used in order to prevent overlap of debris fields between discharge craters, as the debris field was one of the metrics used in these experiments to quantify the effect of the Lorentz forces. The electrode was re-zeroed at each individual discharge location with the electromagnet on to ensure accurate gap setting during a discharge.

## 4.2.2 Perpendicular Magnetic Field Results

In order to verify if the perpendicular magnetic field can confine or stabilize the  $\mu$ -EDM discharge plasma, the plasma characteristics were examined using optical spectroscopy as described in Section 2.4.2. Figure 4.5 shows the spectroscopic equipment used to collect this data. The setup consists of two  $f/2$  lenses to focus the discharge light onto a 0.1x5mm slit in the spectroscope, where the spectrum is then captured with a 752x580 pixel camera yielding a resolution of approximately 0.5 nm/pixel.

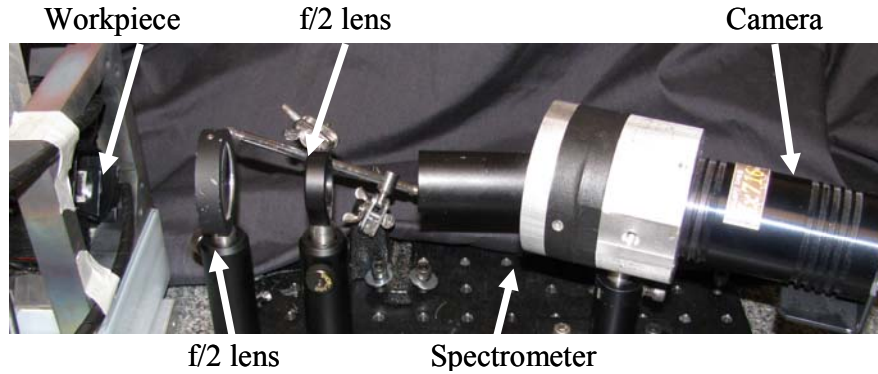


**Figure 4.5: Spectrometer setup on  $\mu$ -EDM testbed**

Three sets of spectra were collected during each experiment. First, a calibration spectrum was recorded by using a mercury lamp with distinct spectral lines at known wavelengths. Second, a dark image (no spark) was taken to allow for background subtraction from the signal images. Last, the trial discharge spectrum was collected. Examples of these three spectra can be seen in Fig. 4.6. After background subtraction, the trial spectrum exhibits both a significant amount of continuum radiation as well as convolution of many of the spectral peaks due to peak broadening brought on by instrument broadening as well as natural, Stark, and Doppler broadening. To remove the continuum radiation, several local minima were used to find a baseline, which was then removed from all the data around those minima.



**Figure 4.6: Example of spectrum collected**

To correct the convolution issue, automated peak separation analysis software [124] was used to both deconvolute and fit Voigt peaks to a range of the spectral data around the spectral lines of interest, as seen in Fig. 4.7. The upper plot shows the original data points with a line

overlaid that is produced by the convolution product of the individual deconvoluted peaks shown on the lower plot. Voigt line shapes were utilized because they combine characteristics of both a Gaussian line shape as well as a Lorentzian line shape. These two line shapes characterize different sources of peak broadening in optical spectroscopy, thus the Voigt line shape provides the most accurate model for experimental spectral data.

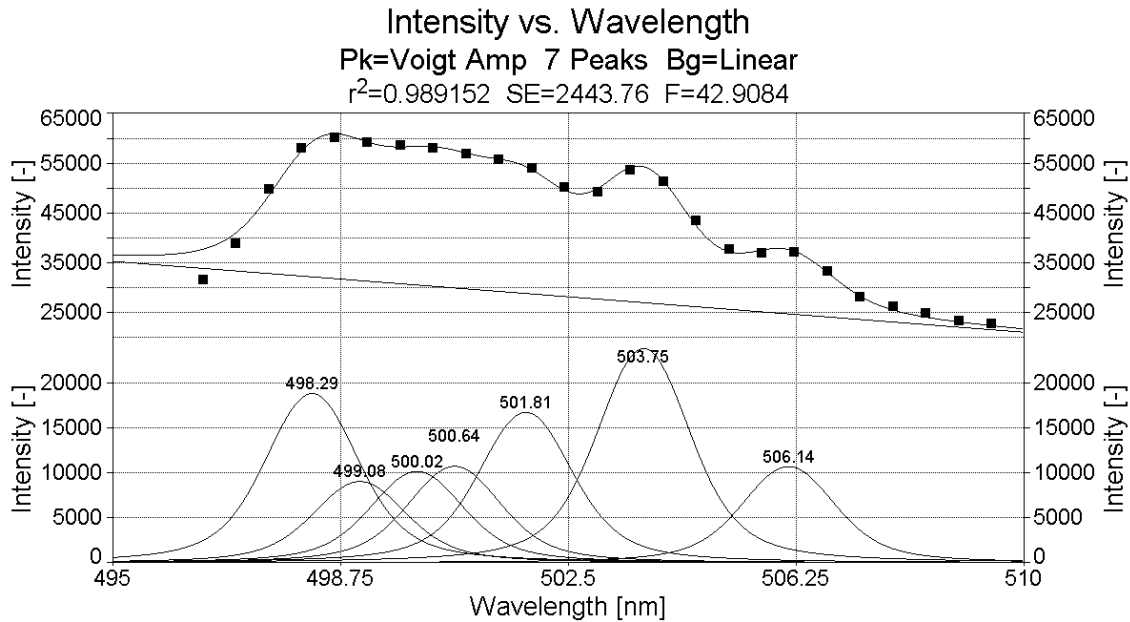


**Figure 4.7: Example of a PeakFit plot used for deconvoluting spectral data**

Once the spectrum was deconvoluted into the appropriate Voigt peaks, the areas under the 498.173nm and 521.04nm lines were determined to find the total intensity of the spectral lines for Eq. 2.1 (repeated below for convenience). The FWHM of the  $H_{\alpha}$  line was also determined at this time. Before the FWHM of the  $H_{\alpha}$  can be used in Eq. 2.2 (repeated below for convenience) for determining electron density, line broadening due to instrument effects needs to be removed as it is not accounted for in Eq. 2.2. This was done by measuring the spectral line broadening of several mercury lamp emission lines that were known to be singular wavelengths and subtracting the average FWHM of these peaks from the  $H_{\alpha}$  FWHM. Values for the remaining parameters required for use in Eq. 2.1 and Eq. 2.2 are shown in Table 4.3 [122].

**Table 4.3: Equation 2.1\* and 2.2\* Values**

Parameter	Line 1	Line 2	Units
$\lambda_n$	498.173	521.04	nm
$E_n$	26910.712	19573.973	cm <sup>-1</sup>
$k$	0.695035613	0.695035613	cm <sup>-1</sup> /K
$I_n$	Measured	Measured	-
$g_n$	13	9	-
$A_n$	0.66	0.0411	10 <sup>8</sup> s <sup>-1</sup>

$$*\text{Eq. 2.1: } T = \frac{-(E_1 - E_2) / k}{\ln\left(\frac{I_1 \lambda_1 g_2 A_2}{I_2 \lambda_2 g_1 A_1}\right)}; \quad *\text{Eq. 2.2: } n_e = 8.8308 \cdot 10^{16} \cdot (\Delta\lambda_w)^{1.6005}$$

Table 4.4 summarizes the plasma temperature and electron densities for the perpendicular field experiments. No correlation is seen between field strength and average plasma temperature or electron density. If any difference were to be present in the plasma temperature and electron density data, it would be between the 0.33T and 1.00T field strengths as it is the largest difference in field strength tested, so a t-test with a 0.1 level of significance was conducted between these data sets. For the temperature data, the test statistic is  $t_{\text{calc}}=0.857$  with a rejection criteria of  $t_{\text{crit}}=1.86$  to reject the hypothesis of equal true means, thus there is no evidence to suggest temperature changes with field strength. Similarly for the electron density, the test statistic is  $t_{\text{calc}}=0.775$  with the same rejection criteria, thus there is no evidence to suggest electron density changes with field strength either.

The standard deviation of the electron density appears to increase with increasing field strength, but an F-test at a level of significance of 0.1 does not support this conclusion. For the 0.33T and 0.66T data, the test statistic is  $F_{\text{calc}}=3.568$  with a rejection criteria of equal true variances of  $F_{\text{crit}}=5.19$ . For the 0.66T and 1.00T data, the test statistic is  $F_{\text{calc}}=2.522$  with a rejection criteria of equal true variances of  $F_{\text{crit}}=6.59$ . Thus, there is no evidence to suggest a difference of true variances in these tests.

**Table 4.4: Plasma Characteristics for Perpendicular Field Experiments**

Trial	<u>0.33T</u>		<u>0.66T</u>		<u>1.00T</u>	
	Temperature [K]	Electron Density [ $1 \times 10^{17} \text{ cm}^{-3}$ ]	Temperature [K]	Electron Density [ $1 \times 10^{17} \text{ cm}^{-3}$ ]	Temperature [K]	Electron Density [ $1 \times 10^{17} \text{ cm}^{-3}$ ]
1	5260	4.3	5120	1.7	5520	3.6
2	5980	5.7	5030	2.0	4300	5.3
3	5650	7.0	4990	5.6	5830	11.8
4	5370	7.7	5050	8.6	6650	15.1
5	7540	8.6	4510	8.6	5060	-
6	-	9.1	-	-	-	-
Average	<b>5960</b>	<b>7.1</b>	<b>4940</b>	<b>5.3</b>	<b>5472</b>	<b>8.9</b>
Standard Deviation	<b>926</b>	<b>1.8</b>	<b>245</b>	<b>3.4</b>	<b>875</b>	<b>5.4</b>

Average plasma temperature is in the range of 5000K-6000K, which is significantly colder than macro-scale EDM plasmas, which are reported to be on the average of 8000K [66]. The average electron density is between  $5 \times 10^{17} \text{ cm}^{-3}$  and  $9 \times 10^{17} \text{ cm}^{-3}$ , which is somewhat less dense than the electron density in macro-scale EDM plasmas that are on the order of  $10^{18} \text{ cm}^{-3}$  as reported by Descoudres [66]. The micro-EDM plasmas produced in these experiments using a liquid dielectric are also significantly denser than micro-plasmas produced in air. Noguchi et al. [125] reported micro-discharge plasma electron densities using a gaseous dielectric between  $0.2-3 \times 10^{13} \text{ cm}^{-3}$  and Ito et al. [126] reported electron densities on the order of  $10^{15} \text{ cm}^{-3}$  for similar plasmas in air. Using an average plasma temperature of 5500K and an average electron density of  $7 \times 10^{17} \text{ cm}^{-3}$ , the mean inter-particle distance for the perpendicular field experiments can be estimated as  $a=7\text{nm}$ , the Debye length is estimated at  $\lambda_D=6\text{nm}$ , and the coupling factor  $\Gamma=0.434$ . These plasma characteristics are in agreement with those found by Descoudres for macro-scale EDM plasmas within their first microsecond ( $a=6\text{nm}$ ;  $\lambda_D=6\text{nm}$ ;  $\Gamma=0.45$ ) [66].

These results indicate that the plasma is non-ideal and the inter-particle distance is roughly the same as the Debye length, resulting in significant electrostatic interactions between particles. This is likely the reason that no increase in plasma temperature or electron density is measured with increasing field strength in these experiments. The containment effects of the magnetic fields are significantly weaker than the electrostatic interactions between particles, thus further compression of the plasma by magnetic confinement is not probable. It can be concluded that perpendicular magnetic fields up to 1T in strength do not provide any additional plasma confinement or stability.

## 4.3 Experimental Results for Magnetic Field-Assisted $\mu$ -EDM using Lorentz Forces

### 4.3.1 Lorentz Force Pointing into Workpiece Surface Results

The results reported in Section 3.4.3 had evidence to suggest that the addition of the Lorentz force pointing into the workpiece surface alters the mechanism of material removal by showing changes in discharge crater depth of 30.5% and overall erosion volume of 38.2%. Additionally, statistically significant results were shown that the erosion efficiency was increased by 25% with the addition of the Lorentz force in this configuration versus a standard  $\mu$ -EDM discharge. As a result, additional trials were run at three different field strengths using the electromagnet as the magnetic field source to further explore the effects of the Lorentz force on the  $\mu$ -EDM process.

**Volume analysis and erosion efficiency.** In Section 3.4.3, the positive discharge crater volume was found to increase by 30.5%, negative volume decreased by 11% and erosion volume increased 38.2%, resulting in a 25% increase in erosion efficiency in the Lorentz force into the

workpiece trials. To confirm these results, similar data was collected for the electromagnet experiments using 3D laser surface scanning as was described in Section 3.4.2. A sample of the 3D images of the discharge craters from these trials is shown in Fig. 4.8. Table 4.5 compares the volume data and erosion efficiencies for these trials.

**Table 4.5: Summary of Lorentz Force into workpiece experiments**

<b>0.33T</b>				
<b>Trial</b>	<b>Positive Volume [<math>\mu\text{m}^3</math>]</b>	<b>Negative Volume [<math>\mu\text{m}^3</math>]</b>	<b>Erosion Volume [<math>\mu\text{m}^3</math>]</b>	<b>Erosion Efficiency [%]</b>
1	2733	841	1893	3.01%
2	1490	93	1397	2.27%
3	2563	620	1943	3.36%
4	3930	483	3316	5.45%
Average	<b>2679</b>	<b>509</b>	<b>2137</b>	<b>3.52%</b>
Standard Deviation	<b>999</b>	<b>314</b>	<b>824</b>	<b>1.36%</b>
<b>0.66T</b>				
<b>Trial</b>	<b>Positive Volume [<math>\mu\text{m}^3</math>]</b>	<b>Negative Volume [<math>\mu\text{m}^3</math>]</b>	<b>Erosion Volume [<math>\mu\text{m}^3</math>]</b>	<b>Erosion Efficiency [%]</b>
1	1807	135	1672	2.89%
2	2721	165	2556	5.21%
3	3987	425	3563	5.85%
4	4441	343	4098	6.57%
5	4215	200	4016	6.58%
Average	<b>3434</b>	<b>253</b>	<b>3181</b>	<b>5.42%</b>
Standard Deviation	<b>1128</b>	<b>125</b>	<b>1043</b>	<b>1.53%</b>
<b>1.00T</b>				
<b>Trial</b>	<b>Positive Volume [<math>\mu\text{m}^3</math>]</b>	<b>Negative Volume [<math>\mu\text{m}^3</math>]</b>	<b>Erosion Volume [<math>\mu\text{m}^3</math>]</b>	<b>Erosion Efficiency [%]</b>
1	2536	499	2036	3.16%
2	4990	128	4862	8.26%
3	3819	342	3477	5.93%
4	2162	31	2131	4.99%
Average	<b>3377</b>	<b>250</b>	<b>3127</b>	<b>5.59%</b>
Standard Deviation	<b>1289</b>	<b>211</b>	<b>1331</b>	<b>2.12%</b>

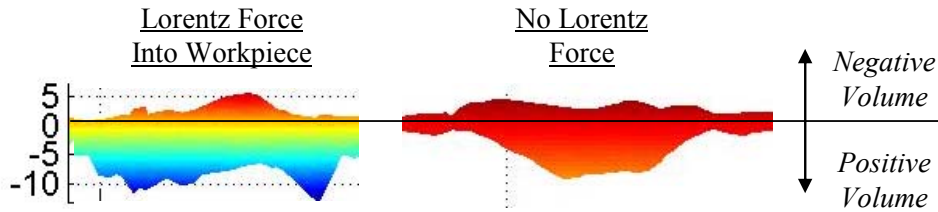


**Figure 4.8: Samples of the 3D laser scanning images taken of the discharge craters**

When the field strength is increased from 0.33T to 0.66T, there is an increase in erosion efficiency of 54%, but there is only an increase of 3% from 0.66T to 1T. To test for significance, a t-test using a level of significance of 0.1 was conducted between the 0.33T and 0.66T erosion efficiency data. The test statistic for this data was  $t_{\text{calc}}=1.940$  with a rejection criteria of  $t_{\text{crit}}=1.895$  to reject the hypothesis of equal true means, thus there is evidence to suggest the erosion efficiency is increased with increasing field strength. This indicates that significantly more material is removed per unit of spark energy going into each discharge when the magnetic field is 0.66T, however there is little evidence to show that increasing the field strength any higher than this will result in any significant increase in MRR.

To further understand the cause of this increase in erosion efficiency, it can be seen that there is an increase in positive volume of approximately 28% and a decrease in negative volume of 50% between the 0.33T and 0.66T field strengths. This indicates that there is more material removed from the melt pool below the workpiece surface for the increased field strength case, and this volume is not transported to the rim, but is instead completely removed from the melt pool, as evidenced by the decrease in negative volume. These results confirm the findings reported in Section 3.4.3 of increased erosion efficiency due to improved material removal.

**Plasma characteristics.** The increases in positive volume noted with the Lorentz force pointing into the workpiece surface could be the result of either mechanical effects such as increased debris ejection and/or thermal effects such as an increase in plasma temperature. The discharge plasma will be investigated first for changes resulting from the Lorentz force pointing

into the workpiece process. Table 4.6 shows the temperature and electron density data for the Lorentz force pointing into the workpiece experiments. No significant difference is seen in the plasma temperature for the three field strengths. The electron density does appear to decrease at higher field strengths, as the 0.33T field strength electron density ( $7.3 \times 10^{17} \text{ cm}^{-3}$ ) is somewhat higher than the electron densities at 0.66T ( $2.6 \times 10^{17} \text{ cm}^{-3}$ ) and 1.00T ( $3.1 \times 10^{17} \text{ cm}^{-3}$ ). However, the standard deviation in the 0.33T trial can be seen to be significantly higher than the standard deviation reported for either the 0.66T or 1.00T trials. Thus, to confirm that there was no reason to believe a difference in true means existed, a t-test for significance was conducted and showed no evidence to suggest a difference of true means between these trials. The test statistic was  $t_{\text{calc}}=0.929$  and the rejection criteria at a level of significance of 0.1 was  $t_{\text{crit}}=1.86$ , thus there is no evidence to reject the hypothesis of equal true means.

**Table 4.6: Plasma Characteristics for Parallel Field Experiments**

Trial	0.33T		0.66T		1.00T	
	Temperature [K]	Electron Density [ $1 \times 10^{17} \text{ cm}^{-3}$ ]	Temperature [K]	Electron Density [ $1 \times 10^{17} \text{ cm}^{-3}$ ]	Temperature [K]	Electron Density [ $1 \times 10^{17} \text{ cm}^{-3}$ ]
1	3556	0.3	4175	1.2	4692	0.4
2	5952	0.3	4752	1.2	5421	1.4
3	5211	2.4	4261	1.7	5265	1.9
4	4929	10.0	5551	2.6	5119	3.4
5	5133	23.6	5429	6.1	4846	8.2
Average	<b>4956</b>	<b>7.3</b>	<b>4834</b>	<b>2.6</b>	<b>5069</b>	<b>3.1</b>
Standard Deviation	<b>873</b>	<b>9.9</b>	<b>640</b>	<b>2.0</b>	<b>299</b>	<b>3.1</b>

At the lower field strength, the inter-particle distance, Debye length, and coupling factor are  $a=7\text{nm}$ ,  $\lambda_D=6\text{nm}$ , and  $\Gamma=0.434$ , indicating the plasma is non-ideal and there are significant electrostatic interactions between particles. At the higher field strengths however, the inter-particle distance increases to  $a=9.4\text{nm}$ , Debye length increases to  $\lambda_D=9\text{nm}$ , and the coupling

factor is  $\Gamma=0.356$ . These results show that for the increased field strength, the plasma experiences greater expansion, as depicted by the larger inter-particle distance. However, the Debye length increases as well so the resulting plasma does not become any more ideal.

When the electric field is perpendicular to the magnetic field, as is the case in these experiments, the electrons develop a path of travel that is more restrictive than the straight path normally seen in an electric field, as seen in Fig. 4.9. The particle motion shown is a 2-D in-plane motion that occurs as the result of the electron both moving along the electric field lines as well as orbiting about the magnetic field lines [127].

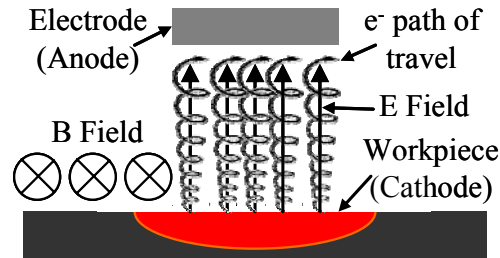


**Figure 4.9: Electron path of travel when E-field and B-field are perpendicular**

The small decrease in electron density at higher field strengths seen in Table 4.6 could be the result of increased resistance for electron travel caused by tighter orbits in the non-uniform path of travel shown in Fig. 4.9. Higher resistance to electron travel causes fewer electrons to be transported across the electrode gap, resulting in a lower electron density. These results suggest that the increased erosion efficiency reported for the Lorentz force pointing into the workpiece case is likely not due to increased plasma temperature or electron density.

**Debris Field Characteristics.** With the Lorentz force pointing into the workpiece surface, increases in positive volume and erosion efficiency occurred. By examining the debris field characteristics, it is possible to determine if material ejection is modified by the Lorentz force, causing increased erosion efficiency. SEM imaging of the area surrounding the discharge crater was used to collect information on the debris field that formed around the crater, as no debris

flushing techniques were employed so the debris ejected from each discharge crater settled in the immediate proximity of the crater on the workpiece surface. By quantifying the characteristics of the debris field, insight can be had into any effects the magnetic forces may be having on material ejection from the melt pool and discharge gap.

SEM images were taken of each discharge area and the distance of every debris particle 2  $\mu\text{m}$  or larger contained inside a 640  $\mu\text{m}$  diameter zone, centered on the discharge crater, was measured from the discharge crater center as shown in Fig. 4.10. The particle size cutoff of 2  $\mu\text{m}$  was due to the fact that particles any smaller than that were difficult to distinguish from other surface features on the workpiece, so data could not be reliably collected below this cutoff. The debris field zone diameter of 640  $\mu\text{m}$  was chosen because it is the distance between discharge craters set by the step-over size discussed in Section 4.2.

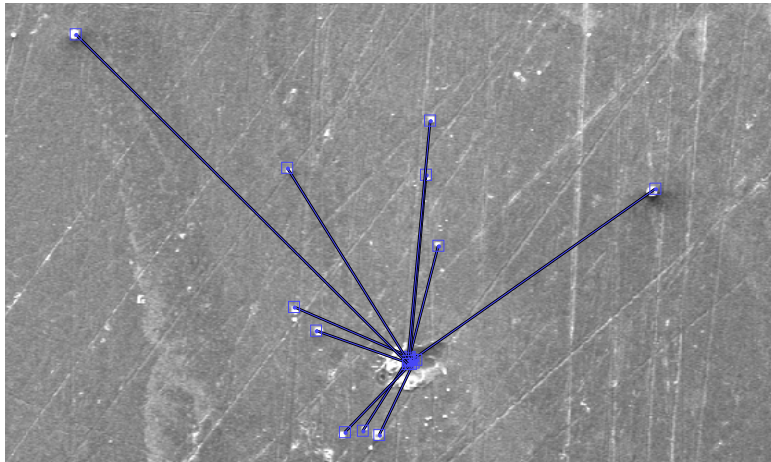


**Figure 4.10: Example of the measurements taken from the debris field**

Figure 4.11 shows the results from 17 discharges done with and without the Lorentz force at a field strength of 1T and with the debris data collected as specified. It can be seen that when the Lorentz force is applied into the workpiece, the discharge debris distance shifts towards values further away from the crater. The average debris distance without the Lorentz force is 164 $\mu\text{m}$ , whereas with the Lorentz force applied, the average increases to 207 $\mu\text{m}$ . More importantly

though, is the 0-50 $\mu\text{m}$  category. The diameter of the electrode is 100 $\mu\text{m}$ , so any particles less than 50 $\mu\text{m}$  from the discharge center have not been cleared from the discharge gap (assuming the discharge occurs at the center of the electrode). In the Lorentz force case, there are no debris particles in the 0-50 $\mu\text{m}$  range. This is important in  $\mu\text{-EDM}$  as debris particles stuck in the gap can cause subsequent abnormal discharges, thus eliminating particles in this category is desirable.

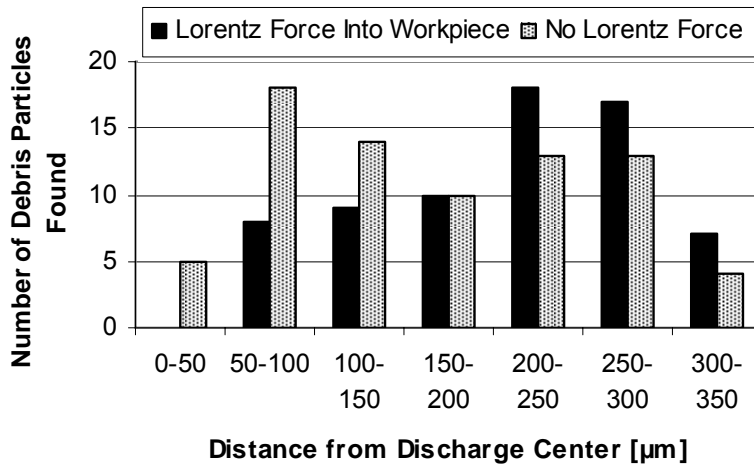


**Figure 4.11: Debris field distribution for the Lorentz force pointing into the workpiece surface configuration**

### 4.3.2 Lorentz Force Pointing Outward From Workpiece Surface Results

In Section 3.4.4, preliminary testing of the Lorentz force pointing out from the workpiece surface configuration revealed that the average negative volume decreased by 43% and the average positive volume decreased by 23%, but the erosion volume only decreased by 15% and erosion efficiency was unaffected. This led to speculation that this configuration of the Lorentz force may be affecting the *movement* of material in the discharge crater, but not actually affecting the *removal* of the material from the crater. To gain additional insight into these results, trials were run at three different field strengths using the electromagnet as the source of the magnetic field and the same 3D laser scanning techniques were used to collect discharge

crater volume data. A sample of the 3D images of the discharge craters is shown in Fig. 4.12.

Table 4.7 compares the volume data and erosion efficiencies for these trials.

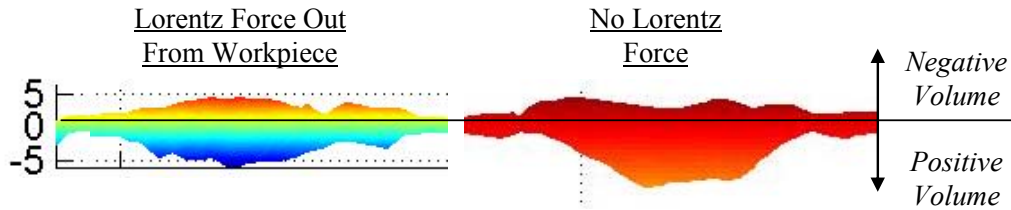


Figure 4.12: Samples of the 3D laser scanning images taken of the discharge craters

Table 4.7: Summary of Lorentz force pointing out from the workpiece experiments

	<u>0.33T</u>			
<b>Trial</b>	<b>Positive Volume [<math>\mu\text{m}^3</math>]</b>	<b>Negative Volume [<math>\mu\text{m}^3</math>]</b>	<b>Erosion Volume [<math>\mu\text{m}^3</math>]</b>	<b>Erosion Efficiency [%]</b>
1	3086	448	2423	3.69%
2	2975	860	2115	2.96%
3	3599	1232	2367	3.77%
4	2763	348	2416	3.55%
5	2898	1029	1869	3.00%
Average	<b>3106</b>	<b>722</b>	<b>2330</b>	<b>3.49%</b>
Standard Deviation	<b>321</b>	<b>377</b>	<b>242</b>	<b>0.39%</b>
	<u>0.66T</u>			
<b>Trial</b>	<b>Positive Volume [<math>\mu\text{m}^3</math>]</b>	<b>Negative Volume [<math>\mu\text{m}^3</math>]</b>	<b>Erosion Volume [<math>\mu\text{m}^3</math>]</b>	<b>Erosion Efficiency [%]</b>
1	3025	604	2421	3.53%
2	2088	967	1120	2.11%
3	2263	172	1892	2.96%
Average	<b>2459</b>	<b>581</b>	<b>1811</b>	<b>2.87%</b>
Standard Deviation	<b>498</b>	<b>398</b>	<b>654</b>	<b>0.71%</b>
	<u>1.00T</u>			
<b>Trial</b>	<b>Positive Volume [<math>\mu\text{m}^3</math>]</b>	<b>Negative Volume [<math>\mu\text{m}^3</math>]</b>	<b>Erosion Volume [<math>\mu\text{m}^3</math>]</b>	<b>Erosion Efficiency [%]</b>
1	1818	278	1658	2.77%
2	2351	863	1488	2.15%
3	2095	470	1625	2.89%
4	1061	506	555	1.25%
Average	<b>1831</b>	<b>529</b>	<b>1332</b>	<b>2.26%</b>
Standard Deviation	<b>558</b>	<b>244</b>	<b>523</b>	<b>0.75%</b>

Table 4.7 shows a decrease in erosion efficiency of 15% when increasing the field strength from 0.33T to 0.66T and a decrease of 21% from 0.66T to 1T. Comparing the results of the 0.33T and 1T trials in a t-test for significance shows that the test statistic is  $t_{\text{calc}}=3.202$  and the rejection criteria of a equal true means is  $t_{\text{crit}}=1.895$  at a 0.1 level of significance, so there is evidence to support a decrease in the true mean of erosion efficiency with increasing field strength. This indicates that material removal actually is hindered with increasing field strength when the Lorentz force is oriented to point out from the workpiece surface. Positive volume trends show a decrease of 20% and 26% with each step increase in field strength and the negative volume decreases by 26% and 9% as well, which are in agreement with the preliminary results seen in Section 3.4.4. This can even be seen in Fig. 4.12, where the Lorentz force case appears to have less peak-to-valley height difference than the standard discharge case. This indicates an overall decrease in the transport of melt pool material from the crater to the rim during a discharge, thus the reduced erosion efficiency seen in Table 4.7 is likely due to this damping of the melt pool movement during a discharge.

## 4.4 Proposed Mechanism of Material Removal for the Lorentz Force Process

In Chapter 3, preliminary testing was done on the Lorentz force process. It was determined that the Lorentz forces acting parallel to the melt pool surface did not affect any of the measured metrics, but when a directional workpiece current was added to induce a Lorentz force acting perpendicular to the workpiece surface, changes were noticed in the discharge crater characteristics. With the Lorentz force pointing into the workpiece surface, it was noted that the positive discharge crater volume increased by 30.5%, negative volume decreased by 11% and

erosion volume increased 38.2%, resulting in a 25% increase in erosion efficiency. With the Lorentz force pointing outward from the workpiece surface, it was noted that the average negative volume decreased by 43% and the average positive volume decreased by 23%, but the erosion volume only decreased by 15% and the erosion efficiency was unaffected. As a result, it was suspected that the Lorentz force pointing into the workpiece surface was aiding the material removal mechanism to increase MRR, but when pointing out from the workpiece surface, the Lorentz force merely altered the flow of melt pool material during a discharge without affecting the overall efficiency of the process.

Chapter 4 further investigated these findings by conducting trials over multiple field strengths and collecting the same crater volume data as well as collecting spectroscopic data to note changes in discharge plasma characteristics and collecting debris field data to shed light on the mechanism at work in the process. For the Lorentz force pointing into the workpiece surface, an increase in erosion efficiency of 54% was noted between the 0.33T and 0.66T field strengths in addition to an increase in positive volume of approximately 28% and a decrease in negative volume of 50%. Debris distance was found to increase as well with the Lorentz force pointing into the workpiece surface while the discharge plasma characteristics did not change with the addition of the Lorentz force. For the Lorentz force pointing out from the workpiece surface, a decrease in erosion efficiency of 15% when increasing the field strength from 0.33T to 0.66T was accompanied by a decrease in positive volume of 20% and a decrease in negative volume of 26%. The decrease in erosion efficiency seen in this testing did not appear in the preliminary testing, likely because only a single field strength was tested in those experiments so the change was not noticeable. These results solidified the hypothesis that the Lorentz force pointing into the workpiece surface was aiding in material removal and that the Lorentz force pointing outward

from the workpiece surface was hindering material transport in the melt pool, causing the erosion efficiency to decrease slightly.

Based on this data along with SEM images, debris field data, and plasma channel data, melting and splashing are suspected as the material removal mechanism in  $\mu$ -EDM, as is also suggested by Wang et al. [57] and discussed in Section 2.2.1. In the melting/splashing model, the plasma channel causes workpiece material to melt, starting at the center of the plasma channel, and growing both axially into the workpiece surface and radially along the workpiece surface. The melted material flows radially to the edge of the discharge crater due to the Marangoni effect [59], creating a rim of material around the crater [57] as can be seen in Fig. 4.13. Some of the material built up on the rim is removed via splashing due to recoil forces produced upon plasma channel collapse [52].

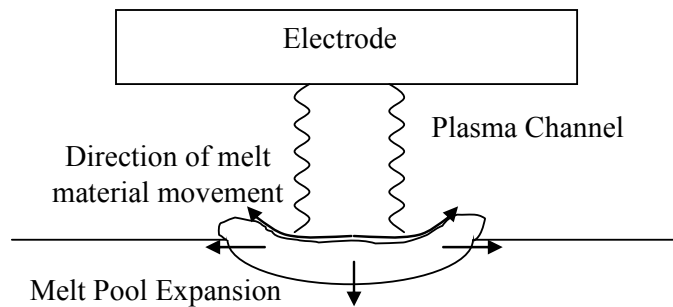


**Figure 4.13: Movement of the melt pool material during a  $\mu$ -EDM discharge**

The melting/splashing mechanism of material removal can be verified given the efficiency data in Table 4.5 and Table 4.7. The erosion efficiencies seen in Table 4.5 and Table 4.7 are based on the melting/splashing assumption and are in agreement with those found by Wang et al. [57], who reported an erosion efficiency of 3.31% for titanium assuming melting/splashing. Calculations run for erosion efficiency using vaporization as the primary material removal

mechanism by substituting  $H_v$ , the enthalpy of vaporization ( $1.089 \times 10^4$  kJ/kg), for  $H_m$  in Eq. 3.1 yield efficiencies well over 50%, far too large to be reasonable. Thus, the discharges examined in this study can be assumed to follow the model of melting/splashing as the primary material removal mechanism.

Based on the observation of both increased positive volume and increased debris distance for the Lorentz force pointing into the workpiece case, additional melt material is likely pushed away from the bottom of the melt pool as shown by the schematic in Fig. 4.14a as a result of this added Lorentz force. This is conceptually similar to the process of laser hole drilling as proposed by von Allmen et al. [128], who describes the vapor pressure above the melt pool as a piston that exerts force downward on the melt pool. In addition to the vapor pressure providing the piston force in  $\mu$ -EDM, the Lorentz force now directly applies force to the melt pool.

The vapor pressure of the plasma above the melt pool is reported to be on the order of several bar (several hundred kN/m<sup>2</sup>) by Descoedres [66]. Based on a melt pool diameter of 50 $\mu$ m, the Lorentz force in these experiments would exert approximately 100 $\mu$ N (50 kN/m<sup>2</sup>) of force on the melt pool, which is in the same order of magnitude as the existing plasma pressure.

By adding the Lorentz force pointing into the workpiece surface, the melt pool effectively experiences an increased pressure above it. This clears away additional melted material from the bottom of the discharge crater, exposing new workpiece material to the plasma during a discharge, creating a deeper crater. Melted material is transported up the sides of the crater to the crater rim, where it is removed by splashing after the plasma channel collapses as suggested in Fig. 4.14b. This flow structure for melted material may also add stability to the process, resulting in the increased uniformity of the discharge pools seen in Fig. 3.23.

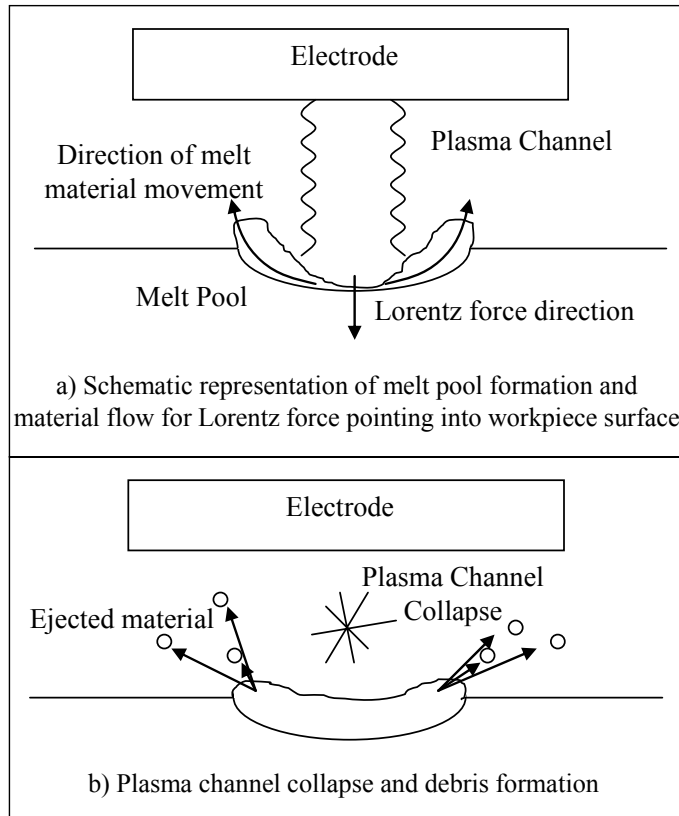


**Figure 4.14: Melting/Splashing material removal mechanism**

For the Lorentz force pointing outward from the workpiece surface, the decreased negative and positive discharge crater volumes reported in Section 3.4.4 and Section 4.3.2 suggest that the melt pool is prevented from flowing outward and is instead trapped at the center of the discharge crater. This result is undesirable because once the workpiece material has reached its melting point it needs to be removed from the melt pool as further heating is a waste of energy with no additional benefit to material removal, which explains the decrease in erosion efficiency reported in Table 4.7.

The Lorentz force oriented outward from the workpiece surface likely causes the entire melt pool to experience a force upward, similar to how a pool of water would behave if a vacuum were placed over it. With the current configuration, this force is too weak to overcome the surface tension in the melt pool and the plasma pressure over the melt pool to remove molten

material, thus the Lorentz force simply ends up impeding the flow of material towards the rim, causing both the positive and negative volumes to significantly decrease when compared to the no field case and resulting in a loss of erosion efficiency.

## 4.5 Chapter Summary

Permanent magnets have been used to conduct proof of concept trials and a summary of these trials has been provided in Section 3.5. Following successful proof of concept trials, more in-depth trials were conducted utilizing an electromagnet as the source of the magnetic field to allow multiple field strengths to be tested. To enable these studies, the design and fabrication of a custom electromagnet has been completed. The electromagnet experiments utilized 3D imaging techniques to analyze discharge crater volume and erosion efficiency, SEM imaging to determine debris field distribution, and spectral analysis to determine plasma characteristics.

Perpendicular magnetic fields were found to have no effect on plasma temperature or electron density, indicating that this particular magnetic field orientation has no effect on plasma confinement. The parallel magnetic fields used in the Lorentz force-assisted  $\mu$ -EDM technique were shown to have little effect on plasma temperature or plasma density, indicating that the addition of the Lorentz force to the  $\mu$ -EDM process likely has a mechanical effect on the material removal mechanism.

For the Lorentz force pointing into the workpiece surface trials, discharge crater volume data and erosion efficiency data was found to be in agreement with the preliminary data found in Chapter 3 indicating an increase in erosion efficiency of 54% between the 0.33T and 0.66T field strength trials. In addition, the debris distance was found to increase with the addition of this configuration of the Lorentz force. Based on these results, a modified mechanism of material

removal has been proposed based these findings. With the Lorentz force pointing into the workpiece, the pressure on the melt pool is increased, causing more material to be transported to the crater rim, where it is removed as debris upon plasma channel collapse, thereby increasing erosion efficiency.

The data from the Lorentz force pointing out from the workpiece surface trials was also found to be in agreement with the data from Chapter 3. Positive volume decreased by 20% and 26% with each step increase in field strength and the negative volume decreased by 26% and 9% as well, indicating the flow of molten material has been hindered in the melt pool with the addition of the Lorentz force in this configuration. It was also found that when comparing the 0.33T field strength to the 1.00T field strength, the noted decrease in erosion efficiency of 35% was statistically significant at the 0.1 level of significance, suggesting that hindering the flow of melt pool material does decrease erosion efficiency. With the Lorentz force pointing out from the workpiece surface, it is suggested that the melt pool feels a force similar to that which would be felt by a pool of water with a vacuum placed over it. If it were possible to increase this force enough to overcome the plasma pressure and surface tension of the melt pool, additional material may be removed, however with the force values seen in these experiments, the Lorentz force only works to hinder the movement of melt pool material in this configuration.

# Chapter 5

## Conclusions and Recommendations

### 5.1 Summary of Research Objective and Scope

The objective of this thesis was to develop a magnetic field-assisted  $\mu$ -EDM process to improve MRR regardless of workpiece magnetic properties. Through fundamental investigation of single spark discharges on non-magnetic workpiece materials, two methods to achieve the objective goal were analyzed. The first technique developed was aimed at altering the discharge plasma channel through the use of magnetic fields to affect plasma confinement and/or plasma stability. The second technique developed aimed to improve the material removal mechanism of the  $\mu$ -EDM process through the use of Lorentz forces induced in the melt pool.

The scope of this research was to focus on the magnetic field interactions with the  $\mu$ -EDM discharge process to determine the effects on the process mechanics. This was completed in the context of single-spark discharges on Grade 5 titanium alloy using a tungsten wire electrode. Only deionized water was used as a dielectric. The magnetic fields were produced first by permanent magnets for proof of concept experimentation, and later by electromagnets during full-scale testing.

### 5.2 Conclusions

The following is a set of specific conclusions that can be drawn from this work:

## **Design of Experiments**

1. A  $\mu$ -EDM testbed was designed and constructed for the purpose of investigating the effects of magnetic field-assisted  $\mu$ -EDM techniques on the fundamental characteristics of single spark discharges on non-magnetic workpiece materials. A hybrid RC-transistor single pulse discharge circuit capable of low-energy short-duration controlled single discharges was also developed to enable this investigation. An electromagnet capable of producing a uniform magnetic field up to 1T in strength and orthogonal to the workpiece surface was designed and constructed for the purpose of additional investigation into the effects of magnetic field-assisted techniques on the fundamentals of the  $\mu$ -EDM discharge process for non-magnetic workpiece materials.
2. Metrics used to characterize the single spark  $\mu$ -EDM discharge process were developed and methods used to measure these characteristics were outlined. The metrics included discharge crater area analysis, high-speed plasma imaging analysis, discharge crater volume analysis, erosion efficiency analysis, plasma temperature and electron density analysis, and debris field analysis.

## **Magnetic Confinement and Stabilization of $\mu$ -EDM Plasma**

3. In initial experiments using a permanent magnet as the source of the magnetic field, discharge crater area shows no sign of change by the introduction of perpendicular magnetic fields, indicating plasma confinement is unlikely. However, there is evidence at a level of significance of 0.1 to suggest that these fields decrease the standard deviation of the discharge crater area, indicating the possibility of enhanced plasma channel stability.

4. Through additional testing using an electromagnet as the source of the magnetic field, the average and standard deviation of the plasma temperature and electron density are found to be unaffected by the addition of perpendicular magnetic fields up to 1T in the  $\mu$ -EDM discharge process, confirming that perpendicular magnetic fields have no effect on plasma confinement or stability.
5. The parallel magnetic fields used in the Lorentz force process do not affect plasma temperature. Electron density may appear to decrease slightly between field strengths of 0.33T ( $n_e=7.3 \times 10^{17} \text{ cm}^{-3}$ ) and 0.66T ( $n_e=2.6 \times 10^{17} \text{ cm}^{-3}$ ) due to an increase in transport resistance for the electrons in the plasma channel; however, this has not been shown to be a statistically significant result at a level of significance of 0.1.
6. Calculations show that the  $\mu$ -EDM discharge plasma is non-ideal and the inter-particle distance is roughly the same as the Debye length ( $a=7\text{nm}$ ,  $\lambda_D=6\text{nm}$ ,  $\Gamma=0.434$ ), which is consistent with macro-scale EDM plasmas in their first microsecond. Average  $\mu$ -EDM plasma temperature is in the range of 5000-6000K and average electron density is between  $5 \times 10^{17} \text{ cm}^{-3}$  and  $9 \times 10^{17} \text{ cm}^{-3}$ , indicating  $\mu$ -EDM plasmas are colder and less dense than macro-scale EDM plasmas.

#### **Lorentz Force Effects on $\mu$ -EDM Material Removal Mechanism**

7. Magnetic fields oriented parallel to the workpiece surface as in the Lorentz process show no evidence to suggest changes in the discharge crater morphology at a level of significance of 0.1. Average positive volume was only found to increase 8.5% and average negative volume was found to decrease by 10.6% with the addition of parallel magnetic fields.

8. When using a 0.7T surface field strength permanent magnet as the source of the magnetic field, trials have shown that for the Lorentz forces pointing into the workpiece surface, positive (crater) volume increased by 30.5%, while negative (rim) volume increased by only 11% over a normal  $\mu$ -EDM discharge crater without any applied magnetic fields, leading to an increase in average erosion efficiency of 25%. The increase in erosion efficiency was tested for significance and mild evidence was found to suggest that erosion efficiency increases with the addition of the Lorentz force.
9. When using a 0.7T surface field strength permanent magnet as the source of the magnetic field, the Lorentz force pointing outward from the workpiece surface has been shown to decrease negative (rim) volume by 43% and decrease positive (crater) volume by 23% without affecting erosion efficiency. This suggests that this configuration of the Lorentz force process hinders melt pool material movement during a discharge but has no impact on overall process efficiency.
10. When using an electromagnet as the source of the magnetic field, the Lorentz force pointing into the workpiece has been shown to increase erosion efficiency by 54% between the 0.33T and 0.66T field strengths. In this case, positive (crater) volume is seen to increase by 28% while negative (rim) volume decreases by 50%, indicating that the increase in erosion efficiency is due to an increase in material removed from the melt pool as debris during a discharge.
11. When using an electromagnet as the source of the magnetic field and a field strength of 1T, the debris distance distribution shifts to values further from the discharge crater with the application of the Lorentz force pointing into the workpiece surface. This

suggests that the addition of the Lorentz force in this configuration causes an increase in the ejection force of debris from the melt pool.

12. When using an electromagnet as the source of the magnetic field, the Lorentz force pointing outward from the workpiece causes a decrease in both positive and negative discharge crater volumes, resulting in a decrease of 35% in erosion efficiency between the 0.33 and 1T field strengths. Lorentz forces pointing outward from the workpiece surface cause a decrease in melt pool material transport from the discharge crater center to the rim, reducing erosion efficiency of the process.
13. Taken together, the volume, erosion efficiency, plasma temperature, electron density, and debris field data strongly suggest that the Lorentz forces cause a mechanical effect in the melt pool to alter the material removal mechanism. With the Lorentz force pointing into the workpiece surface, the plasma pressure on the melt pool is increased by the addition of the Lorentz force, transporting more debris to the outer edge of the melt pool, where it was removed as additional debris upon plasma channel collapse. As a result, the Lorentz force pointing into the workpiece surface has been determined to be a viable method of enhancing MRR in the  $\mu$ -EDM process through the use of magnetic fields in the machining of non-magnetic workpiece materials.
14. For the Lorentz force pointing outward from the workpiece surface, the combined data strongly suggests that the added force counteracts the plasma pressure force, thus hindering material transport from the center of the discharge crater to the crater rim. Thus, the Lorentz force pointing outward from the workpiece surface has been determined to not be a viable method for enhancing MRR in the  $\mu$ -EDM process.

15. Equal trace amounts <1% of the electrode material were found in the parallel field melt pools and the parallel field with directional current melt pools, indicating that the additional Lorentz forces do not have a negative impact on electrode wear.

## 5.3 Recommendations for Future Work

1. Additional workpiece and electrode materials need to be tested to determine the effectiveness of the Lorentz force technique with other non-magnetic materials commonly used in  $\mu$ -EDM such as tungsten carbide, magnesium, and molybdenum as well as magnetic workpiece materials such as tool steels to ensure the process can be extended to all  $\mu$ -EDM applications.
2. Only a narrow range of discharge process parameters were tested in this study. A parametric study on the effect of discharge process parameters on the Lorentz force technique would be beneficial for optimizing the process to maximize the increases in erosion efficiency observed in this thesis.
3. The flow characteristics of the molten pool have been shown to be affected by the addition of the Lorentz force. The development of a model to simulate these flow characteristics would be extremely beneficial for further research into magnetic field-assisted  $\mu$ -EDM techniques. Modeling the flow characteristics would provide information on the forces present in the melt pool that may help identify methods of magnetic field application to further increase the removal of material from the melt pool.
4. The extension of the Lorentz force-assisted  $\mu$ -EDM technique to full-scale machining operations is required to determine industrial viability and measure MRR and TWR at

this level for comparison to other productivity improvement techniques implemented in full-scale  $\mu$ -EDM operations. In order to complete this task, several new components need to be added to the testbed. A spark discharge circuit capable of continuous discharge pulse trains is required. A discharge gap monitoring and control technique needs to be implemented in order to produce stable cutting conditions during a machining operation. Finally, a dielectric flushing technique needs to be implemented in order to determine if the Lorentz force technique provides sufficient debris removal or if a secondary debris removal technique needs to be employed to keep the discharge gap clear of debris.

# Bibliography

- [1] Uruarte, L., Herrero, A., Ivanov, A., Oosterling, H., Staemmler, L., Tang, P.T., and Allen, D., 2006, "Comparison between micro fabrication technologies for metal tooling," Special Issue paper, Proc. IMechE 220, pp. 1665-1676.
- [2] Schumacher, B.M., 2004, "After 60 years of EDM the discharge process remains still disputed," J. Matl. Proc. Tech., 149, pp. 376-381.
- [3] Allen, P., Chen, X., Kim, D., 2005, "Numerical and Experimental Study on Micro-Electrical Discharge Micromachining Characteristics on Molybdenum," Proceedings of IMECE2005, pp. 1131-1137.
- [4] Allen, P., Chen, X., 2007, "Process simulation of micro electro-discharge machining on molybdenum," J. Matl. Proc. Tech., 186, pp. 346-355.
- [5] Liu, H.S., Yan, B.H., Huang, F.Y., Qiu, K.H., 2005, "A study on the characterization of high nickel alloy micro-holes using micro-EDM and their applications," J. Matl. Proc. Tech., 169, pp. 418-426.
- [6] Ponappa, K., Aravindan, S., Rao, P.V., Ramkumar, J., Gupta, M., 2010, "The effect of process parameters on machining of magnesium nano alumina composites through EDM," Int. J. Adv. Manuf. Technol., 46, pp. 1035-1042.
- [7] Pradhan, B.B., Masanta, M., Sarkar, B.R., Bhattacharyya, B., 2009, "Investigation of electro-discharge micro-machining of titanium super alloy," Int. J. Adv. Manuf. Technol., 41, pp. 1094-1106.

- [8] Somashekhar, K.P., Ramachandran, N., Mathew, J., 2009, "Modeling and optimization of process parameters in micro Wire EDM by Genetic Algorithm," *Adv. Matl. Research*, 76-78, pp. 566-570.
- [9] Son, S., Lim, H., Kumar, A.S., Rahman, M., 2007, "Influences of pulsed power condition on the machining properties in micro EDM," *J. Matl. Proc. Tech.*, 190, pp. 73-76.
- [10] Sundaram, M.M., Pavalarajan, G.B., Rajurkar, K.P., 2008, "A Study on Process Parameters of Ultrasonic Assisted Micro EDM Based on Taguchi Method," *J. Matl. Eng. and Perf.*, 17(2), pp. 210-215.
- [11] Wang, A.C., Yan, B.H., Tang, Y.X., Huang, F.Y., 2005, "The feasibility study on a fabricated micro slit die using micro EDM," *Int. J. Adv. Manuf. Technol.*, 25, pp. 10-16.
- [12] Lin, C.T., Chow, H.M., Yang, L.D., Chen, Y.F., 2007, "Feasibility study of micro-slit EDM machining using pure water," *Int. J. Adv. Manuf. Technol.*, 34, pp. 104-110.
- [13] Chung, D.K., Shin, H.S., Kim, B.H., Park, M.S., Chu, C.N., 2009, "Surface finishing of micro-EDM holes using deionized water," *J. Micromech. Microeng.*, 19, pp. 1-7.
- [14] Chow, H.M., Yan, B.H., Huang, F.Y., Hung, J.C., 2000, "Study of added powder in kerosene for the micro-slit machining of titanium alloy using electro-discharge machining," *J. Matl. Proc. Tech.*, 101, pp. 95-103.
- [15] Klocke, F., Lung, D., Antonoglou, G., Thomaidis, D., 2004, "The effects of powder suspended dielectrics on the thermal influenced zone by electrodischarge machining with small discharge energies," *J. Matl. Proc. Tech.*, 149, pp. 191-197.

- [16] Yeo, S.H., Tan, P.C., Kurnia, W., 2007, "Effects of powder additives suspended in dielectric on crater characteristics for micro electrical discharge machining," *J. Micromech. Microeng.*, 17, pp. 91-98.
- [17] Chow, H.M., Yang, L.D., Lin, C.T., Chen, Y.F., 2008, "The use of SiC powder in water as dielectric for micro-slit EDM machining," *J. Matl. Proc. Tech.*, 195, pp. 160-170.
- [18] Prihandana, G.S., Mahardika, M., Hamdi, M., Wong, Y.S., Mitsui, K., 2009, "Effect of micro-powder suspension and ultrasonic vibration of dielectric fluid in micro-EDM processes—Taguchi approach," *Int. J. Mach. Tools & Manuf.*, 49, pp. 1035-1041.
- [19] Wang, J., Wang, Y.G., Zhao, F.L., 2009, "Simulation of Debris Movement in Micro Electrical Discharge Machining of Deep Holes," *Matl. Sci. Forum*, 626-627, pp. 267-272.
- [20] Kiran, M.P.S.K., Joshi, S.S., 2007, "Modeling of Surface Roughness and the Role of Debris in Micro-EDM," *J. Manuf. Sci. Eng.*, 129, pp. 265-273.
- [21] Richardson, M.T., Gianchandani, Y.B., 2010, "Wireless Monitoring of Workpiece Material Transitions and Debris Accumulation in Micro-Electro-Discharge Machining," *J. Microelectromechanical Systems*, 19(1), pp. 48-54.
- [22] Bamberg, E., Heamawatanachai, S., 2009, "Orbital electrode actuation to improve efficiency of drilling micro-holes by micro-EDM," *J. Matl. Proc. Tech.*, 209, pp. 1826-1834.
- [23] Cao, M., Yang, S., Li, W., Yang, S., 2010, "Chip-Ejection Mechanism and Experimental Study of Water Dispersant Dielectric Fluid on Small-Hole EDM," *Adv. Matl. Res.*, 97-101, pp. 4111-4115.

- [24] Wansheng, Z., Zhenlong, W., Shichun, D., Guanxin, C., Hongyu, W., 2002, "Ultrasonic and electric discharge machining to deep and small hole on titanium alloy," *J. Matl. Proc. Tech.*, 120, pp. 101-106.
- [25] Gao, C., Liu, Z., 2003, "A study of ultrasonically aided micro-electrical-discharge machining by the application of workpiece vibration," *J. Matl. Proc. Tech.*, 139, pp. 226-228.
- [26] Huang, H., Zhang, H., Zhou, L., Zheng, H.Y., 2003, "Ultrasonic vibration assisted electro-discharge machining of microholes in Nitinol," *J. Micromech. Microeng.*, 13, pp. 693-700.
- [27] Chern, G.L., Chuang, Y., 2006, "Study on vibration-EDM and mass punching of micro-holes," *J. Matl. Proc. Tech.*, 180, pp. 151-160.
- [28] Hung, J.C., Lin, J.K., Yan, B.H., Liu, H.S., Ho, P.H., 2006, "Using a helical micro-tool in micro-EDM combined with ultrasonic vibration for micro-hole machining," *J. Micromech. Microeng.*, 16, pp. 2705-2713.
- [29] Kim, D.J., Yi, S.M., Lee, Y.S., Chu, C.N., 2006, "Straight hole micro EDM with a cylindrical tool using a variable capacitance method accompanied by ultrasonic vibration," *J. Micromech. Microeng.*, 16, pp. 1092-1097.
- [30] Endo, T., Tsujimoto, T., Mitsui, K., 2008, "Study of vibration-assisted micro-EDM—The effect of vibration on machining time and stability of discharge," *Precision Eng.*, 32, pp. 269-277.
- [31] Sundaram, M.M., Pavalarajan, G.B., Rajurkar, K.P., 2008, "A Study on Process Parameters of Ultrasonic Assisted Micro EDM Based on Taguchi Method," *J. Matl. Eng. and Perf.*, 17(2), pp. 210-215.

- [32] Tong, H., Li, Y., Wang, Y., 2008, "Experimental research on vibration assisted EDM of micro-structures with non-circular cross-section," *J. Matl. Proc. Tech.*, 208, pp. 289-298.
- [33] Jia, B.X., Wang, D.S., Guo, J.Z., 2009, "Machining Deep Micro Holes by EDM with USM in Inversion Installing," *Matl. Sci. Forum.*, 626-627, pp. 321-326.
- [34] Yu, Z.Y., Zhang, Y., Li, J., Luan, J., Zhao, F., Guo, D., 2009, "High aspect ratio micro-hole drilling aided with ultrasonic vibration and planetary movement of electrode by micro-EDM," *CIRP Annals*, 58, pp. 213-216.
- [35] Yeo, S. H., Murali, M., Cheah, H.T., 2004, "Magnetic field assisted micro electro-discharge machining," *Journal of Micromechanics and Microengineering*, 14, pp. 1526-1529.
- [36] Tayler, R.J., 1957, "The Influence of an Axial Magnetic Field on the Stability of a Constricted Gas Discharge," *Proceedings of the Physical Society*, 70(11), pp. 1049-1063.
- [37] Keidar, M., Beilis, I., Boxman, R.L., Goldsmith, S., 1996, "2D expansion of the low-density interelectrode vacuum arc plasma jet in an axial magnetic field," *J. Phys. D: Appl. Phys.*, 29, pp. 1973-1983.
- [38] Beilis, I.I., Keidar, M., Boxman, R.L., Goldsmith, S., 1998, "Theoretical study of plasma expansion in a magnetic field in a disk anode vacuum arc," *J. Appl. Phys.*, 83(2), pp. 709-717.
- [39] Rondanini, M., Cavallotti, C., Ricci, D., Chrastina, D., Isella, G., Moiseev, T., von Kanel, H., 2008, "An experimental and theoretical investigation of a magnetically confined dc plasma discharge," *J. Appl. Phys.*, 104, pp. 1-13.
- [40] Hagelaar, G.J.M., 2007, "Modelling electron transport in magnetized low-temperature discharge plasmas," *Plasma Sources Sci. Technol.*, 16, pp. 57-66.

- [41] Masuzawa, T., 2000, "State of the Art of Micromachining," *Annals of CIRP*, 49(2), pp. 473-488.
- [42] Lazarenko, B.R., Lazarenko, N., 1943, "About the inversion of metal erosion and methods to fight ravage of electric contacts," WEI-Institute, Moscow (in Russian).
- [43] Jameson, E. C., 2001, *Electrical Discharge Machining*, Society of Manufacturing Engineers, Michigan, pp. 1-21, Ch. 1.
- [44] Ho, K.H., Newman, S.T., 2003, "State of the art electrical discharge machining (EDM)," *Int. J. of Mach. Tools & Manuf.*, 43, pp. 1287-1300.
- [45] Masuzawa, T., Sata, T., Kinoshita, N., 1972, "The Role of the Chips in Micro-EDM," *Bull. Japan Soc. of Prec. Eng.*, 6(1), pp 8-14.
- [46] Ehrfeld, W., Lehr, H., Michel, F., Wolf, A., 1996, "Micro Electro Discharge Machining as a Technology in Micromachining," *Proc. SPIE*, 2879, pp. 332-337.
- [47] Beltrami, I., Joseph, C., Clavel, R., Bacher, J.P., Bottinelli, S., 2004, "Micro- and nanoelectric-discharge machining," *J. Matl. Proc. Tech.*, 149, pp. 263-265.
- [48] Liao, Y.S., Chen, S.T., Lin, C.S., Chuang, T.J., 2005, "Fabrication of high aspect ratio microstructure arrays by micro reverse wire-EDM," *J. Micromech. Microeng.*, 15, pp. 1547-1555.
- [49] Guber, A.E., Giordano, N., Loser, M., Wieneke, P., 1997, "Mikroinstrumente aus Nickel-Titan," *F & M*, 105(4), pp. 247-251.
- [50] Crowe, R. W., 1956, "Formative Time Lags in the Electric Breakdown of Liquid Hydrocarbons," *J. Appl. Phys.*, 27(2), pp. 156-160.
- [51] Greene, J.E., Guerrero-Alvarez, J.L., 1974, "Electro-Erosion of Metal Suraces," *Metallurgical Transactions*, 5, pp. 695-706.

- [52] Gray, E.W., Pharney, J.R., 1974, "Electrode erosion by particle ejection in low-current arcs," *J. Appl. Phys.*, 45(2), pp. 667-671.
- [53] Erden, A., Kaftanoglu, B., 1981, "Thermo-Mathematical Modelling and Optimization of Energy Pulse Forms in Electric Discharge Machining (EDM)," *Int. J. Mach. Tool Des. Res.*, 21(1), pp. 11-22.
- [54] McGeough, J.A., Rasmussen, H., 1982, "A macroscopic model of electro-discharge machining," *Int. J. Mach. Tool Design and Res.*, 22(4), pp. 333-339.
- [55] DiBitonto, D.D., Eubank, P.T., Patel, M.R., Barrufet, M.A., 1989, "Theoretical models of the electrical discharge machining process. I. A simple cathode erosion model," *J. Appl. Phys.*, 66(9), pp. 4095-4103.
- [56] Patel, M.R., Barrufet, M.A., Eubank, P.T., DiBitonto, D.D., 1989, "Theoretical models of the electrical discharge machining process. II. The anode erosion model," *J. Appl. Phys.*, 66(9), pp. 4104-4111.
- [57] Wang, B.J., Saka, N., Rabinowicz, E., 1992, "Static-gap, single-spark erosion of Ag-CdO and pure metal electrodes," *Wear*, 157, pp.31-49.
- [58] Eubank, P.T., Patel, M.R., Barrufet, M.A., Bozkurt, B., 1993, "Theoretical models of the electrical discharge machining process. III. The variable mass, cylindrical plasma model," *J. Appl. Phys.*, 73(11), pp. 7900-7909.
- [59] Witz, G., Revaz, B., Flukiger, R., 2005, "Heat transfer and Marangoni effect in the electron discharge machining (EDM) process," *Proceedings of the COMSOL Multiphysics User's conference*, Paris.
- [60] Yeo, S.H., Kurnia, W., Tan, P.C., 2008, "Critical assessment and numerical comparison of electro-thermal models in EDM," *J. Matl. Proc. Tech.*, 203, pp. 241-251.

- [61] Wong, Y.S., Rahman, M., Lim, H.S., Han, H., Ravi, N., 2003, "Investigation of micro-EDM material removal characteristics using single *RC*-pulse discharges," *J. of Matl. Proc. Tech.*, 140, pp. 303-307.
- [62] Dhanik, S., Joshi, S.S., 2005, "Modeling of a Single Resistance Capacitance Pulse Discharge in Micro-Electro Discharge Machining," *J. Manuf. Sci. Eng.*, 127(4), pp. 759-767.
- [63] Katz, Z., Tibbles, C.J., 2005, "Analysis of micro-scale EDM process," *Int. J. Adv. Manuf. Technol.*, 25, pp. 923-928.
- [64] Soldera, F.A., Mucklich, F., 2005, "On the Erosion of Material Surfaces caused by Electrical Plasma Discharging," *Mater. Res. Soc. Symp. Proc.*, 843, pp. T5.4.1-T5.4.6.
- [65] Yeo, S.H., Kurnia, W., Tan, P.C., 2007, "Electro-thermal modelling of anode and cathode in micro-EDM," *J. Phys. D: Appl. Phys.*, 40, pp. 2513-2521.
- [66] Descoedres, A., 2006, "Characterization of EDM Plasmas," Ph. D. Thesis, Ecole Polytechnique Federale De Lausanne.
- [67] Raizer, Y.P., 1991, *Gas Discharge Physics*, Springer-Verlag, Berlin.
- [68] Tsai, Y.Y., Masuzawa, T., 2004, "An index to evaluate the wear resistance of the electrode in micro-EDM," *J. Matl. Proc. Tech.*, 149, pp. 304-309.
- [69] Boothroyd, G.G., 2006, *Fundamentals of Machining and Machine Tools*, CRC/Taylor and Francis, Boca Raton.
- [70] Kao, C.C., Shih, A.J., 2006, "Sub-nanosecond monitoring of micro-hole electrical discharge machining pulses and modeling of discharge ringing," *Int. J. Mach. Tools & Manuf.*, 46, pp. 1996-2008.

- [71] Mahendran, S., Devarajan, R., Nagarajan, T., Majdi, A., 2010, "A Review of Micro-EDM," Proc. Of IMECS, 2, pp. 1-6.
- [72] Jahan, M.P., Wong, Y.S., Rahman, M., 2008, "A Comparative Study of Transistor and RC Pulse Generators for Micro-EDM of Tungsten Carbide," Int. J. Precision Eng. and Manuf., 9(4), pp. 3-10.
- [73] Yu, Z.Y., Rajurkar, K.P., Shen, H., 2002, "High Aspect Ratio and Complex Shaped Blind Micro Holes by Micro EDM," CIRP Annals, 51(1), pp. 359-362.
- [74] Tong, H., Li, Y., Wang, Y., Yu, D., 2008, "Servo scanning 3D micro-EDM based on macro/micro-dual-feed spindle," Int. J. Mach. Tools & Manuf., 48, pp. 858-869.
- [75] Kunieda, M., Lauwers, B., Rajurkar, K.P., Schumacher, B.M., 2005, "Advancing EDM through Fundamental Insight into the Process," CIRP Annals, 54(2), pp. 64-87.
- [76] Lin, Y.C., Yan, B.H., Chang, Y.S., 2000, "Machining characteristics of titanium alloy (Ti-6Al-4V) using a combination process of EDM with USM," J. of Matl. Proc. Tech., 104, pp. 171-177.
- [77] Chen, S.T., Yang, H.Y., Du, C.W., 2009, "Study of an ultrafine w-EDM technique," J. Micromech. Microeng., 19, pp. 1-8.
- [78] Lim, H.S., Wong, Y.S., Rahman, M., Lee, M.K.E., 2003, "A study on the machining of high-aspect ratio micro-structures using micro-EDM," J. Matl. Proc. Tech., 140, pp. 318-325.
- [79] Zhao, W., Yang, Y., Wang, Z., Zhang, Y., 2004, "A CAD/CAM system for micro-ED-milling of small 3D freeform cavity," J. Matl. Proc. Tech., 149(1-3), pp. 573-578.

- [80] Masuzawa, T., Fujino, M., Kobayashi, K., Suzuki, T., Kinoshita, N., 1985, "Wire Electro-Discharge Grinding for Micro-Machining," *Annals of CIRP*, 34(1), pp. 431-434.
- [81] Diver, C., Atkinson, J., Helml, H.J., Li, L., 2004, "Micro-EDM drilling of tapered holes for industrial applications," *J. Matl. Proc. Tech.*, 149, pp. 296-303.
- [82] Yamazaki, M., Suzuki, T., Mori, N., Kunieda, M., 2004, "EDM of micro-rods by self-drilled holes," *J. Matl. Proc. Tech.*, 149, pp. 134-138.
- [83] Jahan, M.P., Wong, Y.S., Rahman, M., 2009, "A study on the fine-finish die-sinking micro-EDM of tungsten carbide using different electrode materials," *J. Matl. Proc. Tech.*, 209, pp. 3956-3967.
- [84] Yan, B.H., Wang, A.C., Huang, C.Y., Huang, F.Y., 2002, "Study of precision micro-holes in borosilicate glass using micro EDM combined with micro ultrasonic vibration machining," *Int. J. Mach. Tools & Manuf.*, 42, pp. 1105-1112.
- [85] Weng, F.T., Her, M.G., 2002, "Study of the Batch Production of Micro Parts Using the EDM Process," *Int. J. Adv. Manuf. Tech.*, 19(4), pp. 266-270.
- [86] Her, M.G., Weng, F.T., 2001, "Micro-hole Machining of Copper Using the Electro-discharge Machining Process with a Tungsten Carbide Electrode Compared with a Copper Electrode," *Int. J. Adv. Manuf. Tech.*, 17(10), pp. 715-719.
- [87] Ekmekci, B., Sayar, A., Opoz, T.T., Erden, A., 2010, "Characteristics of Surface Damage in Micro Electric Discharge Machining of Micro Holes," *Adv. Matl. Res.*, 83-86, pp. 688-695.
- [88] Ekmekci, B., Sayar, A., Opoz, T.T., Erden, A., 2009, "Geometry and surface damage in micro electrical discharge machining of micro-holes," *J. Micromech. Microeng.*, 19, pp. 1-16.

- [89] Kibria, G., Sarkar, B. R., Pradhan, B. B., Bhattacharyya, B., 2009, "Comparative study of different dielectrics for micro-EDM performance during microhole machining of Ti-6AL-4V alloy," *Int. J. Adv. Manuf. Technol.*
- [90] Jahan, M.P., Anwar, M.M., Wong, Y.S., Rahman, M., 2009, "Nanofinishing of hard materials using micro-electrodischarge machining," *Proc. IMechE Part B: Eng. Manuf.*, 223, pp. 1127-1142.
- [91] Pham, D.T., Dimov, S.S., Bigot, S., Ivanov, A., Popov, K., 2004, "Micro-EDM—recent developments and research issues," *J. Matl. Proc. Tech.*, 149, pp. 50-57.
- [92] Jahan, M.P., Wong, Y.S., Rahman, M., 2010, "A comparative experimental investigation of deep-hole micro-EDM drilling capability for cemented carbide (WC-Co) against austenitic stainless steel (SUS 304)," *Int. J. Adv. Manuf. Technol.*, 46(9-12), pp. 1145-1160.
- [93] Somashekhar, K.P., Ramachandran, N., Mathew, J., 2010, "Material removal characteristics of microslot (kerf) geometry in  $\mu$ -WEDM on aluminum," *Int. J. Adv. Manuf. Technol.*, online, pp. 1-16.
- [94] Yeo, S.H., Tan, L.K., 1999, "Effects of ultrasonic vibrations in micro electro-discharge machining of microholes," *J. Micromech. Microeng.*, 9, pp. 345-352.
- [95] Yeo, S.H., Goh, K.M., 2001, "The effect of ultrasound in micro electro discharge machining on surface roughness," *Proc. Instn. Mech. Engrs.*, 215(B), pp. 271-276.
- [96] Murali, M., Yeo, S.H., 2004, "Rapid Biocompatible Micro Device Fabrication by Micro Electro-Discharge Machining," *Biomedical Microdevices*, 6(1), pp. 41-45.
- [97] Egashira, K., Matsugasako, A., Tsuchiya, H., Miyazaki, M., 2006, "Electrical discharge machining with ultralow discharge energy," *Precision Engineering*, 30, pp. 414-420.

- [98] Hao, T., Yang, W., Yong, L., 2008, "Vibration-assisted servo scanning 3D micro EDM," *J. Micromech. Microeng.*, 18, pp. 1-8.
- [99] Yan, B.H., Wang, A.C., Huang, C.Y., Huang, F.Y., 2002, "Study of precision micro-holes in borosilicate glass using micro EDM combined with micro ultrasonic vibration machining," *Int. J. Mach. Tools & Manuf.*, 42, pp. 1105-1112.
- [100] Endo, T., Tsujimoto, T., Mitsui, K., 2006, "Fabrication of Micro-Components Using Vibration-Assisted Micro-EDM," *Proc. American Society for Precision Eng.*, 2006 Annual Meeting, pp. 515-518.
- [101] Sternberg, N., Godyak, V., Hoffman, D., 2006, "Magnetic field effects on gas discharge plasmas," *Physics of Plasmas*, 13, pp. 1-14.
- [102] Keidar, M., Beilis, I., Boxman, R.L., Goldsmith, S., 1996, "2D expansion of the low-density interelectrode vacuum arc plasma jet in an axial magnetic field," *J. Phys. D: Appl. Phys.*, 29, pp. 1973-1983.
- [103] Beilis, I.I., Keidar, M., Boxman, R.L., Goldsmith, S., 1998, "Theoretical study of plasma expansion in a magnetic field in a disk anode vacuum arc," *J. Appl. Phys.*, 83(2), pp. 709-717.
- [104] Rondanini, M., Cavallotti, C., Ricci, D., Chrastina, D., Isella, G., Moiseev, T., von Kanel, H., 2008, "An experimental and theoretical investigation of a magnetically confined dc plasma discharge," *J. Appl. Phys.*, 104, pp. 1-13.
- [105] Wilson, C.G., Gianchandani, Y.B., 2004, "Miniaturized Magnetic Nitrogen DC Microplasmas," *IEEE Trans. On Plasma Sci.*, 32(1), pp. 282-287.
- [106] Hassouba, M.A., 2001, "Effect of the magnetic field on the plasma parameters in the cathode fall region of the DC-glow discharge," *Eur. Phys. J. AP*, 14, pp. 131-135.

- [107] Tayler, R.J., 1957, "The Influence of an Axial Magnetic Field on the Stability of a Constricted Gas Discharge," *Proceedings of the Physical Society*, 70(11), pp. 1049-1063.
- [108] Kotalik, P., Nishiyama, H., 2002, "An Effect of Magnetic Field on Arc Plasma Flow," *IEEE Trans. On Plasma Sci.*, 30(1), pp. 160-161.
- [109] Kim, K.S., 2009, "Influence of a transverse magnetic field on arc root movements in a dc plasma torch: Diamagnetic effect of arc column," *Appl. Phys. Letters*, 94, pp. 1-3.
- [110] Rehbein, W., Schulze, H.P., Mecke, K., Wollenberg, G., Storr, M., 2004, "Influence of selected groups of additives on breakdown in EDM sinking," 149, pp. 58-64.
- [111] Amson, J.C., 1965, "Lorentz force in the molten tip of an arc electrode," *Brit. J. Appl. Phys.*, 16, pp. 1169-1179.
- [112] Gallet, B., Berhanu, M., Mordant, N., 2009, "Influence of an external magnetic field on forced turbulence in a swirling flow of liquid metal," *Physics of Fluids*, 21, online, pp. 1-13.
- [113] Jahan, M.P., Wong, Y.S., Rahman, M., 2009, "A study on the quality micro-hole machining of tungsten carbide by micro-EDM process using transistor and RC-type pulse generator," *J. Matl. Proc. Tech.*, 209, pp. 1706-1716.
- [114] Han, F., Chen, L., Yu, D., Zhou, X., 2007, "Basic study on pulse generator for micro-EDM," *Int. J. Adv. Manuf. Technology*, 33, pp. 474-479.
- [115] Liu, K., Lauwers, B., Reynaerts, D., 2010, "Process capabilities of Micro-EDM and its applications," *Int. J. Adv. Manuf. Technol.*, 47, pp. 11-19.
- [116] Bose, Bimal K., 1992, "Evaluation of Modern Power Semiconductor Devices and Future Trends of Converters," *IEEE Transactions on Industry Applications*, 28(2), pp. 403-413.

- [117] Jeswani, M.L., 1981, "Electrical Discharge Machining in Distilled Water," *Wear*, 72, pp. 81-88.
- [118] Soni, J.S., Chakraverti, G., 1996, "Experimental Investigation on Migration of Material During EDM of Die Steel (T215 Cr12)," *J. Matl. Proc. Tech.*, 56, pp. 439-451.
- [119] Lee, J.W., 2003, "Microstructural evaluation and phase transformation of recast layers in electrical discharge machined dual phase Fe-Mn-Al alloy," *J. Matl. Sci.*, 38, pp. 1679-1687.
- [120] Guu, Y.H., Hou, M.T.K., 2007, "Effect of machining parameters on surface textures in EDM of Fe-Mn-Al alloy," *Matl. Sci. and Eng. A*, 466, pp. 61-67.
- [121] Albinski, K., Musiol, K., Miernikiewicz, A., Labuz, S., Malota, M., 1996, "The temperature of a plasma used in electrical discharge machining," *Plasma Sources Sci. Technol.*, 5, pp. 736-742.
- [122] NIST atomic spectra database, Version 3,  
(URL:<http://physics.nist.gov/PhysRefData/ASD/index.html>).
- [123] Gigosos, M.A., Cardenoso, V., 1996, "New plasma diagnosis tables of hydrogen Stark broadening including ion dynamics," *J. Phys. B: At. Mol. Opt. Phys.*, 29(20), pp. 4795-4838.
- [124] Peakfit Software, (URL: <http://www.sigmaplot.com>).
- [125] Noguchi, Y., Matsuoka, A., Uchino, K., Muraoka, K., 2002, "Direct measurement of electron density and temperature distributions in micro-discharge plasma for a plasma display panel," *J. of Applied Physics*, 91(2), pp. 613-616.
- [126] Ito, T., Izaki, T., Terashima, K., 2000, "Development of plasma chip," *Surface and Coatings Technology*, 133, pp. 497-500.

- [127] Chen, F.F., 1984, *Introduction to Plasma Physics and Controlled Fusion, Vol. 1: Plasma Physics, 2<sup>nd</sup> ed.*, Plenum Press, New York, pp. 19-21, Chap. 2.
- [128] von Allmen, M., Blatter, A., 1995, *Laser-Beam Interactions with Materials*, Springer, New York, pp. 131-133, Chap. 5.
- [129] Kao, C.C., Shih, A.J., 2008, "Fuzzy Logic Control of Microhole Electrical Discharge Machining," *J. Manuf. Sci. and Eng.*, 130, pp. 1-6.
- [130] De Bruijn, H. E., Delft, TH, Pekelharing, A.J., 1978, "Effect of a Magnetic Field on the Gap Cleaning in EDM," *Annals of CIRP*, 27, pp. 93-95.
- [131] Lin, Y. C., Lee, H. S., 2008, "Machining characteristics of magnetic force-assisted EDM," *Int. J. of Machine Tools & Manuf.*, 48, pp. 1179-1186.
- [132] Lin, Y. C., Lee, H. S., 2009, "Optimization of machining parameters using magnetic-force-assisted EDM based on gray relational analysis," *Int. J. Adv. Manuf. Technol.*, 42, pp. 1052-1064.
- [133] Haines, M.G., Lebedev, S.V., Chittenden, J.P., Beg, F.N., Bland, S.N., Dangor, A.E., 2000, "The past, present, and future of Z pinches," *Physics of Plasmas*, 7(5), pp. 1672-1680.